Study on multi-timescale characteristics of ionospheric trough in subauroral/auroral region

Tetsuro Ishida

Department of Polar Science,
School of Multidisciplinary Sciences,
The Graduate University for Advanced Studies

March 2015

Contents

Abstract

The F-region ionospheric trough is a band of depleted electron density that extends longitudinally around the nightside subauroral/auroral region of Earth. The averaged electron density structure of the trough is well known, but the physical and/or chemical processes associated with its structural variation are still unclear. Hence, a detailed and unified investigation within the trough region is highly desirable. To understand the fundamental characteristics of the trough region, we conducted a multi-part investigation that consisted of the following two steps.

For the first step, we investigated seasonal variation and solar activity dependence of the quiet-time ionospheric trough using plasma parameter data obtained via Common Program 3 (CP-3) observations performed by the European Incoherent Scatter (EISCAT) radar between 1982 and 2011. These statistical studies are based upon geomagnetically quiet to moderate conditions because we needed to understand the pure response of seasonal variation and solar activity dependence as the first step. The statistical results indicated that strong plasma flow plays an important role in the trough formation especially in the sunlit regions. Since frictional heating accompanied by strong plasma flow decreases electron density through dissociative recombination process, the trough can be preserved even during summer which has a relatively higher ionization rate than in the other seasons. We also found that such frictional heating becomes more intense under high solar activity, and thus the troughs with frictional heating tend to be deeper. Additionally, we propose the possibility that the occurrence rate of the trough was influenced by field-aligned currents (FACs). Some of the case studies previously reported that the downward FACs could produce the trough structure, but its statistical characteristic is still unclear. Thus, this is the first statistical study which mentioned the relationship between the trough and FACs. Especially during

equinox, the occurrence rate of the trough increased/decreased in the downward/upward current region with solar activity, which was possibly caused by solar activity dependence of the FACs intensity.

The statistical studies above were based upon geomagnetically quiet to moderate conditions, and thus, for the second step, analyses under geomagnetically active conditions were performed to further understand the basic characteristics of the trough. Specifically, we focused on the trough region during a substorm event and investigated the small-structure called an ionospheric blob (a few hundreds of kilometers in scale), which is considered to be the main source of the irregularities. As such small-scale structures vary over relatively short-term durations, and we conducted new EISCAT radar observations with high-speed meridional scans (60–80 s) during October and December 2013. The temporal evolution of a blob was observed during a substorm event on December 4, 2013. This is the first report regarding direct observations of blob deformation in the trough region during a substorm. The observational results indicated that the enhanced plasma flow was associated with the deformation process of the blob within the trough region. We suggest that the blob deformation was caused by the following two-step process: the initial "seed" density structures are created by the Kelvin–Helmholtz instability and dissociative recombination, and then the smaller scale irregularities are secondarily created by the gradient-drift instability.

In summary, the obtained results indicated that enhancement of plasma flow plays an important role in trough structuring over both long-term and short-term durations. In regards to the long-term duration, enhancement of plasma flow forms the trough through dissociative recombination and preserves its structure from the effect of ionization. Such trough structuring is more intense under high solar activity. In regards to short-term periods, enhancement of plasma flow also contributes to trough structuring in the form of blob deformation through dissociative recombination and

some of the plasma instabilities. Besides, the results also indicated that the occurrence rate of the trough was influenced by the FACs. Especially during equinox, the occurrence rate of the trough varied with solar activity possibly under the influence of solar activity dependence of the FACs intensity.

Acknowledgements

The author first would like to thank Dr. Yasunobu Ogawa (chief supervisor) and Dr. Akira Kadokura (sub-supervisor). They sincerely supported the author's research activity and gave the author useful advice that helped him improve his research skills throughout the course of his Ph.D. work. Dr. Ogawa prepared the long-term EISCAT dataset necessary for the author's research activities and thesis work. The research introduced in Chapter 3 is based upon this EISCAT dataset. He also provided the author with opportunities to attend the EISCAT observation campaign and many international conferences. The observational data obtained during this EISCAT campaign were used for the research presented in Chapter 4, and the knowledge obtained from the conferences is reflected in many parts of this thesis. The author would like to emphasize here that this thesis work could not have been accomplished without his sincere supervising and generous support. Dr. Kadokura also provided useful and constructive advice throughout the author's Ph.D. activities. In particular, the discussion related to the magnetometer in Chapter 4 is based upon a series of discussions with him. Furthermore, he offered many helpful suggestions regarding the article from the perspective of magnetospheric physics.

The author also sincerely thanks Dr. Yasutaka Hiraki, Dr. Keisuke Hosokawa, and Dr. Yuichi Otsuka. Dr. Hiraki offered the author many helpful suggestions and much kind encouragement; discussions held with him are reflected in many parts of Chapter 3. Drs. Hosokawa and Otsuka also provided many helpful suggestions pertaining to the work presented in Chapter 4. The author also thanks Dr. Ryuho Kataoka for helpful suggestions regarding the research results. Additionally, the author wishes to express his heartfelt thanks to all staff members at the National Institute of Polar Research for their support and encouragement throughout his Ph.D. work.

This thesis research was supported financially by a Grant-in-Aid from the Japan Society for the Promotion of Science (JSPS) Fellows program. The author thanks Dr. Hiroshi Miyaoka for his employment as a research assistant. The author is indebted to the director and staff of EISCAT for providing the observational data. EISCAT is an international association supported by research organizations in China (CRIRP), France (CNRS, until the end of 2006), Finland (SA), Germany (DFG, until the end of 2011), Japan (NIPR and STEL), Norway (NFR), Sweden (VR), and the United Kingdom (NERC). In particular, Dr. Ingemar Häggström (EISCAT HQ) is also acknowledged for his helpful support in operating the EISCAT peer-reviewed program experiments and special experiments in Tromsø.

The author is thankful for the GPS-TEC data that were collected under the direction of A. J. Coster at the MIT Haystack Observatory. The TEC map was obtained from the GPS/TEC Plot routine on the Virginia Tech SuperDARN website (http://vt.superdarn.org/tiki-index.php?page=DaViT+TEC), which is supported by NSF award numbers AGS-0838219 and AGS-0946900. Additionally, the author thanks Dr. Takuya Tsugawa (NICT) and Dr. Michi Nishioka (NICT) for giving the author useful information about the TEC map.

The IMAGE magnetometer network is maintained by 10 institutes from Estonia, Finland, Germany, Norway, Poland, Russia, and Sweden. The author is grateful for their continuous effort in maintaining the instruments.

Finally, the author would like to express his sincere gratitude to the following advisory committee members for their constructive comments on this thesis: Dr. Yasunobu Ogawa, Dr. Akira Kadokura, Dr. Hisao Yamagishi, Dr. Keisuke Hosokawa, and Dr. Hitoshi Fujiwara.

1 Introduction

Here, we introduce the basic information necessary to understand this thesis. The basic physics of the upper atmosphere associated with this thesis is described in Sections 1.1–1.2. These sections are based upon Chapter 4 in *Brekke* [2013]. The basic information and some of the past publications of the ionospheric trough are introduced in Section 1.3. The plasma instabilities associated with the blob deformation (details are presented in Chapter 4) are explained in Section 1.4. Finally, we explain the objectives of this thesis in Section 1.5.

1.1 The upper atmosphere surrounding Earth

Earth's atmosphere below ~100 km is composed of ~78.1% molecular nitrogen (N_2), ~20.9% molecular oxygen (O_2), ~0.9% argon (Ar), and ~0.1% other gases. Molecules start to dissociate above ~100 km of altitude, and the scale height of each chemical species is determined approximately by the equilibrium between the gravitational force and diffusion processes that depend on each species' molecular mass. Hence, the constituents of the atmosphere vary with altitude. Figure 1.1 shows detailed altitudinal profiles of each species between 100 and 1000 km under solar minimum and maximum conditions [from *U.S. Standard Atmosphere*, 1976]. The dominant molecule/atom varies with altitude and solar activity. For example, atomic hydrogen dominates from 400–1000 km under solar minimum conditions (see Panel a), but atomic oxygen becomes dominant from 250–1000 km under solar maximum conditions (see Panel b). This occurs because the scale height of each species depends on atmospheric temperature, and thus, the scale height varies with solar activity. The neutral temperature varies with time of day, season, or solar activity, and the altitudinal profile of each species varies accordingly. In addition, it is known that atmospheric

composition has strong latitudinal dependence. Figure 1.2 shows the latitudinal dependence of molecular nitrogen (N_2), molecular oxygen (O_2), and helium (He) at 300 km under solstice and equinox conditions [from *Roble*, 1987]. In this figure, the important feature to note is that the O/N_2 ratio in the winter hemisphere is greater than that in the summer hemisphere. This latitudinal difference in atmospheric composition occurs because of the summer-to-winter neutral circulation, which is called the *seasonal anomaly*. The increased O and decreased N_2 densities in winter turn out to increase the O^+ density. However, as the atmospheric composition is also influenced by chemical and physical processes, the situation is actually more complicated than described above. Some of the neutral atomic and molecular species turn into ions and electrons via photoionization processes in response to the Sun's extreme ultra violet (EUV) radiation. The region where such ionization occurs is called the ionosphere (details below).

Beyond the limit of the ionosphere (~1000 km) is a region dominated by Earth's magnetic field, which is called the magnetosphere. The plasma in the magnetosphere consists mainly of electrons and protons, which originate from the solar wind (from outer) and the ionosphere (from inner). There are small fractions of He^+ and O^+ ions of ionospheric origin and some He^{++} ions originating from the solar wind. As the shape and boundary of the magnetosphere changes in response to the solar wind, its area cannot be delineated precisely. However, it has been confirmed from satellite observations that the sunward boundary of the magnetosphere is located ~10 Re from Earth (the distance between the dawn–dusk boundaries is ~15 Re) and its tail is elongated anti-sunward beyond ~150 Re (after *Pilipp and Morfill* [1987]; from *Kivelson and Russell* [1995]), as shown in Figure 1.3. Here, Re is the mean radius of the Earth ($= 6.37 \times 10^6$ m). It is known that Earth is protected against cosmic rays and energetic particles from the Sun by the magnetosphere. In addition, the magnetosphere influences

the ionosphere via field-aligned currents (FACs). The spatial distribution of the FACs was first revealed by *Iijima and Potemra* [1976] using statistical analyses of satellite data. Figure 1.4 shows that the spatial distribution of the FACs (from *Iijima and Potemra* [1976]) comprises two current systems: Region 1 (R1) current and Region 2 (R2) current. The R1 current is distributed at the auroral region and located above the latitude of the R2 current. The R1 current flows outward from the ionosphere in the dusk sector and into the ionosphere in the dawn sector. Conversely, the R2 current flows into the ionosphere in the dusk sector and outward from the ionosphere in the dawn sector. It is considered that the magnetosphere and ionosphere form some sort of closed circuit via the FACs called the ionospheric current closure. Figure 1.5 shows a schematic image of the three-dimensional current closure in the magnetosphere–ionosphere (M–I) coupling system [after *Hosokawa*, 2008]. As electrons and ions play a role as carriers of current, it can be considered that this current closure influences the electron-density structure of the ionosphere. However, the physical and/or chemical processes associated with the M–I coupling are not fully understood. As the ionosphere is connected with the magnetosphere via geomagnetic field lines, magnetospheric convection is also mapped to the ionosphere in the M–I coupling system. Figure 1.6 displays how ionospheric convection is driven by the magnetosphere [after *Hosokawa*, 2008]. When the southward interplanetary magnetic field (IMF), i.e., the Sun's magnetic field lines, contacts the terrestrial field lines at the dayside reconnection point (see D-Rx in Figure 1.6a), the IMF is reconnected with the terrestrial field lines and moves anti-sunward (see 1–6 in Figure 1.6b). Subsequently, the geomagnetic field lines become reconnected with each other at the nightside reconnection point (see N-Rx in Figure 1.6a) and move sunward via the outside trajectories (see 7–9 in Figure 1.6b). Hence, the signature of ionospheric convection is generally a two-cell pattern, as shown in Figure 1.6b. In the ionosphere, the

high-density plasma structures are convected from the dayside to the nightside, and their transport in the nightside region depends on the ionospheric convection pattern.

1.2 Ionosphere

The ionosphere is divided into three primary layers by altitude: the D-layer (70–100 km), E-layer (100–150 km), and F-layer (above ~150 km), although the F-layer is divided further into two distinct sublayers, the F1-layer (150–200 km) and F2-layer (above ~200 km), because of the strong EUV during daytime. The composition of the neutral atmosphere and EUV intensity vary with altitude, and thus, the predominant ion species and electron density also differ with altitude. Figure 1.7 shows the altitudinal profile of the most typical ion species together with the corresponding electron density profile [after *Richmond*, 1987; from *Brekke*, 2013]. This figure shows that the predominant ion species in the F region are O^+ ions followed by NO^+ ions and O_2^+ ions. The neutral density is ~$10^{15}/\mathrm{m}^3$ in the F region, while the electron density is at most $\sim 10^{12}/\mathrm{m}^3$, even in daytime under solar minimum conditions. Hence, the ionization rate in the F region is at most ~0.1%. In addition, the electron density varies with time, season, or solar activity because the EUV intensity depends on these factors. Figure 1.8 shows the variation of the electron density profile with time and solar activity [from *Richmond*, 1987]. The electron density profiles for solar minimum and maximum conditions are similar, but the peak altitude clearly increases from solar minimum to maximum conditions. As mentioned above, because scale height increases with increasing temperature, the peak altitude also shifts upwards under solar maximum conditions.

The ion (electron) density in the ionosphere is held in equilibrium between the production by solar radiation and particle precipitation and the losses incurred by

chemical and photochemical processes and transportation phenomena such as diffusion, neutral winds, and plasma transportation caused by the FACs. This relationship can be expressed by the following continuous equation:

$$\frac{\partial n_{\mathrm{i}}}{\partial t} = q_{\mathrm{i}} - l_{\mathrm{i}} - \nabla \cdot (\boldsymbol{v}_{\mathrm{i}} n_{\mathrm{i}}) \tag{1.1}$$

where n_{i} is the density of the ion species, q_{i} is the production, l_{i} is the loss by chemical and photochemical processes, and the last term is the divergence due to transportation phenomena through a volume of interest (the advection term).

First, we will explain the production term. The main causes of the production in the F region are solar radiation and particle precipitation from the magnetosphere. Among them, the production term caused by only solar radiation can be expressed with the following equation (e.g., see Chapter 4 in *Brekke* [2013] for the derivation of formula):

$$q = q_{\mathrm{m,0}} \exp\left(1 - x - \sec\chi \exp(-x)\right) \tag{1.2}$$

where $q_{\mathrm{m,0}}$ is the ion production rate at maximum for an overhead sun ($\chi = 0°$), χ is the solar zenith angle, and $x = \left(z - z_{m,0}\right)/H$ is the normalized height where $z_{\mathrm{m,0}}$ is the altitude of peak production and H the scale height. Figure 1.9 illustrates the ionization profiles for different zenith angles between 0° and 80° [after *Van Zandt and Knecht*, 1964; from *Brekke*, 2013]. It can be seen that the height of peak production increases with increases in the solar zenith angle. Furthermore, the peak altitude also becomes higher because of particle precipitation from the magnetosphere.

Next, we explain the loss term, which is most important regarding discussions of the ionospheric trough. As mentioned above, O^+ ions are the dominant ions in the

ionosphere. It is known that O^+ ions will combine with N_2 and O_2 molecules via the charge exchange reaction and produce NO^+ and O_2^+ ions with rate coefficients of k_1 and k_2, respectively:

$$\begin{aligned} O^+ + N_2 &\xrightarrow{k_1} NO^+ + N \\ O^+ + O_2 &\xrightarrow{k_2} O_2^+ + O \end{aligned} \tag{1.3}$$

The dissociative recombination occurs after the charge exchange reaction and as a result, the NO^+ and O_2^+ ions recombine with electrons as follows:

$$\begin{aligned} NO^+ + e &\xrightarrow{\alpha_1} N + O \\ O_2^+ + e &\xrightarrow{\alpha_2} O + O \end{aligned} \tag{1.4}$$

In a quasi-chemical photoequilibrium condition, the loss rate of electrons (dissociative reaction rate) is given by

$$\beta = \frac{k_1[N_2] + k_2[O_2]}{1 + \frac{k_1}{\alpha_1}\frac{[N_2]}{n_e} + \frac{k_2}{\alpha_2}\frac{[O_2]}{n_e}} \tag{1.5}$$

where $[N_2]$ and $[O_2]$ are the number density of N_2 and O_2, respectively. The values for k_1 and k_2 are on the order of $2 \times 10^{-18}\mathrm{m}^3\mathrm{s}$, while α_1 and α_2 are on the order of $10^{-13}\mathrm{m}^3\mathrm{s}$. Furthermore, $[N_2] < 10^{15}\mathrm{m}^{-3}$ and $[O_2] \approx 10^{14}\mathrm{m}^{-3}$ in the F-region altitude. Hence, $\alpha_1 \cdot n_e$ and $\alpha_2 \cdot n_e$ are respectively much larger than $k_1[N_1]$ and $k_2[O_2]$, and thus, Equation 1.5 can be simplified as follows:

$$\beta = k_1[\mathrm{N_2}] + k_2[\mathrm{O_2}] \tag{1.6}$$

The rate coefficients of dissociative recombination have been studied by many researchers [e.g., *McFarland et al.*, 1973; *Albritton et al.*, 1977]; hence, it is important to select appropriate coefficients for the targets. *St.-Maurice and Torr* [1978] parameterized the rate coefficient most suitable for the reaction of the high-latitude F region by using a bi-Maxwellian ion velocity distribution. Our research topic is the ionospheric trough in the high-latitude region, and therefore, we applied their rate coefficient for this study. The rate coefficients derived by *St.-Maurice and Torr* [1978] are expressed as follows:

$$\begin{aligned} k_1 &= 1.533 \times 10^{-12} - 5.92 \times 10^{-13}\left(\frac{T_{\mathrm{eff}}}{300}\right) \\ &+8.60 \times 10^{-14}\left(\frac{T_{\mathrm{eff}}}{300}\right) \quad 300 \le T_{\mathrm{eff}} \le 1700°K \end{aligned} \tag{1.7}$$

$$\begin{aligned} k_1 &= 2.73 \times 10^{-12} - 1.155 \times 10^{-12}\left(\frac{T_{\mathrm{eff}}}{300}\right) \\ &+1.483 \times 10^{-13}\left(\frac{T_{\mathrm{eff}}}{300}\right)^2 \quad 1700 < T_{\mathrm{eff}} < 6000°K \end{aligned} \tag{1.8}$$

$$\begin{aligned} k_2 &= 2.82 \times 10^{-11} - 7.74 \times 10^{-12}\left(\frac{T_{\mathrm{eff}}}{300}\right) \\ &+1.073 \times 10^{-12}\left(\frac{T_{\mathrm{eff}}}{300}\right)^2 - 5.17 \times 10^{-14}\left(\frac{T_{\mathrm{eff}}}{300}\right)^3 \\ &+9.65 \times 10^{-16}\left(\frac{T_{\mathrm{eff}}}{300}\right)^4 \quad 300 < T_{\mathrm{eff}} \le 6000°K \end{aligned} \tag{1.9}$$

where $T_{\mathrm{eff}}\,(= (T_{\mathrm{i}} + T_{\mathrm{n}})/2)$ is the effective temperature, which is based on the ion temperature T_{i} and neutral temperature T_{n}.

In the ionosphere, the relationship between the ion-neutral temperatures and

ion-neutral relative velocities is expressed as follows (e.g., see Chapter 5 in *Schunk and Nagy* [2009] for the derivation of formula):

$$T_{\mathrm{i}} = T_{\mathrm{n}} + \frac{m_{\mathrm{n}}}{3k}(\boldsymbol{V}_{\mathrm{i}} - \boldsymbol{V}_{\mathrm{n}})^2 \tag{1.10}$$

where m_{n} is the mean neutral mass, k is the Boltzmann constant, and $(\boldsymbol{V}_{\mathrm{i}} - \boldsymbol{V}_{\mathrm{n}})$ is the ion-neutral relative velocity.

For simplicity, assuming here that the neutral temperature and velocity do not change very much, we find that the enhanced convection flow leads to increased T_{i}. This heating process caused by the enhanced convection flow is called frictional heating, which is considered to be the predominant heating process in the F-region ionosphere. Thus, the high-speed convective flow of the high-latitude ionosphere increases the T_{i} because of frictional heating and that increased T_{i} promotes dissociative recombination. Figure 1.10 shows a profile of the dissociative recombination rate β against the effective temperature. As shown in the figure, β increases with temperatures above ~1100 K, which indicates that frictional heating decreases electron density through dissociative recombination during high-speed convection.

1.3 Ionospheric trough

The ionospheric trough in the F region is characterized by a band of depleted electron density that extends longitudinally around the nightside subauroral/auroral region of Earth. Under geomagnetically quiet and moderate conditions, the overall trough structure is composed mainly of a high-latitude domain and a mid-latitude domain. Figure 1.11 shows the location of the quiet-time troughs [after *Rodger et al.*, 1992]. In the high-latitude ionosphere, there are three regions of decreasing electron density: the

high-latitude trough (A), mid-latitude trough (B), and polar hole (C). In this paper, we focus on the high- and mid-latitude troughs. Here, we introduce the basic mechanisms of their generation and review past publications.

The high-latitude trough is usually accompanied by an increase in ion temperature (T_i) caused by high-speed convective flow [e.g., *Williams and Jain*, 1986; *Collis and Häggström*, 1988], such that the trough is commonly regarded to form by dissociative recombination accompanied by frictional heating. Additionally, the effects of upward ion flow (accompanied by frictional heating) on the high-latitude trough have also been investigated in relation to the overall trough-density structure [e.g., *Winser et al*., 1986]. As a result, many previous studies share a common interpretation that this mechanism alone cannot account for the observed drop in electron density in the F region [e.g., *Williams and Jian*, 1986; *Winser et al*., 1986].

Conversely, the mid-latitude trough is present in the subauroral region and it is generally considered to form via ordinary loss processes involving recombination in darkened regions of stagnated plasma flow (see red ellipse in Figure 1.11). Consequently, the mid-latitude trough is not accompanied by a similar increase in T_i because no frictional heating occurs. Several researchers have studied the relationship between nighttime convection patterns and the formation of the mid-latitude trough. *Spiro et al*. [1978] proposed that this trough forms because of stagnation of plasma around the duskside, where the return flow meets the co-rotating ionospheric plasma. Using a numerical convection model, *Sojka et al*. [1983] demonstrated that the mid-latitude trough forms in the nightside and extends past the terminator to the high-latitude dusk region. Furthermore, *Whalen* [1989] suggested that high-density plasma in the region of the dawn and dusk cells could be displaced by low-density nighttime plasma via sunward convective transport.

It has often been pointed out that small-scale structures or irregularities in the electron

density are produced within the trough region during geomagnetic active conditions, which affect the Global Navigation Satellite System (GNSS)-based navigation systems [e.g., *Basu et al*., 2008]. The Doppler and delay spread of HF signals, which are often caused by scattering or reflection from irregularities, are more frequent within the trough region during a sunspot maximum than during a sunspot minimum [*Stocker and Warrington*, 2011]. The scale size of the irregularities can range from tens of kilometers down to hundreds of meters, and large-scale structures called "blobs," in the scale length range of hundreds of kilometers, are considered to be the main source of the irregularities [e.g., *Tsunoda*, 1988]. However, the detailed process of their generation is still unclear because of the lack of adequate observations. Therefore, it is highly desirable that the processes associated with such small-scale structures within the trough be understood.

1.4 Plasma instabilities

The state of plasma fluid can be categorized roughly into the following two types: stable mode (or equilibrium) and unstable mode. The nature of this plasma stability can be explained through a simple analogy of a ball that is placed in a valley (stable state) or on the top of a hill (unstable state). If the ball is in the valley, from which no realistic perturbation can lift it away, the system is stable. After an initial perturbation, the ball returns to its equilibrium position. It may oscillate around the bottom of the valley for a long time if damping of the oscillation is weak. However, if the ball is at the summit of the hill, any perturbation will move it away from its position and the system is unstable. In such a situation, a small perturbation in the plasma fluid will grow or oscillate. Plasma instabilities grow by many types of mechanisms. In particular, it is known that the Kelvin–Helmholtz (K–H) instability and gradient drift (G-D) instability are

predominant in the high-latitude F region. As explained in Section 1.3, small-scale structures in the electron density are often observed within/around the trough region. Such structures are thought to be produced through the K–H instability and/or G-D instability around the trough region [e.g., *Keskinen and Ossakow*, 1983; *Keskinen et al.*, 1988]. Here, we introduce the above two mechanisms that are associated with the discussion in Chapter 4.

The K–H instability is known to be the instability driven by the velocity difference (or flow shear) in the convection. As plasma convection exists in the polar ionosphere, the velocity differences in the plasma convection are observed inside and outside of the trough region. Hence, it is possible that such velocity differences influence the trough structure through the K–H instability. Figure 1.12 shows a schematic illustration of K–H instability in the high-latitude F region where the plasma flow is directed in the x-direction, an applied electric field is in the y-direction, a geomagnetic field line is in the z-direction, and L is the width of the shear region [after *Keskinen et al.*, 1988]. Note that here we simplify the condition, although other factors such as the neutral wind are also involved in the real ionosphere. The linear growth rate of the K–H instability can be estimated from the work by *Keskinen et al.* [1988]. Accordingly, for ionospheric applications, the linear growth rate γ_{KH} can be expressed by the following equation:

$$\gamma_{\mathrm{KH}} = 0.2\,\Delta V/L \tag{1.11}$$

Thus, the growth time τ_{KH} can be obtained by $5\,L/\Delta V$, which is the inverse of the growth rate. This means that the K–H instability grows more rapidly with stronger flow shear and narrower shear width.

Figure 1.13 describes a simplified schematic diagram of the G-D instability with a plasma density gradient directed in the x-direction, an applied electric field in the

y-direction, and a geomagnetic field line in the z-direction [from *Tsunoda*, 1988]. Given the above geometry, the positive feedback loop of the G-D instability operates as follows. When a perturbation pattern is imposed on the plasma density contours, the ions drift to the right along the background electric field $\vec{E}_0$ (represented by the solid curve) leaving the highly magnetized electrons (dashed curve) behind. The resulting charge separation is accompanied by a polarization of the electric field $\vec{E}_p$. The $\vec{E}_p \times \vec{B}$ motion is in a direction such that the initial perturbation is amplified by moving plasma that is less dense further into regions of plasma that is more dense, and vice versa. Since the charge separation is produced through the large Pedersen mobility (mobility of the y-direction) of the ions as compared to that of the electrons, it becomes small in the F region where the Pedersen mobility of the ions is relatively small. As a result, the growth rate of the G-D instability is small in the F region.

1.5 Objectives of this thesis

Most previous studies on the trough have been based upon event investigations and statistical analyses that focus solely on electron density; thus, little is known about the predominant processes associated with trough formation on various time scales. In particular, the rapid temporal variation on a time scale of minutes within the trough region has not been investigated because of the lack of adequate observations. Therefore, there are many unsolved issues remaining in regards to the trough formation. Hence, the goal of this thesis was to develop an understanding of the processes associated with the trough's structural change on several time scales, focusing especially on long-term (seasonal and solar activity) and short-term (60–80 seconds) variations.

The seasonal variation and solar activity dependence of the trough were investigated based upon the European Incoherent Scatter (EISCAT) radar dataset from 1982 to 2011, which encompasses about three solar cycles. In this research, we focused on the

variation of the trough's occurrence rate and frictional heating accompanied by seasonal variation and solar activity dependence. The details of the approach used and the results obtained are described in Chapter 3.

The study on the rapid temporal evolution within the trough region required a new technique of Incoherent Scatter (IS) radar observation. Thus, we conducted new EISCAT radar observations as part of the Peer-reviewed Program (PP) and Japanese Special Program (SP) during October and December 2013, and we obtained data for nine events that each lasted for a period of 4 hours (14:00–18:00 UT, MLT $\simeq$ UT + 2.2 h). In this research, we focused on localized plasma density enhancement, or so-called blobs, within the trough region, and then discussed the process of blob deformation. The details of the approach used and the obtained results are described in Chapter 4.

2 Instruments

This thesis reports on two major avenues of research (details are presented in Chapter 3 and Chapter 4), both of which have been conducted based on EISCAT radar data; however, other complementary observational data have been used. In this chapter, we introduce the instruments used in obtaining the data for this thesis work.

2.1 EISCAT radar

In general, observations by IS radars, including the EISCAT UHF radar system, are based upon Thomson scattering (see Section 6.1). The transmitter of the EISCAT UHF radar system is located in Tromsø, northern Norway (69°35'N, 19°14'E, Invariant Latitude: 66°12'N). Signals scattered from the ionosphere are received at stations in Kiruna, Sweden (67°52'N, 20°26'E, Invariant Latitude: 64°27'N) and Sodankyla Finland (67°22'N, 26°38'E, Invariant Latitude: 63°34'N), as well as at the transmitting site. In addition, another EISCAT radar is located in Svalbard, Norway (78°09'N, 16°03'E, Invariant Latitude: 75°10'N). Figure 2.1 shows the locations of the EISCAT radars.

From the spectrum shape of the IS signal, the plasma parameters (electron density, ion/electron temperature, and line-of-sight ion drift velocity) can be determined within the altitude range ~70–1000 km. We explain how the plasma parameters are determined from the spectrum shape of the IS signal in Section 6.2. By combining the line-of-sight ion velocities derived from the three stations that observe the same ionospheric volume, the three-dimensional ion velocity vector can be computed, and hence, the electric field that causes the $\mathrm{E} \times \mathrm{B}$ drift above ~200 km can be determined. As the trough usually stretches over a wide range of latitude, we used data from the meridional scanning observations of the EISCAT UHF radar. For the statistical analysis introduced in Chapter 3, we used the EISCAT Common Program 3 (CP-3) dataset that takes ~30

minutes for a single scan. The EISCAT CP-3 scan is a meridional scanning mode that follows a geomagnetic north–south trajectory during a single scan. Figure 2.2 shows a schematic illustration of the trough observed by the EISCAT CP-3 scan. Although this observational technique can follow relatively slow variations of the trough, such as seasonal variation or solar activity dependence, it is insufficient for observing more rapid temporal evolutions. Therefore, we used a high-speed meridional scan mode for the research, which is introduced in Chapter 4; its temporal resolution is 60–80 seconds, i.e., ~25 times higher than that of the CP-3 scans.

2.2 GPS-TEC

The Global Positioning System (GPS) is a measurement system composed of a constellation of 24 orbiting satellites. They emit continuous navigation signals on two different L-band frequencies (L1-band and L2-band) to ground-based GPS receivers. More than 1000 ground-based GPS receivers monitor the signals from the GPS satellites within their field of view, and thus, each GPS receiver can obtain the GPS signals in the visible area. A GPS signal is delayed during ionospheric propagation depending on the transmitting frequency and ionospheric electron density; therefore, from one transmission it is possible to obtain two delay times derived from the L1- and L2-band frequencies. As each individual delay time involves information regarding ionospheric electron density, we can calculate the total electron content (TEC) along the signal path from these two delay times. We introduce the details of the TEC calculation in Section 6.3.

As explained above, each GPS receiver can obtain the TEC value for each transmission, which means that we can construct maps of TEC values by combining data from the GPS receivers. Thus, the TEC maps alone can provide a large-scale

visualization of the temporal evolution of the ionospheric density structure. Figure 2.3 shows examples of the TEC maps [from *Zhang et al.*, 2013]. The color scale runs from high-electron density (red) to low-electron density (blue). The dotted line across each panel is the day–night terminator at 100-km altitude. The blue circles and ellipses highlight the polar cap patch, the evolution of which is followed in this figure.

2.3 IMAGE magnetometers

The International Monitor for Auroral Geomagnetic Effects (IMAGE) consists of 31 magnetometer stations maintained by 10 institutes from Estonia, Finland, Germany, Norway, Poland, Russia, and Sweden. Figure 2.4 shows the locations of the IMAGE magnetometer stations (see station information at http://space.fmi.fi/image/beta/?page=maps). It is known that ionospheric currents accompanied by auroral activity flow in the E-region. As the ground magnetometers observe the geomagnetic variations caused mainly by the E-region Hall current, we can estimate the equivalent current from the magnetometer data [e.g., *Iijima and Nagata*, 1972]. Since the F-region drift vectors roughly go in the opposite direction from the E-region Hall current, we used data from the meridional chain stations to estimate the F-region drift vectors around the EISCAT observation range. Note that the perpendicular component of the field-aligned current and geomagnetic variation derived from the Pedersen current cancel out each other, and thus, the geomagnetic variation on the ground comes from only the Hall current in principle [*Fukushima*, 1976]. Hence, the estimated drift vectors from the IMAGE magnetometer can be used as a proxy of the real F-region convection.

3 Seasonal variation and solar activity dependence of the quiet-time ionospheric trough

3.1 Introduction

Statistical studies dealing with the seasonal variation of the trough can be found in a number of papers [*Mallis and Essex*, 1993; *Horvath and Essex*, 2003; *Voiculescu et al.*, 2006; *Lee et al.*, 2011]. For example, *Lee et al.* [2011] analyzed the seasonal dependence of the mid-latitude trough using the GPS Occultation Experiment data of FORMOSAT-3/COSMIC, which covers the period from February 2008 to January 2009, and showed that its electron-density structure changed dramatically in each season. *Vo and Foster* [2001] used Millstone Hill incoherent scatter radar data obtained between 1982 and 2000 to investigate the spatial extent and temporal evolution of the total electron content (TEC) at middle and subauroral latitudes. They showed that the latitudinal gradients in TEC associated with the equatorward wall of the trough are appreciably larger during a solar maximum than during a solar minimum. However, the processes responsible for the changes in the latitudinal gradients of the trough remain unclear.

As briefly mentioned in Section 1.3, radio propagation is affected by irregularities within the trough region. *Stocker and Warrington* [2011] reported that the Doppler and delay spread of HF signals, which are often caused by scattering or reflection from irregularities within the trough, are more frequent during a sunspot maximum than during a sunspot minimum. As these studies show that both electron density and the occurrence rate of the trough show significant variations depending on the season and solar activity, a detailed and unified investigation of these factors is required to fully

understand the trough's basic characteristics.

In this chapter, we investigate the seasonal variation and solar activity dependence of the mid- and high-latitude troughs using an in-depth statistical analysis. Based on the EISCAT dataset from 1982 to 2011, which covers about three solar cycles, we then discuss the physical and chemical processes related to the evolution of the trough. To evaluate the occurrence rate of the trough (discussed later), we must differentiate the variation in the occurrence rate caused by seasonal variation and solar activity dependence from that caused by a change in the trough location. Given that the trough location changes according to auroral activity, whereby it shifts toward the equator as the Kp index increases [e.g., *Moffett and Quegan*, 1983; *Rodger et al*., 1992], we have used a dataset obtained under quiet and moderate geomagnetic conditions (Kp ≤ 3-), which can be considered as low auroral activity.

3.2 Data analysis

This study utilized a dataset obtained by the European Incoherent Scatter (EISCAT) UHF radar located in Tromsø, northern Norway (69°35'N, 19°14'E, Invariant Latitude: 66°12'N), which enabled us to observe ionospheric plasma parameters (electron density, ion/electron temperature, and line-of-sight ion drift velocity) in the altitude range of ~70–1000 km. In the present study, we must deal with all plasma parameters at the same altitudes, within the limitations of our statistical analysis; thus, we cannot eliminate the influence of hmF2 displacement accompanied by seasonal and solar activity variation. We used average plasma parameters between altitudes of 300 km and 350 km (near hmF2) to reduce the influence of hmF2 displacement. For long-term data analysis of the trough, we used the EISCAT dataset from 1982 to 2011, which covers about three solar cycles.

To visualize trough structures over a wide range of latitudes, we used scan data from EISCAT Common Program 3 (CP-3), as detailed in Table 3.1. This scanning mode follows a geomagnetic north–south trajectory during a single scan and covers a range of geomagnetic latitudes from approximately 73°N to 60.5°N at an altitude of 325 km. Since each scan takes ~30 min to complete, the EISCAT radar moves ~291 km eastward with the rotation of the Earth in non-rotating coordinates during a single scan. Therefore, 48 repetitions of the CP-3 scan obtain a physical quantity of plasma amounting to once around the earth. The different beam patterns and pulse codes used by the CP-3 scan are listed in Table 3.1. Its spatial resolution is dependent on these combinations, but all CP-3 scans can obtain a latitudinal distribution covering ~12.5° at an altitude of 325 km. The width of the ionospheric trough is generally less than 10° [e.g., *Collis and Häggström*, 1988], so we consider that either a part of or the entire trough can be identified in the CP-3 scan data if the trough is located within the EISCAT field of view (FOV). An example of a trough measurement made by the CP-3 scan on October 26, 1988 is shown in Figures 3.1a–3.1c. Figure 3.1a shows the electron-density structure obtained from a single CP-3 scan on a dusk sector (16:00–16:26 UT). Here, the trough is characterized by a region of decreasing electron density around 67°N–69°N at an altitude of 250–500 km, represented by the dark-green/blue-colored grid squares. Figure 3.1b shows the latitudinal distribution of electron density (black line), which was derived by averaging electron density along the geomagnetic field line within the 300–350 km altitude range (red box in Figure 3.1a). Figure 3.1b contains a black shaded region that represents the extent of the trough, as determined using a detection algorithm (described below). A plausible background electron density (red dashed line in Figure 3.1b) was obtained by the following calculation. First, to determine the background electron density, we sorted the electron density values of the latitudinal distribution, generally 15–16 points, in ascending order. Then, we defined the median

value of the upper half of the data sequence obtained from the sorting process as the background electron density. We were able to determine a plausible background electron density in a situation where the latitudinal width of the trough was less than three-fourths of the scanning width. However, as this background electron density was identified solely by the latitudinal distribution of the CP-3 scan, it does not necessarily reflect the true value of the ionospheric background. These data show that the trough exhibits an electron density up to 90% lower than background levels, with a rate of decrease of ~30% per degree of latitude. In addition, the orange line in Figure 3.1b represents the electron-density variation measured at 14:40–14:56 UT on October 29, 1986, a similar time and month to the electron density data collected on October 26, 1988 (black line), but the orange-colored line was not detected at the trough as the solar zenith angle (SZA) is > 90°. This shows that the trough does not always form, even in regions with no sunlight. The rate of decrease along the orange line is ~11% per degree of latitude, which is, notably, only one-third of the rate of decrease for the trough itself (black line). We ignored gradual electron-density variations such as those shown by the orange line by considering them not as troughs, but as structures associated with diurnal variation.

We identified the trough region using a detection algorithm that exploits the fact that the trough, in particular the mid-latitude trough, is longitudinally elongated but latitudinally narrow. As a result, it covers several hours of magnetic local time (MLT), but only a few degrees of geomagnetic latitude (MLat). Therefore, we were able to identify the electron density variation in the trough by evaluating the latitudinal distribution, as shown in Figure 3.1b. We defined a region of decreasing electron density, the minima of which were at least 20% lower than the background value; this region was then identified as the trough region. Our data confirm that a 20% decrease is sufficient to distinguish the trough events from the non-trough events, with this value

able to detect trough events referred to in past studies [e.g., *Collis and Häggström*, 1988; *Voiculescu et al*., 2010]. Additionally, to verify this threshold, we showed that the trough characteristics detailed below (Section 3.3) did not change upon increasing this value, i.e., that the trough characteristics could be obtained using a threshold of just 20%.

Figure 3.1c shows the electron-density structure in MLT–MLat coordinates for the same day derived from 48 scans of the latitudinal distribution. Red-boxed regions indicate grid cells that correspond to the variation in electron density shown in Figure 3.1b. Dashed black lines represent the solar terminator, where SZA = 90°, and solid black lines indicate the latitudinal widths of the detected troughs. Here, the Altitude Adjusted Corrected GeoMagnetic coordinates (AACGM) system was used to calculate MLat. Note that we calculated MLT by using a simple conversion (MLT = UT + 2.5 hours) for ease of statistical analysis. Finally, Figure 3.1d shows the ratio of electron density decrease in the trough to the background electron density.

3.3 Results

Figure 3.2 shows the occurrence rates of the trough according to season and F10.7. These data have been divided into nine scenarios, each characterized by one of three seasons and one of three solar activities. For each grid cell, the occurrence rate (R) can be defined as follows:

$$\mathrm{R}\ (\mathrm{MLT}, \mathrm{MLat}, \mathrm{F10.7}, \mathrm{season}) = \frac{\mathrm{n}\ (\mathrm{MLT}, \mathrm{MLat}, \mathrm{F10.7}, \mathrm{season})}{\mathrm{N}\ (\mathrm{MLT}, \mathrm{F10.7}, \mathrm{season})} \qquad (3.1)$$

where n (MLT, MLat, F10.7, season) is the number of trough detections in each grid cell and N (MLT, F10.7, season) is the total number of events in each grid cell. The total

number of events N does not depend on MLat because one latitudinal distribution, i.e., a set of grid cells of that latitude, is used for one trough detection. Thus, the total number of events N is expressed as $\mathrm{N}\ (\mathrm{MLT}, \mathrm{F10.7}, \mathrm{season})$, not $\mathrm{N}\ (\mathrm{MLT}, \mathrm{MLat}, \mathrm{F10.7}, \mathrm{season})$. Each annual period was divided into three periods (seasons): winter (±1.5 months around the winter solstice), summer (±1.5 months around the summer solstice), and the equinox (the remainder of the year). Note that Kp indices were limited to geomagnetically quiet and moderate conditions (Kp ≤ 3-), as explained in Section 3.1. These data show that the occurrence rate decreases from winter to summer (with decreasing SZA) for all solar activities. No data were available for winter during F10.7 = 180–300 solar flux unit (sfu) owing to the very limited number of samples. The occurrence rate appears to be maintained on the high-latitude side of the FOV (65°–72° MLat), even in the sunlit regions, whereas it is almost zero on the low-latitude side of the FOV (61°–65° MLat). Nevertheless, the relationship between the occurrence rate and F10.7 is not obvious, although it is clear that the occurrence rate varies with F10.7 in darkened regions.

As an example, Figure 3.3 presents the relationship between the occurrence rate and average description of the trough under the same conditions as in Figure 3.2e. In these figures, each panel indicates (a) the occurrence rate of the trough with overplotted ion drift velocity ($\boldsymbol{V}_{\mathrm{i}}$) and (b) the ion temperature variation (ΔT_{i}) in the trough. Red arrows shown in Figure 3.3a indicate eastward ion flows, whereas black arrows indicate westward ion flows. Each colored grid cell mapped on the polar plot has a resolution of 0.5 MLT and 0.6–0.8 MLat; however, grid cells containing fewer than four samples were displayed as blank areas. Note that most of the ion velocity vectors were calculated at heights of 275 km from tristatic observations, so the height of overplotted $\boldsymbol{V}_{\mathrm{i}}$ is around 50 km below that of the occurrence rate and ΔT_{i}.

Figure 3.3a shows that the strong eastward and westward flows exist on the

high-latitude side of the FOV, which are up to ~600 m/s. The value of V_{i} tends to be smaller than ~100 m/s on the low-latitude side of the FOV. It appears that the occurrence rate increases up to ~80% along the return flow during 14:00–22:00 MLT, and additionally during 01:00–06:00 MLT. Moreover, it also increases up to ~80% in the region of small convection flow during 21:00–08:00 MLT on the low-latitude side of the FOV. Conversely, the occurrence rate decreases considerably down to ~10% during 22:00–01:00 MLT on the high-latitude side of the FOV, which is located approximately in the region of the Harang reversal (light blue in Figure 3.3a). The results also suggest that the occurrence rate is particularly low (< ~20%) during 00:00–07:00 MLT at 65°–67° MLat. Figure 3.3b demonstrates that ΔT_{i} is greater than ~0 K on the high-latitude side of the FOV along the region of the return flow, but it is less than ~0 K on the low-latitude side of the FOV. Here, ΔT_{i} in the trough is derived from the following simplified energy equations:

$$T_{\mathrm{i}} = T_{\mathrm{n}} + \frac{m_{\mathrm{n}}}{3k}(\boldsymbol{V}_{\mathrm{i}} - \boldsymbol{V}_{\mathrm{n}})^2 \Leftrightarrow T_{\mathrm{i}} - T_{\mathrm{n}} = \frac{m_{\mathrm{n}}}{3k}(\boldsymbol{V}_{\mathrm{i}} - \boldsymbol{V}_{\mathrm{n}})^2 \tag{3.2}$$

$$\Longrightarrow \Delta T_{\mathrm{i}} = T_{\mathrm{i}} - T_{\mathrm{n}} \simeq T_{\mathrm{i\,(trough)}} - T_{\mathrm{i\,(non-trough)}} \tag{3.3}$$

where T_{n} in a neutral temperature, m_{n} is the mean neutral mass, k is the Boltzmann constant, and $(\boldsymbol{V}_{\mathrm{i}} - \boldsymbol{V}_{\mathrm{n}})$ is the ion-neutral relative velocity. We have presumed that T_{n} is approximately equal to T_{i} within the non-trough region in our statistical cases. Then, assuming that V_{n} is equal to zero, ΔT_{i} turns out to be nearly proportional to the square of V_{i}, which is derived from Equation 3.2. *Aruliah et al.* [1996] demonstrated average neutral wind at the F region over Kiruna, Sweden, using the FPI dataset, which contains 9 years of observational data. According to their results, average neutral wind varies significantly around 0–100 m/s throughout the day under geomagnetically quiet to

moderate conditions. Thus, the error in ΔT_{i} is within approximately ±100 K, even in the region of increased convection. On the whole, the ΔT_{i} shown in Figure 3.3b increases with V_{i}, providing support that the above assumption is reasonable. It is known that T_{i} is typically increased in the high-latitude trough with frictional heating due to return flow, whereas it is not increased in the mid-latitude trough under geomagnetically quiet and moderate conditions [e.g., *Moffett and Quegan*, 1983; *Williams and Jian*, 1986; *Ma et al.*, 2000]. Thus, it is considered that the region of increased T_{i} reflects frictional heating in the high-latitude trough. Note that ΔT_{i} in the trough is not always smaller than ~0 K on the low-latitude side of the FOV because the mid-latitude trough also experiences significant frictional heating due to the subauroral polarization stream (SAPS) under geomagnetically active conditions, which spans the nightside from dusk to the early morning sector for all K_{p} greater than 4 [e.g., *Foster and Vo*, 2002]. In our case, however, the primary source of increased T_{i} is return flow located on the high-latitude side of the FOV because the occurrence rate of SAPS is low under geomagnetically quiet and moderate conditions.

3.4 Discussion

3.4.1 Seasonal variation

Figure 3.4 presents the seasonal variation in the ratio of the ΔT_{i} within the trough (hereafter referred to as the ΔT_{i} ratio), and the MLT distributions on both the high-latitude (upper panels) and low-latitude (lower panels) sides of the FOV are shown. Here, we defined the range of 65°–72° MLat and 61°–65° MLat as the high-latitude and low-latitude side of the FOV, respectively, as mentioned in Section 3.3. The left, middle, and right columns show the results for the winter, equinox, and summer seasons, respectively. The color bar has four sectors: blue ($\Delta T_{\mathrm{i}} < 200\ K$), yellow ($\Delta T_{\mathrm{i}} = 200 -$

500 K), orange ($\Delta T_{\mathrm{i}} = 500 - 1000$ K), and red ($\Delta T_{\mathrm{i}} > 1000\ K$). Early studies used an increase in the F-region parallel T_{i} exceeding 100 K to identify frictional heating events [*McCrea et al*., 1991; *Davies et al*., 1997]. However, the T_{i} values deduced by incoherent scatter fitting typically contain error in the high-latitude trough region [*Häggström and Collis*, 1990]. Therefore, in the present study, we regard $\Delta T_{\mathrm{i}} \geq 200$ K as an indicator of frictional heating, since any error is within approximately ±100 K under geomagnetically quiet and moderate conditions. As seen in Figure 3.3b, the behavior of ΔT_{i} is different between the high- and low-latitude sides; accordingly, we can discuss both sides separately.

The upper panels in Figure 3.4 show that the warm-colored bars (comprising yellow, orange, and red), which mean increased T_{i} by frictional heating, are larger than ~85% in the post-midnight region (00:00–06:00 MLT) in all seasons. This means that a large part of the troughs are accompanied by large variations of T_{i} produced by frictional heating of eastward return flow, as shown in Figure 3.3b. Figure 3.2 demonstrates that the occurrence rate is maintained at 80–90% in the post-midnight high-latitude region, even in summer, whereas it decreases significantly from winter to summer in other sectors. Hence, we conclude that dissociative recombination accompanied by frictional heating tends to cancel out any increases in the production rate due to increased solar EUV, such that the electron density trough can survive even in sunlit regions. In winter, however, the MLT distribution of the ΔT_{i} ratio is not consistent with the occurrence rate shown in Figure 3.2. Increased T_{i} is dominant near the midnight sector (21:00–06:00 MLT), whereas the occurrence rate of the trough increases in the dayside rather than the midnight sector. Therefore, it is possible that other physical and/or chemical processes are involved in controlling the trough formation, especially in darkened regions. *Sojka et al*. [1983] reported the results of numerical modeling of plasma transportation, which indicate that the duskside trough formed primarily owing

to transport of the nightside low-density plasma to the dayside. Thus, one interpretation of the discrepancy between the occurrence rate and the location of frictional heating during winter is that the plasma convection roughly determines the trough location, and consequently, it influences the occurrence rate. Another feature identified is the variation in the ΔT_{i} ratio. In all seasons, increased T_{i} is dominant near the midnight sector and it decreases toward the dayside. As shown in Figure 3.3a, the location of return flow moves to the outside of the poleward boundary of the FOV, which can lead to a decrease in the frictional heating rate from near the midnight to the dayside. Thus, it can be considered that ΔT_{i} in the trough also decreases toward the dayside. Additionally, the ratio of increased T_{i} decreases from winter to summer, with a particularly pronounced decreases (30–40%) in the dayside (e.g., 12:00–15:00 MLT; 09:00–12:00 MLT). The neutral density increases from winter to summer, which leads to an increase in the ion drag force on the neutral atmosphere; consequently, the term $(\boldsymbol{V}_{\mathrm{i}} - \boldsymbol{V}_{\mathrm{n}})$ of Equation 3.2 decreases, which leads to a decrease in ΔT_{i}. Therefore, we suggest that an increase in the ion drag force on the neutral atmosphere from winter to summer causes a decrease in ΔT_{i} in the trough.

The lower panels in Figure 3.4 demonstrate that the warm-colored bars decrease from winter to summer over all MLT sectors. Thus, it can be assumed that an increase in ion drag force from winter to summer suppresses an increase in ΔT_{i}, as explained above. Furthermore, from the summer panels, it is clear that the sum of the warm-colored bars of the upper panel amounts to ~66% of the total; this proportion is ~47% greater than that of the lower panel. In other words, this indicates that there is a major difference in the ratio of frictional heating between the high- and low-latitude sides during summer. Furthermore, Figure 3.2 illustrates that the occurrence rate of the trough decreases down to ~10% on the low-latitude side of the FOV during summer. Therefore, we posit that the trough cannot survive without frictional heating in sunlit regions.

3.4.2 Solar activity dependence

Figure 3.2 shows that the occurrence rate varies with F10.7. To evaluate the variation in the occurrence rate in a more quantitative way, we compared occurrence rates in each season using values obtained by averaging all grid cells over a two-hour period (Figure 3.5) and plotted the MLT distribution of the occurrence on the high-latitude (upper panels) and low-latitude (lower panels) sides of the FOV. The left, middle, and right columns show the results for the winter, equinox, and summer seasons, respectively. The blue, green, and orange dotted lines shown in each panel denote the variation in the occurrence rate at F10.7 = 0–90 sfu, F10.7 = 90–180 sfu, and F10.7 = 180–300 sfu, respectively. The error bars indicate the standard deviation centered on the mean value.

During winter, when the darkened region covers the EISCAT FOV almost entirely, the occurrence rate changes little with F10.7 in the pre-midnight to post-midnight region (16:00–06:00 MLT), where it decreases significantly (by nearly 20–50%) with F10.7 in the dayside (07:00–16:00 MLT). It is reasonable to suppose that solar EUV makes a greater contribution to ionization for higher values of F10.7, thus leading to a decrease in the occurrence rate in the dayside. For the pre-midnight to post-midnight region, it is evident that the occurrence rate of the upper panel varies nearly symmetrically with that of the lower panel. The upper panel shows that the occurrence rate decreases down to ~20% within the pre-midnight region (18:00–00:00 MLT); this is ~30% lower than the rate in the midnight region (00:00 MLT). Conversely, the occurrence rate appears to increase up to ~80% in the post-midnight region (00:00–06:00 MLT), such that it is about 30% higher than that in the midnight region. In contrast to the upper panel, the lower panel of Figure 3.5 demonstrates that the occurrence rate increases up to ~80% within the pre-midnight region, such that it is ~30% higher than that in the midnight

region; conversely, it decreases down to ~20% in the post-midnight region, such that it is about 30% lower than that in the midnight region. Here, we presume that the increase/decrease in electron density accompanied by upward/downward field-aligned currents (FACs) can contribute to the formation of the F-region trough. Then, it can be assumed that the region 1 (R1) FAC causes the variation in occurrence rate in the upper panel, whereas the region 2 (R2) FAC causes that in the lower panel (red and blue shaded areas of winter in Figure 3.5). A relationship between the F-region trough and downward FACs has been indicated in some model works and observational evidence [e.g., *Doe et al.*, 1995; *Nilsson et al.*, 2005; *Zou et al.*, 2013]. Thus, it is perhaps unsurprising that the increase/decrease in electron density caused by FACs could have an impact on the occurrence rate of the F-region trough.

Next, we focus on the occurrence rate in the equinox period. The upper panel of Figure 3.5 shows that the occurrence rate decreases by 20–30% with increasing F10.7 within the pre-midnight to post-midnight region (21:00–02:00 MLT), whereas it increases by 20–30% with increasing F10.7 within the post-midnight to morning region (02:00–07:00 MLT). Conversely, the lower panel shows that the occurrence rate increases by 30–40% with increasing F10.7 within the pre-midnight to post-midnight region and decreases by 40–50% with increasing F10.7 within the post-midnight to morning region. Subsequently, the occurrence rate varies with F10.7; consequently, the proportion of the occurrence rate is very similar to that in winter under high solar activity. *Ohtani et al*. [2014] showed that FACs are more intense during higher solar activity in the nightside. Therefore, it could be assumed that the variation in the occurrence rate with F10.7 during the equinox is a manifestation of solar activity dependence on FACs.

During summer, it can be recognized that the peak of the occurrence rate is located around 04:00 MLT in the upper panel of Figure 3.5. However, we cannot identify solar

activity dependence on the occurrence rate during summer. It is possible that high ionization rates in summer tend to suppress the formation of the trough, which presumably cancels out the solar activity dependence.

We also found that trough depth and frictional heating depend on solar activity. Figure 3.6 presents the MLT distributions of several parameters on the high-latitude side of the FOV, as in Figure 3.5: (a) trough depth and (b) T_i within the trough. The trough depth is the ratio of electron density in the trough to the background electron density, as shown in Figure 3.1d. Figure 3.6a illustrates that the trough depth increases by 10–30% with increasing F10.7 within the post-midnight to morning (01:00–09:00 MLT) and dayside to duskside (12:00–16:00 MLT) regions during equinox, and within the midnight to morning region (00:00–09:00 MLT) during summer, as indicated by shaded areas. It is also clear that T_i in the trough increases by 200–800 K with increasing F10.7 over the MLT sectors in which the trough deepens with increasing F10.7, as shown in Figure 3.6b. However, this characteristic is not obvious in winter. These data indicate that the trough becomes deeper via dissociative recombination caused by increased T_i with increasing F10.7, at least during the equinox and summer seasons (but not winter). Now, focusing on the occurrence rate on the high-latitude side of the FOV during equinox (Figure 3.5), it can be seen that the post-midnight to morning region (02:00–07:00 MLT) where the occurrence rate increases with increasing F10.7 corresponds to the MLT sector where the trough depth and T_i increases with increasing F10.7 (Figures 3.6a and 3.6b). As explained in Section 3.2, the regions of decreasing electron density, the minima of which were at least 20% lower than the background value, are detected in this study. Thus, the occurrence rate tends to be high within the region that the trough tends to become deep. In this respect, it can be considered that an increase of the occurrence rate within the post-midnight to morning region during equinox is caused by not only the FACs effect but also the enhanced dissociative

recombination caused by frictional heating.

3.5 Summary and conclusion

A long-term statistical analysis of the ionospheric trough in relation to seasonal variation and solar activity dependence has been conducted using EISCAT UHF radar data collected during 1982–2011. In this study, we have focused on the plasma parameters in the F region at altitudes of 300–350 km. In addition, we have used a dataset obtained under quiet and moderate geomagnetic conditions (Kp ≤ 3-). The main results obtained regarding the seasonal variation of the trough characteristics/occurrence/parameters are summarized as follows.

1. On the high-latitude side of the FOV (65°–72° MLat), the ratio of increased T_{i} due to frictional heating ($\Delta T_{\mathrm{i}} \geq 200\ K$) is larger than ~85% in the post-midnight region (00:00–06:00 MLT) owing to eastward return flow in all seasons. Moreover, there is a major difference in the ratio of frictional heating between the high- and low-latitude sides of the FOV during summer, with frictional heating ~47% higher on the high-latitude side. Based on comparisons of the occurrence rate with the ratio of frictional heating, we conclude that dissociative recombination accompanied by frictional heating is the main cause of trough formation in sunlit regions.
2. The increase in T_{i} is suppressed from winter to summer, most likely owing to frictional heating being suppressed by increased ion drag force on the neutral atmosphere in summer.

The main results concerning the dependence on solar activity are summarized as follows.

3. During the winter and equinox seasons, the variation in the occurrence rate suggests the possibility that FACs modulate the occurrence rate of the F-region trough. Accordingly, the effects of FACs become dominant with increasing F10.7 during equinox. During summer, however, we could not confirm any solar activity dependence on the occurrence rate.
4. Trough depth and frictional heating were found to increase with F10.7 within the post-midnight to morning (01:00–09:00 MLT) and dayside to duskside (12:00–16:00 MLT) regions during equinox, and the midnight to morning region (00:00–09:00 MLT) during summer. These data indicate that the trough becomes deeper via dissociative recombination caused by increased T_i with increasing F10.7, at least during the equinox and summer seasons (but not winter).

The mechanisms of trough formation, especially for those observed in the nightside ionosphere, require further investigation. A continuous examination of the physical and chemical processes of trough formation would strengthen our understating of its basic characteristics. Therefore, future studies should involve detailed analyses that consider the effects of a neutral atmosphere associated with frictional heating, particularly its effects on temperature, composition, and wind velocity. In addition, observations that allow for evaluation of the effects of advection on trough formation (e.g., high-temporal-resolution observations of the trough focusing on the duskside) are also required.

4 Blob deformation inside the ionospheric trough during a substorm

4.1 Introduction

Localized plasma density enhancements are often produced in the high-latitude ionosphere by the transportation process of plasma or particle precipitations. Among such plasma density enhancements, structures enhanced by a factor of 2–10 above the background density, and with horizontal dimensions ranging from ~100 to 1000 km, are generally called blobs from the outside of the polar cap, or patches in the polar cap [e.g., *Tsunoda*, 1988; *Crowley et al.*, 2000]. The blobs are generally categorized into the following three types: (1) boundary blobs, (2) subauroral blobs, and (3) auroral blobs. Boundary blobs are regarded as a proxy of the equatorward auroral boundary. Subauroral blobs resemble boundary blobs but are found in the trough region. In contrast, auroral blobs are observed in the auroral oval, and they appear to be localized in longitude when compared with boundary and subauroral blobs. Blobs/patches are important research subjects because they turn into ionospheric irregularities through some sort of deformation processes, and these irregularities affect radio wave propagation and scintillation of Global Navigation Satellite System (GNSS) signals [e.g., *Moen et al.*, 2013; *Jin et al.*, 2014]. Blobs/patches are known to be created by temporal/spatial changes in the convection pattern [e.g., *Livingstone et al.*, 1982; *Crowley et al.*, 2000; *Hosokawa et al.*, 2010a]. Such generation processes are well reproduced in past modeling works [e.g., *Robinson et al.*, 1985; *Anderson et al.*, 1996]. Besides, high-speed plasma flow can also deform them through the enhanced dissociative recombination process [*Valladares et al.*, 1994]. Thus, it is clear that background plasma convection plays an important role in blob deformation. However,

detailed blob behavior (deformation/splitting) under highly variable plasma convection during substorms is still unclear because of the lack of adequate observations. Therefore, new techniques that can follow variations of plasma parameters (e.g., density, velocity, and temperature) in detail are highly desirable.

In past studies, large-scale ionospheric density structures including blobs have been investigated by ground-based global positioning system (GPS) receivers to obtain TEC (total electron content) maps [e.g., *Coster et al.*, 2003; *Foster et al.*, 2005; *Hosokawa et al.*, 2010b; *Zhang et al.*, 2013]. The TEC maps can provide visualizations of the temporal evolution of the large-scale ionospheric density structure, but they cannot resolve the small-scale structure because of their limited spatial-temporal resolution (grid resolution of 1° for the latitude and 2° for the longitude, temporal resolution of 5 min). Furthermore, to study the blob deformation process in detail, we need to know not only the plasma structure but also the motion of the plasma convection with sufficient temporal resolution. Therefore, we conducted the European Incoherent Scatter (EISCAT) radar observations with high-speed meridional scans (grid resolution of ~0.1°–0.5° for the latitude, temporal resolution of 60–80 s) during October and December 2013. In this campaign, we encountered a convected blob inside the high-latitude trough in the dusk to pre-midnight region. The blob was deformed during a substorm. In this study, we examine the temporal evolution of the blob structure using the EISCAT data and other complementary data such as TEC maps and ground-based magnetometer data.

4.2 Observations

The high-speed meridional scans of the EISCAT UHF radar take 60–80 s to scan elevation angles from 25° to 89°. Detailed information about the EISCAT UHF radar

was introduced in Section 2.1. The observations were conducted as part of the Peer-reviewed Program (PP) and Japanese Special Program (SP) during October and December 2013, and we obtained a total of nine events that each lasted for a period of 4 hours (14:00–18:00 UT, $\mathrm{MLT} \simeq \mathrm{UT} + 2.2$ h). To date, the EISCAT observations for the blob have been conducted mainly by Common Program 3 (CP-3) scans, which take ~30 minutes for a single scan. However, as the temporal resolution of these single scans was insufficient to observe the rapid variation of the blob, we developed high-speed meridional scans for this study, with a temporal resolution that is ~25 times higher than that of the CP-3 scans. A detailed description of the CP-3 scans was introduced in Chapter 3. Since the EISCAT observations cannot capture the large-scale picture around the field of view (FOV) due to its limited observational range (up to ~5° of the latitude), we used TEC maps to visualize the horizontal shape of the density structures. In addition, the convection pattern around the EISCAT FOV was inferred from the ground-based magnetometer data.

During the observation campaign, we encountered a substorm on December 4, 2013 at 17:00–18:00 UT, which was detected using the geomagnetic data. Figure 4.1 shows the magnetometer data at the Dixon Island station (73.54°N, 80.56°E) and Tixie Bay station (71.58°N, 129.00°E). The beginning of the negative bay was shown at ~17:00 UT in the magnetometer H-component of Dixon Island and Tixie Bay located in the magnetic midnight sector, which means that the substorm growth phase started at this time. Subsequently, it explosively developed at ~17:30 UT; at the same time, Pi2 pulsation also appeared at the Nurmijärvi station (56.89°N, 102.18°E). Moreover, the auroral electrojet (AE) index suddenly increased at ~17:35 UT. Thus, we concluded that the onset time was around 17:30 UT. The interplanetary magnetic field (IMF) was predominantly southward (-4.4 to -3.4 nT) during 17:00–18:00 UT. In addition, the IMF B_y component turned from positive to negative (down to ~-2.0 nT) at ~17:40 UT.

4.3 Results

Figure 4.2 shows the TEC maps after onset of the substorm. The color scale runs from a high-electron density (red) to a low-electron density (blue). The top left panel of Figure 4.2 is an overview of the polar ionosphere around onset time (~17:30 UT). The dashed black line represents the solar terminator, where SZA = 90°. Besides, the top right panel is the TEC variation around the EISCAT FOV, which enlarges the black box shown in the top left panel. The black rectangle indicates the EISCAT FOV, and the dashed curving line indicates the boundary of the high-latitude trough. The earlier study used a threshold of just 20% lower than the background ionospheric electron density to identify the ionospheric trough [*Ishida et al.*, 2014a]. In this event, therefore, the region of less than ~4.8 TECU (total electron content unit; $1\,\mathrm{TECU} = 10^{16}\,\mathrm{el\,m^{-2}}$) can be considered as the trough region since the background ionospheric electron density was ~6.0 TECU in the nightside. Thus, we can see that the EISCAT FOV was inside of the trough region after onset of the substorm. Figure 4.2a–f shows a time sequence of the horizontal shape of the density structures around the EISCAT FOV. Note that the color scale ranges within 0.5–3.5 TECU so that the focus is on the density variation in the trough region. A sequence of structural change shown in Figure 4.2a–c illustrates that a chunk of increased plasma density gets closer to the EISCAT radar during 17:30–17:45 UT, and thus the TEC value slightly increases around the high-latitude side of the EISCAT FOV (up to ~3 TECU in Figure 4.2c). Then, the horizontal shape changes intricately around the EISCAT FOV during 17:45–18:00 UT (d–f). As described above, the TEC maps indicate that the EISCAT radar observed the plasma structuring in the dusk to pre-midnight subauroral region, and the structuring was shown in the trough region. Thus, the blob deformation, which is shown in detail latter, likely can be

regarded as that of a subauroral blob.

Figure 4.3 shows the keogram at an altitude of 210 km that was reproduced from the N_e observed by the meridional scans, with overplotted convection vectors. A keogram is the time versus geomagnetic latitude plot of the EISCAT plasma parameters along a specific cross section. In this study, we show a keogram along the geomagnetic north–south cross section. The convection vectors were from the International Monitor for Auroral Geomagnetic Effects (IMAGE) meridian chain. As explained in Section 2.3, the F-region drift vectors roughly go in the opposite direction from the E-region Hall current. Note that the convection vector was mapped to an altitude of 120 km along the geomagnetic field line and the vector size does not reflect the actual drift speed but the geomagnetic variation. The red dashed vertical line indicates the onset time of the substorm (~17:30 UT), and the remaining 30 minutes is divided into six sections according to Figures 4.2a–f. A high-density blob appears at ~17:20 UT, and then it extends toward the low-latitude region by the end of the observations (18:00 UT). The overplotted vectors shown in Figure 4.3 indicate that the southeastward flow was dominant above ~71.5°N, while the southwestward flow was dominant below ~68.5°N during 17:00–17:40 UT. Therefore, we can say that a southeast–southwest flow shear existed between 68.5°N–71.5°N at least by ~17:40 UT. Since the southeastward flow region expanded equatorward from ~17:20 UT to 18:00 UT, the latitude of the flow shear seems to move over time, and it appears to be located at a lower latitude than the blob region after ~17:50 UT. In addition, it should be noted that the southeastward flow increased rapidly at ~68°N after ~17:50 UT.

Figure 4.4 shows the temporal evolution of a blob on the meridional plane during Figure 4.2e–f: (top) N_e, (middle) north–south component of ion velocity ($V_{i\,(N-S)}$), and (bottom) T_i. Note that the $V_{i\,(N-S)}$ was calculated from the line-of-sight ion velocity ($V_{i\,(LOS)}$) and the elevation angle of the meridional scan. Dashed slant lines indicate the

geomagnetic field lines. Red horizontal axes indicate the geomagnetic latitudes at an altitude of 210 km. Hereafter, unless otherwise noted, the geomagnetic latitude is referred to that in Figure 4.4. Since the $V_{\mathrm{i\,(LOS)}}$ and T_{i} deduced from incoherent scatter fitting are usually inappropriate in the case of $N_{\mathrm{e}} < 5 \times 10^{10}\ \mathrm{m}^{-3}$, we ignored them in such situations. Figure 4.4a shows that a part of the blob appears at the high-latitude side of the EISCAT FOV, which was nearly superposed on the region of southward velocity. Figure 4.4b–c shows that the blob seems to be cracked around 68.5°N (red arrow in Fig. 3b) at ~17:52 UT, and then it is clearly divided into two parts (Blob A and Blob B) over the boundary where the $V_{\mathrm{i\,(N-S)}}$ reversed from northward to southward (hereafter referred to as the $V_{\mathrm{i\,(N-S)}}$ reversal boundary), whose northward component reaches to ~400–500 m/s. The scale sizes of the divided blobs were ~100 km in latitude (Blob A) and more than 250 km in latitude (Blob B). It can also be seen that the $V_{\mathrm{i\,(N-S)}}$ reversal boundary was roughly along the geomagnetic field line. Blob A is distributed at altitudes between 180 and 300 km, while blob B is distributed at even lower latitudes. Furthermore, the cross section between the two blobs is roughly along the geomagnetic field line. Figure 4.4d shows that the divided blobs appear to be elongated equatorward, and the velocity difference on the $V_{\mathrm{i\,(N-S)}}$ reversal boundary reached to ~800 m/s. Another feature identified in Figure 4.4 is that the T_{i} partially increased around the location where the blob started to be divided in Figure 4.4b, and the values reached up to ~1400 K. The video clip during 17:00–18:00 UT can be viewed at http://polaris.nipr.ac.jp/~ishida/PhD_thesis/movie.avi.

4.4 Discussion

In this section, we evaluate the physical and chemical processes associated with the blob deformation shown in Figure 4.4. Figure 4.5 shows the horizontal distribution of

the convection vector at ~17:55 UT (the time when the blob deformation was observed). The green, red, and black vectors are the convection vectors from the IMAGE magnetometer. The southeastward flow (green vectors) was located at the east side of the EISCAT radar, while the southwestward flow (red vectors) was located at the low-latitude side. From the above circumstances, we considered that southeastward–northwestward flow shear was located around the EISCAT observational region. As mentioned in Section 4.3, the $V_{\mathrm{i\,(N-S)}}$ was southward at the high-latitude side of the FOV, while it was northward at the low-latitude side of the FOV at ~17:55 UT. Thus, we assumed here that EISCAT observed the localized northwestward flow (a large red arrow in Figure 4.5) accompanied by southeastward–northwestward flow shear. It is known that the plasma flow shear is enhanced in the dusk to pre-midnight region during the substorm expansion phase [e.g., *Iijima and Nagata*, 1972]. Such plasma flow shear is considered to be formed by a combination of the DP 2 field (convection current system) and DP 1 field (substorm current system) [see *Iijima and Nagata*, 1972, Figure 9]. Moreover, the statistical analysis using SuperDARN data also indicated that the zonal convection speed is enhanced in the pre-midnight region during the substorm expansion phase in the case of IMF $B_{\mathrm{y}} < 0$ [see *Grocott et al.*, 2010, Figure 4d]. Hence, if EISCAT actually observed the enhanced plasma flow shear accompanied by the substorm expansion phase, the blob deformation might be caused by the enhanced flow shear through the K–H instability. Thus, we investigated the possibility that the blob deformation was caused by the enhanced flow shear through the K–H instability. Figure 4.6 presents how the blob was deformed by plasma flow shear through the K–H instability. Figure 4.6a describes a schematic illustration of a plausible geometry of the K–H instability on the geomagnetic latitude–longitude coordinates at ~17:55 UT. Assuming that the convected blob experienced strong southeastward–northwestward flow shear around 68.8°N, the blob could be deformed by plasma flow shear through

the K–H instability, as shown in Figure 4.6b. Note that the schematic illustration of the deformed blob is described as just an image without regard for the real scale ratio. In such a situation, it can be considered that the EISCAT radar observed the deformed blob caused by the K–H instability, which occurred in the localized region (see dashed rectangle in Figure 4.6a). Thus, the EISCAT radar supposedly observed the southward component and northward component of the plasma flow shear during this period, while the IMAGE meridional chain observed the geomagnetic variation derived from southeastward plasma flow. To evaluate the blob deformation in a quantitative way, we calculated the linear growth rate of the K–H instability on the basis of some assumptions. Early studies used $0.2\ V/L$ as the K–H growth rate, and thus the growth time τ_{KH} turns out to be $5\,L/V$, which is the inverse of the growth rate [*Carlson et al.*, 2007]. Here, V is the velocity difference and L is the scale length of the velocity difference. As shown in the line plot of Figure 4.5, the $V_{\mathrm{i\,(N-S)}}$ reverses sharply from ~450 m/s (northward) to ~-300 m/s (southward) between 68°N–69°N along the geomagnetic field line. Assuming that the velocity difference on the $V_{\mathrm{i\,(N-S)}}$ reversal boundary is derived from the zonal (southeastward–northwestward) flow shear, we can find that the scale length L is ~0.8° of the latitude (see dashed red rectangle in Figure 4.5), which corresponds to ~90 km at an altitude of 210 km. Considering that the blob starts to deform at ~17:52 UT, the K–H instability would have grown during ~3–4 minutes (~3.5 min on average) by the time of Figure 4.4c. Thus, we can find that the velocity difference of the convection shear $V_{\mathrm{i\,(shear)}}$ has to be larger than ~2100 m/s by the equation: $\tau_{KH} \leq 3.5\ \mathrm{min} \Rightarrow V \geq 5 \times 90\ \mathrm{km}/3.5\ \mathrm{min}$. Plasma flows of thousands of meters per second are often observed during substorms [e.g., *Zesta et al.*, 2011]. If such zonal (southeastward–northwestward) flow shear really existed, the angle θ between the shear plane and the meridional plane must be larger than ~70° by the equation: $V_{\mathrm{i\,(shear)}} = V_{\mathrm{i\,(N-S)}}/\cos(\theta) \geq 2100\ [\mathrm{m/s}]$, with $V_{\mathrm{i\,(N-S)}} \sim 750\ [m/s]$

around the shear region (see Figure 4.7). Besides, Figure 4.5 indicates that the angle θ is seemingly larger than ~70° around the EISCAT FOV; in addition, Figure 4.3 also shows the convection vector is inclined larger than ~70° from meridional plane after ~17:52 UT around 68°N, which also supports the above assumption. Hence, it is possible that the K–H instability could play a role in modulating the blob structure under the above assumption, although this is not a conclusive answer for the blob deformation.

Additionally, we should also consider that the blob deformation was possibly caused by just a simple plasma transportation process. *Hosokawa et al.* [2010a] reported that polar cap patch was divided into two smaller substructures around the plasma flow shear region. One interpretation is that the "seed" blob structure was distorted/stretched to two different directions on two streamlines and then divided into smaller substructures. Thus, if the $V_{\mathrm{i\,(shear)}}$ of ~1400 m/s holds true according to the reason explained above, the deformed blobs shown in Figure 4.4c might have been caused by the transportation process. Unfortunately, as the SuperDARN radar could not observe drift vectors around the EISCAT FOV on this event, we could not discuss this any further here.

Next, we discuss the extent to which chemical processes could have influenced the blob deformation. As mentioned in Section 4.3, it was found that the T_{i} partially increased around the location where the blob started to be divided in Figure 4.4b. In such a case, there is the possibility that frictional heating will cause blob cutting if the dissociative recombination promotes fast enough at the localized heated region. An early study indicated that the tongue of ionization (TOI) was divided into two patches by high-speed plasma jets in excess of 2 km through the enhanced recombination process [*Valladares et al.*, 1994]. Since we could identify that the blob deformed at ~150–300 km altitudes from Figure 4.4b–c, we compared the recombination rates by

altitude to evaluate whether or not dissociative recombination could have promoted this on a time scale of minutes. The recombination rate β used here was estimated from the mass spectrometer incoherent scatter (MSIS) model parameters and theoretical equations introduced by *St.-Maurice and Torr* [1978]. Note that for simplicity, we used a recombination rate of T_{i} = ~1400 K at all altitudes. Then, we can confirm that β is nearly equal to $\sim 310 \times 10^{-4}\,\mathrm{s}^{-1}$ at 150 km, $\sim 58 \times 10^{-4}\,\mathrm{s}^{-1}$ at 180 km, $\sim 16 \times 10^{-4}\,\mathrm{s}^{-1}$ at 210 km, and $\sim 5 \times 10^{-4}\,\mathrm{s}^{-1}$ at 240 km, which correspond to recombination times of ~0.5 min, ~3 min, ~10 min, and ~33 min, respectively. Considering that the blob starts to deform at ~17:52 UT, the dissociative recombination process would have been promoted for ~3–4 min by the time of Figure 4.4c. Hence, the results indicate that there would have been sufficient recombination time to allow for dissociative recombination and the blob cutting scenario at roughly less than 180 km of altitude, but it is difficult to explain that at higher altitudes. In addition, the observational results also show that the blob was not distributed at $\leq \sim 180$ km around the latitude of increased T_{i}. Thus, we suggest that dissociative recombination could have modulated the blob structure by reducing the electron density around the increased T_{i} region at roughly less than 180 km of altitude. One discrepancy is that electron density of blob B is higher than that of blob A even at $\leq \sim 180$ km nearby the increased T_{i} region. Figure 4.8 shows the temporal variation of the electron temperature (T_{e}) during ~17:52–17:59 UT. It seems likely that the T_{e} increases slightly from ~500 K to up to ~1000 K (red marked region) above ~68.5°N. Hence, the low-altitude ionization around blob B, and small increased T_{e} were possibly caused by high energy particle precipitation during the substorm. As mentioned above, the recombination time of the blob is a few minutes at $\leq \sim 180$ km, and thus the low-altitude ionization around blob B cannot be preserved throughout the long-distance transportation. In this respect, we can also consider that the transported blob possibly

originated from not only the TOI but also particle precipitation.

Here, we evaluate the linear growth rate of the G-D instability caused by the deformed blob shown in Figure 4.4c. The progression of the G-D instability requires the precondition that the gradient vector of the electron density ∇N_{e} is parallel to the $E_0 \times B$ drift vector. Hence, we focus here on the localized region where the ∇N_{e} of Blob B is superposed on the northward component of the $V_{\mathrm{i\,(N-S)}}$. Since above precondition is satisfied on the equatorward boundary of Blob B, the G-D instability was supposedly produced if the northward component of the $V_{\mathrm{i\,(N-S)}}$ worked effectively as the driver of the G-D instability. Figure 4.9 shows a schematic illustration of the G-D instability on the equatorward boundary of Blob B, which is described on the geomagnetic latitude–longitude coordinates. As mentioned above, we assume here that the G-D instability occurred after the blob deformation shown in Figure 4.4c, i.e., during 17:55–17:59 UT. In principle, the collisional and collisionless theories are applicable to the estimation of the linear growth rate of the G-D instability in the F-region altitude. It is known that the regions governed by collisional and collisionless plasma require the conditions of $\nu_{in} \gg 4\,V_0/L$ and $\nu_{in} \ll 4\,V_0/L$, respectively, where ν_{in} is the ion-neutral collision frequency, V_0 is the slip velocity, and L is the gradient scale length [e.g., *Ossakow et al.*, 1978; *Tsunoda*, 1988]. Here, assuming that the neutral wind is negligible as compared with the convection speed, the slip velocity V_0 can be given by ~400 m/s, the northward component of the $V_{\mathrm{i\,(N-S)}}$ shown in Figure 4.4c. In addition, the gradient scale length L of Blob B is estimated to be ~60 km at an altitude of 210 km. Thus, we can find that it is better to discuss our observational results in relation to the collisional case because $4\,V_0/L = \sim 2.6 \times 10^{-2}\ \mathrm{s}^{-1} \ll \nu_{in}$, where ν_{in} is $\sim 1.0\ \mathrm{s}^{-1}$ in the F-region altitude. The linear growth rate γ_0 is expressed as $\gamma_0 = V_0/L$ in a collisional plasma [e.g., *Tsunoda*, 1988; *Oksavik et al.*, 2012]. Hence, the γ_0 can be estimated to be $\sim 6.6 \times 10^{-3}\ \mathrm{s}^{-1}$, which corresponds to a growth time of ~2.5

min. This growth time is quantitatively consistent with results in past publications [e.g., *Oksavik et al.*, 2012; *Hosokawa et al.*, 2013]. However, the video clip shows that the northward component of the $V_{\mathrm{i\,(N-S)}}$ reduces from ~400 m/s to ~200 m/s during 17:55–17:59 UT (~4 min), and thus, the growth time is also supposed to increase from ~2.5 min to ~5 min, which is equal to a growth time of ~3.8 min on average. This means that the northward component of the $V_{\mathrm{i\,(N-S)}}$ (i.e., the driver of the G-D instability) continued longer than a duration of the growth time (~3.8 min), and thus, the GDI could supposedly arise on the equatorward boundary of Blob B. We do not have further observational evidence, but it is natural to assume that secondary irregularities were created through the G-D instability. A similar two-step irregularity generation process in the cusp region has been proposed in past publications [*Carlson et al.*, 2007; *Oksavik et al.*, 2012]: the initial "seed" density structures are created by the plasma flow shear or particle precipitation, and then the smaller scale irregularities are secondarily created by the G-D instability.

4.5 Conclusion

To the best of our knowledge, this is the first detailed report containing direct observations of blob deformation at the nightside auroral region during a substorm, and our report is accompanied by an evaluation of the plausible processes that could have contributed to blob deformation. During the substorm expansion phase, the blob seems to have divided into two parts, whose scale sizes were more than ~100 km of the latitude. We then discussed the possible physical and chemical processes that may have caused this blob deformation. Our analysis indicated that the K–H instability and dissociative recombination accompanied by the enhanced plasma flow could have influenced the blob structure. In addition, we discussed the G-D instability accompanied

by the deformed blob and then estimated its linear growth rate and growth time, which indicated that the growth time of the G-D instability is ~3.8 min on average. Thus, we suggest that once the blob structure breaks, secondary irregularities could be produced around the density boundary via the G-D instability process.

5 Summary of thesis

To date, trough studies have been based upon event studies and statistical analyses focusing solely on electron density, and thus, little is known about the predominant processes associated with trough formation on several time scales. Therefore, we have investigated the associated processes on several time scales, especially seasonal variation, solar activity dependence, and rapid temporal variation on a time scale of minutes. To understand these, we first conducted statistical analyses for the seasonal variation and solar activity dependence of the trough, which were based upon EISCAT UHF radar data collected during 1982–2011. Then, we ran high-speed meridional scans with the EISCAT UHF radar and for the first time observed blob deformation within the trough region during a substorm on December 4, 2013. These two investigations led us to the following conclusions.

Regarding the main results obtained for the seasonal variation of the trough:

1. During geomagnetic quiet to moderate conditions, frictional heating caused by plasma flow is active in the auroral region located in the high-latitude side of the EISCAT FOV, and thus, the occurrence rate of the trough is relatively higher in the auroral region. Especially, during summer, the ratio of frictional heating is ~47% higher on the high-latitude side. Based on comparisons of the occurrence rate with the ratio of frictional heating, we conclude that dissociative recombination accompanied by frictional heating is the main cause of trough formation in sunlit regions.

2. The increase in T_i is suppressed from winter to summer, most likely owing to frictional heating being suppressed by increased ion drag force on the neutral atmosphere in summer.

Regarding the main results concerning the dependence on solar activity:

3. In the winter, the occurrence rate of the trough decreases down to ~20% within the pre-midnight region, while it increases up to ~80% in the post-midnight region on the high-latitude side. In contrast, the occurrence rate increases up to ~80% within the pre-midnight region, while it decreases down to ~20% in the post-midnight region on the low-latitude side. These variations in the occurrence rate are supposedly influenced by the R2 current in the pre-midnight region and the R1 current in the post-midnight region, respectively. Similar behaviors were observed in the equinox under high solar activity. Accordingly, the effects of FACs become dominant with increasing F10.7 during the equinox.
4. Trough depth and frictional heating were found to increase with F10.7 within the post-midnight to morning and dayside to duskside regions during the equinox, and the midnight to morning regions during summer. These data indicate that the trough becomes deeper via dissociative recombination caused by increased T_i with increasing F10.7, at least during the equinox and summer seasons.

The new findings on rapid temporal variation within the trough region are summarized as follows:

5. This is the first time that direct observations of blob deformation during a substorm have been reported. The deformation process of the blob applied to the cusp region

was found within the trough region. Our analysis indicated that the K–H instability and dissociative recombination accompanied by the enhanced plasma flow could have influenced the blob structure, and then smaller scale irregularities could be secondarily created by the localized G-D instability.

Here, we propose two research topics for the future trough studies. The first important topic is the storm and substorm dependences of the trough. As the ionospheric condition is altered drastically by the development of storms and substorms, remarkable trough characteristics can be expected during these extreme conditions. For such studies, a superposed epoch analysis (SEA) using the EISCAT dataset would be effective. The SEA is a statistical method for the analysis of phenomena that develop according to a regular pattern; thus, it would be suitable for phenomena that have specific evolution phases like storms and substorms.

The second potential topic involves trough research using three-dimensional imaging radar. We introduced a new observational technique using EISCAT meridional scans in Chapter 3, but the results still have some drawbacks in regards to the spatial resolution. To understand the processes of small-scale structures like irregularities, a spatial resolution of tens of kilometers will be necessary. In addition to this, the present EISCAT observations cannot depict the phenomena three-dimensionally. In this sense, three-dimensional imaging observations with good spatial resolution will be necessary to understand the more detailed physical and chemical processes. Such instruments are now available in Poker Flat, Alaska (65°13'N, 147°47'W) and Resolute Bay, Canada (74°7'N, 265°1'E), which are called Advances Modular Incoherent Scatter Radar (AMISR). As the AMISR can grasp the volumetric images of the ionospheric plasma parameters on a more rapid time scale than that of the EISCAT meridional scans, it would be effective for further detailed investigations of the deformation processes of

blobs. Furthermore, the construction plan of the EISCAT_3D next-generation phased-array IS radar has been proceeding through the activities of member states of the EISCAT association [*Wannberg et al.*, 2010]. The EISCAT_3D radar is a three-dimensional imaging radar, which is supposed to have ten times higher temporal and spatial resolution than the present EISCAT UHF radar. Thus, new findings from such observations will likely be forthcoming.

6 Appendix

Here, we provide in-depth explanations associated with certain subjects presented in Chapter 2. First, we explain the principle behind IS radar observations in Section 6.1. Second, we explain how the plasma parameters are determined from the IS spectrum in Section 6.2. These two sections are based upon Chapter 2 and Appendix A in *Nygren* [1996]. Finally, we introduce the basic calculation of the TEC in Section 6.3.

6.1 Thomson scattering

Thomson scattering is a process by which the energy of an electromagnetic wave is partly scattered in various directions by a free electron. The IS radars observe the upper atmospheric plasma parameters by taking advantage of this mechanism. Once the electric field of the incident wave (e.g., ground-based-radar-derived radio wave) hits an electron, the electron begins to oscillate and then it emits a small fraction of the incident energy as dipole radiation (see Figure 6.1). However, as the incident energy emitted from an electron is too small to be detected on the ground, we need to send a radio wave of considerable power into the upper atmosphere to receive the radio wave from the electrons. Ions will also try to oscillate as well, but they do not emit sufficient incident energy because of their greater mass. Thus, we can consider that the received radio wave is derived solely from the electrons. The total power scattered by a single electron is

$$\begin{aligned} P_{\mathrm{T}} &= \int S_{\mathrm{s}} |\mathbf{R}|^2 d\Omega = 2\pi \int_0^{\pi} S_{\mathrm{S}} |\mathbf{R}|^2 \sin\chi \, d\chi \\ &= 2\pi r_0^2 S_{\mathrm{i}} \int_0^{\pi} \sin^3 \chi d\chi = \frac{8}{3}\pi r_0^2 S_{\mathrm{i}} = \sigma_{\mathrm{T}} S_{\mathrm{i}} \end{aligned} \tag{6.1}$$

where S_s is the intensity of the scattered radiation at $\mathbf{R}$, r_0 is the classical electron radius ($= 2.82 \times 10^{-15}$ m), and χ is the angle between the electric field of the incident wave and the scattering direction (see Figure 6.2). In the above equation, σ_T is the total cross section of Thomson scattering, also known as the electron Thomson cross section.

In the macroscopic sense, there are always thermal fluctuations in plasma. In the electron component of the plasma, fluctuations with wavelengths longer than the Debye length

$$\lambda_D = \sqrt{\frac{\epsilon_0 k_B T_e}{n_e e^2}} \approx 6.87 \times 10^{-3} \text{ m} \tag{6.2}$$

are controlled mainly by the motion of the massive ions because the light electrons must follow the ions in order to preserve charge neutrality. Therefore, although the mechanism of microscopic scattering is Thomson scattering by the electrons, the shape of the IS spectrum at wavelengths longer than the Debye length will be determined by the motion of the ions. As the transmitting frequency of the EISCAT UHF radar is ~931.5 MHz, its wavelength is $\sim 0.32 \text{ m} \ll 6.87 \times 10^{-3}$ m (Debye length). Thus, we can establish that the IS spectrum of the EISCAT UHF radar incorporates information regarding the electrons and the ions.

Because of the propagation of plasma waves, Doppler shifts appear in the IS spectrum. Figure 6.3 shows a schematic description of the propagation of a plasma wave. A radio wave is transmitted at frequency ν_0 in the direction of $\boldsymbol{r}_T$ and scattering from the direction of $\boldsymbol{r}_R$ is observed at a remote site. Scattering is due to density fluctuations with a wavelength $\lambda = \lambda_0/(2\cos\phi)$ and with their wave vectors pointing in the direction of the bisector of the angle between $\boldsymbol{r}_T$ and $\boldsymbol{r}_R$. Two waves propagating in opposite directions satisfy these conditions, but in Figure 6.3, only the wave fronts

approaching the radars are shown. The phase velocity of the wave fronts is $\pm\mathrm{v}$, where the upper and lower signs refer to the approaching and escaping waves, respectively. Then, the component of the phase velocity in the direction of the transmitter beam is $\pm\mathrm{v}\cos\phi$. The beam-aligned velocity component of the electrons traveling with the wave front is the same, and therefore, the electrons observe the transmitted wave at frequency

$$\nu' = \nu_0\sqrt{\frac{c \pm \mathrm{v}\cos\phi}{c \mp \mathrm{v}\cos\phi}} \tag{6.3}$$

In their own frame of reference, the electrons emit radiation at the same frequency. As the component of their velocity in the direction of the receiver beam is also $\pm\mathrm{v}\cos\phi$, the frequency observed at the receiver is

$$\nu'' = \nu'\sqrt{\frac{c \pm \mathrm{v}\cos\phi}{c \mp \mathrm{v}\cos\phi}} = \nu_0\frac{c \pm \mathrm{v}\cos\phi}{c \mp \mathrm{v}\cos\phi} \approx \nu_0\left(1 \pm 2\frac{\mathrm{v}\cos\phi}{c}\right) \tag{6.4}$$

Then, the observed Doppler shift is given by

$$\delta\nu = \nu'' - \nu_0 = \pm 2\nu_0\frac{\mathrm{v}\cos\phi}{c} = \pm 2\frac{\mathrm{v}\cos\phi}{\lambda_0} \tag{6.5}$$

where λ_0 is the radar wavelength at frequency ν_0. As $\lambda_0 = 2\lambda\cos\phi$, we can also write

$$\delta\nu = \pm 2\frac{\mathrm{v}\cos\phi}{2\lambda\cos\phi} = \pm\frac{\mathrm{v}}{\lambda} = \pm\nu \tag{6.6}$$

This means that the scattered signal should consist of spectral lines shifted upward and

downward from the transmitter frequency. The frequency shift is given by the frequency of the plasma fluctuation at wavelength $\lambda = \lambda_0/(2\cos\phi)$.

The result is valid separately for ion acoustic waves and Langmuir waves. Thus, the scattering spectrum should contain four lines: two caused by ion acoustic waves and two by Langmuir waves. These are called ion lines and plasma lines, respectively, and they are shown schematically in Figure 6.4.

As the phase velocity of the ion acoustic wave is independent of wavelength, it is convenient to use Equation 6.5 in calculating the Doppler shift of the ion lines, which gives

$$\delta\nu_{\mathrm{i}} = \pm\nu_{+} = \pm 2\frac{\mathrm{v}_{+}\cos\phi}{\lambda_0} \tag{6.7}$$

indicating that the frequency shift depends on angle ϕ. The maximum Doppler shift $2\,\mathrm{v}_{+}/\lambda_0$ is observed in the backscattering. When the radar wavelength is 0.3–1.5 m and the phase velocity is a few hundreds of meters per second, the Doppler shift is of the order of a few kilohertz or even less.

6.2 Incoherent scatter fitting

The IS spectrum described in Figure 6.4 is an oversimplification that neglects the fact that the two lines due to ion acoustic waves are actually broadened to merge into a single ion line. If the ion lines were composed of sharp peaks, like those shown in Figure 6.4, the scattering signal should be composed of sinusoidal functions and each should be due to a sinusoidal ion acoustic wave. However, all the time ion acoustic waves are thermally generated as well as attenuated in the plasma. Even in the absence of ion-neutral collisions, the waves are damped by a wave–particle interaction known as

Landau damping. Therefore, the amplitude and phase of a given Fourier component, at a sufficiently distant time in the past, have no relation whatsoever to the present amplitude and phase. In terms of the autocorrelation function, this means that the autocorrelation function of the scattered signal is attenuated with increasing delay. Thus, the autocorrelation function is no longer sinusoidal and the corresponding spectrum can no longer be a delta function, i.e., it must be broader. Figure 6.5 shows an example of the IS spectrum calculated at $\nu_0 = 931.5\ \mathrm{MHz}$ (transmitting frequency of the EISCAT UHF radar), assuming an ion mass of 30.5 u (mixture of O_2^+ and NO^+ ions), zero ion-neutral collision frequency, and a temperature of 300 K. The two ion lines are broadened around $\nu_0 \pm \nu_+$, and their sum makes a double-humped shape characteristic of the E- and F-region altitudes.

The shape of the ion line in the IS spectrum is determined by various plasma parameters. The full theory gives an expression of the line shape that is used in determining the values of the plasma parameters by the least squares method. Figure 6.6 shows how the IS spectrum depends on the plasma parameters. In principle, the spectrum shape depends on the ion temperature, temperature ratio, collision frequency, and concentration ratio of ions with different masses. Moreover, electron density is determined by using the power scale of the spectral density and the line-of-sight ion velocity is determined from this Doppler shift. In addition, a set of secondary parameters can also be calculated, which include the electric field, conductivity tensor, electric currents, and neutral wind velocity.

6.3 Calculation of the TEC

Here, we present a brief introduction to the TEC calculation. As described in Section 2.2, the TEC value represents the total number of electrons along the GPS signal path,

the units of which are expressed as $\mathrm{el/m^2}$ or TECU ($= 10^{16}\mathrm{el/m^2}$). Thus, the TEC value is expressed by

$$\mathrm{TEC} = \int_s n_e ds \tag{6.8}$$

where s means the signal path. As the GPS signal refracts depending on the transmitting frequency and electron density along the signal path, the refraction rate can be expressed as follows:

$$n = 1 - \frac{a n_\mathrm{e}}{{\nu_0}^2} \tag{6.9}$$

where ν_0 is the transmitting frequency and a is a constant ($4.03 \times 10^{17}\ \mathrm{ms^{-2}TECU^{-1}}$). In addition, the GPS signal is also delayed during ionospheric propagation, and thus, the delay time Δt can be determined by

$$\Delta t = \int_s (n-1) ds \tag{6.10}$$

By inserting Equation 6.9 in Equation 6.10, we obtain the following equation:

$$\Delta t = -\frac{a}{f^2} TEC \tag{6.11}$$

Here, given that the ideal arrival time to the receiver without delay is t and that the arrival times of the L1-band (f_1) and L2-band (f_2) are t_1 and t_2, respectively, the delay times derived from the L1- and L2-bands are respectively given by

$$\Delta t_1 = t_1 - t = -\frac{a}{f_1^2}\mathrm{TEC} \tag{6.12}$$

$$\Delta t_2 = t_2 - t = -\frac{a}{f_2^2}\mathrm{TEC} \tag{6.13}$$

From Equation 6.12 and Equation 6.13, the TEC value is given as follows:

$$\mathrm{TEC} = \frac{t_1 - t_2}{a}\frac{f_1^2 f_2^2}{f_1^2 - f_2^2} \tag{6.14}$$

7 References

Albritton, D. L., I. Dotan, W. Lindinger, M. McFarland, J. Tellinghuiser, and F. C. Fehsenfeld (1977), Effects of ion speed distributions in flow drift tube studies on ion-neutral reactions, *J. Chem. Phys.*, 66, 410.

Anderson, D. N., D. T. Decker, and C. E. Valladares (1996), Modeling boundary blobs using time varying convection, *Geophys. Res. Lett.*, 23, 579–582, doi:10.1029/96GL00371.

Aruliah, A. L., A. D. Farmer, D. Rees, and U. Brandstrom (1996), The seasonal behavior of high-latitude thermospheric winds and ion velocities observed over one solar cycle, *J. Geophys. Res.*, 101, 15,701–15,711.

Basu, Su., S. Basu, J. J. Makela, E. MacKenzie, P. Doherty, J. W. Wright, F. Rich, M. J. Keskinen, R. E. Sheehan, and A. J. Coster (2008), Large magnetic storm-induced nighttime ionospheric flows at midlatitudes and their impacts on GPS-based navigation systems, *J. Geophys. Res.*, 113, A00A06, doi:10.1029/2008JA013076. [Printed 114(A3), 2009.]

Brekke, A. (2013), *Physics of the Upper Polar Atmosphere*, 2nd Ed., Springer.

Carlson, H. C., T. Pedersen, S. Basu, M. Keskinen, and J. Moen (2007), Case for a new process, not mechanism, for cusp irregularity production, *J. Geophys. Res.*, 112, A11304, doi:10.1029/2007JA012384.

Collis, P. N., and I. Häggström (1988), Plasma convection and auroral precipitation processes associated with the main ionospheric trough at high latitudes, *J. Atmos. Terr. Phys.*, 50(4–5), 389–404, doi:10.1016/0021-9169(88)90024-4.

Coster, A., F. C. Foster, and P. Erickson (2003), Monitoring the ionosphere with GPS: Space weather, *GPS World*, 14(5), 42–49.

Crowley, G., A. J. Ridley, D. Deist, S. Wing, D. J. Knipp, B. A. Emery, J. Foster, R.

Heelis, M. Hairston, and B. W. Reinisch (2000), The transformation of high-latitude ionospheric F-region patches into blobs during the March 21, 1990 storm, *J. Geophys. Res*., 105, 5215–5230.

Davies, J. A., M. Lester, and I. W. McCrea (1997), A statistical study of ion frictional heating observed by EISCAT, *Ann. Geophys.*, 15, 1399–1411.

Doe, R. F., J. F. Vickrey, and M. Mendillo (1995), Electrodynamic model for the formation of auroral ionospheric cavities, *J. Geophys. Res.*, 100, 9683–9696.

Foster, J. C., and H. B. Vo (2002), Average characteristics and activity dependence of the subauroral polarization stream. *J. Geophys. Res*., 107 (A12), 1475.

Foster, J. C., A. J. Coster, P. J. Erickson, J. M. Holt, F. D. Lind, W. Rideout, M. McCready, A. van Eyken, R. A. Greenwald, and F. J. Rich (2005), Multiradar observations of the polar tongue of ionization, *J. Geophys. Res*., 110, A09S31, doi:10.1029/2004JA010928.

Fukushima, N. (1976), Generalized theorem for no ground magnetic effect of vertical currents connected with Pedersen currents in the uniform-conductivity ionosphere, *Rep. Ionos. Space Res. Jap*., 30, 35–40.

Grocott, A., S. E. Milan, T. K. Yeoman, N. Sato, A. S. Yukimatu, and J. A. Wild (2010), Superposed epoch analysis of the ionospheric convection evolution during substorms: IMF B_Y dependence, *J. Geophys. Res*., 115, A00I06, doi:10.1029/2010JA015728.

Häggström, I., and P. N. Collis (1990), Ion composition changes during F-region density depletions in the presence of electric fields at auroral latitudes, *J. Atmos. Terr. Phys.*, 52, 519–529.

Horvath, I., and E. A. Essex (2003), The southern-hemisphere mid-latitude day-time and night-time trough at low sunspot numbers, *J. Atmos. Solar-Terr. Phys.*, 65, 917–940, doi:10.1016/S1364-6826(03)00113-5.

Hosokawa, K. (2008), *MTI-HandBook*, (http://www2.nict.go.jp/aeri/swe/MTI/MTI_symposium/mti-handbook/top/h20/MTI_Handbook_Hosokawa_Ver_1_1.pdf).

Hosokawa, K., J. P. St.-Maurice, G. J. Sofko, K. Shiokawa, Y. Otsuka, and T. Ogawa (2010a), Reorganization of polar cap patches through shears in the background plasma convection, *J. Geophys. Res*., 115, A01303, doi:10.1029/2009JA014599.

Hosokawa, K., T. Tsugawa, K. Shiokawa, Y. Otsuka, N. Nishitani, T. Ogawa, and M. R. Hairston (2010b), Dynamic temporal evolution of polar cap tongue of ionization during magnetic storm, *J. Geophys. Res*., 115, A12333, doi:10.1029/2010JA015848.

Hosokawa, K., S. Taguchi, Y. Ogawa, and J. Sakai (2013), Two-dimensional direct imaging of structuring of polar cap patches, *J. Geophys. Res*., 118, 6536–6543, doi:10.1002/jgra.50577.

Iijima, T., and T. Nagata (1972), Signatures for the substorm development of the growth phase and expansion phase, *Planet. Space Sci.*, 20, 1095–1101.

Ijima, T., and T. A. Potemra (1976), The amplitude distribution of field-aligned currents at northern high latitudes observed by TRIAD, *J. Geophys. Res.*, 81, 2165–2174.

Jin Y., J. I. Moen, and W. J. Miloch (2014), GPS scintillation effects associated with polar cap patches and substorm auroral activity: direct comparison, J. Space Weather Space Clim., 4(A23), doi:10.1051/swsc/2014019.

Keskinen, M. J., and S. L. Ossakow (1983), Theories of high-latitude ionospheric irregularities: A review, *Radio Sci*., 18(6), 1077–1091, doi:10.1029/RS018i006p01077.

Keskinen, M. J., H. G. Mitchell, J. A. Fedder, P. Satyanarayana, S. T. Zalesak, and J. D. Huba (1988), Nonlinear evolution of the Kelvin-Helmholtz instability in the high-latitude ionosphere, *J. Geophys. Res*., 93(A1), 137–152, doi:10.1029/JA093iA01p00137.

Kivelson, M. G., and C. T. Russell (1995), *Introduction to Space Physics*, Cambridge Univ. Press.

Lee, I., J. Y. Liu, W. Wang, C. Chen, and C. Lin (2011), The ionospheric mid-latitude trough observed by FORMOSAT−3/COSMIC during solar minimum, *J. Geophys. Res.*, 116, A06311, doi:10.1029/2010JA015544.

Livingston, R. C., C. L. Rino, J. Owen, and R. T. Tsunoda (1982), The anisotropy of high-latitude nighttime F region irregularities, *J. Geophys. Res.*, 87, 10,519–10,526, doi:10.1029/JA087iA12p10519.

Ma, S. Y., P. Liu, and K. Schlegel (2000), EISCAT observation of a high-latitude ionization trough associated with a reversed westward plasma flow, *Geophys. Res. Lett.*, 27(20), 3269–3272, doi:10.1029/2000GL000073.

Mallis, M., and E. A. Essex (1993), Diurnal and seasonal variability of the southern-hemisphere main ionospheric trough from differential-phase measurements, *J. Atmos. Terr. Phys.*, 55(7), 1021–1037, doi:10.1016/ 0021-9169(93)90095-G.

McCrea, I. W., M. Lester, T. R. Robinson, N. M. Wade, and T. B. Jones (1991), On the identification and occurrence of ion frictional heating events in the high-latitude ionosphere, *J. Atmos. Terr. Phys.*, 53(6/7), 587–597.

McFarland, M., D. L. Albritton, F. C. Fehsenfeld, E. E. Ferguson, and A. L. Schmeltekopf (1973), Flow-drift technique for ion mobility and ion-molecule reaction rate constant measurements, 2, Positive ion reactions of N^+, O^+, and N_2^+.with O_2. and O^+ with N_2. from thermal to ~2 eV, *J. Chem. Phys.*, 59, 6620–6628.

Moen, J., K. Oksavik, L. Alfonsi, Y. Daabakk, V. Romano, and L. Spogli (2013), Space weather challenges of the polar cap ionosphere, J. Space Weather Space Clim., 3(A02), doi:10.1051/swsc/2013025.

Moffett, R. J., and S. Quegan (1983), The midlatitude trough in the electron concentration of the ionospheric F-layer: A review of observations and modeling, *J. Atmos. Terr. Phys.*, 45, 315–343, doi:10.1016/S0021-9169(83)80038-5.

Nilsson, H., T. I. Sergienko, Y. Ebihara, and M. Yamauchi (2005), Quiet-time mid-latitude trough: influence of convection, field-aligned currents and proton precipitation, *Ann. Geophys.*, 23, 3277–3288.

Nygren, T. (1996), *Introduction to incoherent scatter measurements*, Invers Publications, Sodankyla, Finland.

Ohtani, S., S. Wing, V. G. Merkin, and T. Higuchi (2014), Solar cycle dependence of nightside field-aligned currents: Effects of dayside ionospheric conductivity on the solar wind-magnetosphere-ionosphere coupling, *J. Geophys. Res.*, 119, 322–334, doi:10.1002/2013JA019410.

Oksavik, K., J. Moen, M. Lester, T. A. Bekkeng, and J. K. Bekkeng (2012), In situ measurements of plasma irregularity growth in the cusp ionosphere, *J. Geophys. Res*., 117, A11301, doi:10.1029/2012JA017835.

Ossakow, S. L., P. K. Chaturvedi, and J. B. Workman (1978), High-altitude limit of the gradient drift instability, *J. Geophys. Res.,* 83(A6), 2691–2693, doi:10.1029/JA083iA06p02691.

Pilipp, W. G., and G. Morfill (1978), The formation of the plasma sheet resulting from plasma mantle dynamics, *J. Geophys. Res.*, 83, 5670.

Richmond, A. (1987), The ionosphere. Chapter 7 in: S.-I. Akasofu and Y. Kamide (Eds.), *The Solar Wind and the Earth*, Terra Sci. Publ. Co., Tokyo, Japan, pp. 123–140.

Robinson, R. M., R. T. Tsunoda, J. F. Vickrey, and L. Guerin (1985), Sources of *F* region ionization enhancements in the nighttime auroral zone, *J. Geophys. Res*., 90, 7533–7546.

Roble, R. G. (1987), The Earth's Thermosphere. Chapter 12 in: S.-I. Akasofu, and Y.

Kamide (Eds.), *The Solar Wind and the Earth*, Terra Sci. Publ. Co., Tokyo, Japan, pp. 243–264.

Rodger, A., R. Moffett, and S. Quegan (1992), The role of ion drift in the formation of ionisation troughs in the mid-and high-latitude ionosphere: A review, *J. Atmos. Terr. Phys.*, 54(1), 1–30, doi:10.1016/0021-9169(92) 90082-V.

Schunk, R., and A. Nagy (2009), *Ionospheres, Second edition*, Cambridge Univ. Press.

Sojka, J. J., R. W. Schunk, J. V. Evans, J. M. Holt, and R. H. Wand (1983), Comparison of model high-latitude electron densities with millstone hill observations, *J. Geophys. Res.*, 88, 7783–7793.

Spiro, R. W., R. A. Heelis, and W. B. Hanson (1978), Ion convection and the formation of the mid-latitude F region ionization trough, *J. Geophys. Res.*, 83(A9), 4255–4264, doi:10.1029/JA083iA09p04255.

St.-Maurice, J.-P., and D. Torr (1978), Nonthermal rate coefficients in the ionosphere: The reactions of O^+ with N_2, O_2, and NO, *J. Geophys. Res*., 83(A3), 969–977.

Stocker, A. J., and E. M. Warrington (2011), The effect of solar activity on the Doppler and multipath spread of HF signals received over paths oriented along the midlatitude trough, *Radio Sci.*, 46, RS1014, doi:10.1029/2010RS004482.

Tsunoda, R. T. (1988), High-latitude F region irregularities: A review and synthesis, *Rev. Geophys*., 26, 719–760.

U.S. Standard Atmosphere (1976), NOAA, NASA, USAF, Washington, D.C.

Valladares, C. E., S. Basu, J. Buchau, and E. Friis-Christensen (1994), Experimental evidence for the formation and entry of patches into the polar cap, *Radio Sci*., 29, 167–194.

Van Zandt, T. E. and Knecht, R. W. (1964), The structure and physics of the upper atmosphere. In: D. P. Le Galley and A. Rosen (Eds.), *Space Physics*, John Wiley & Sons, New York.

Vo, H. B., and J. C. Foster (2001), A quantitative study of ionospheric density gradients at midlatitudes, *J. Geophys. Res.*, 106, 21,555–21,563.

Voiculescu, M., I. Virtanen, and T. Nygrén (2006), The F region trough: seasonal morphology and relation to interplanetary magnetic field. *Ann. Geophys.*, 24, 173–185.

Voiculescu, M., T. Nygrén, A. Aikio, and R. Kuula (2010), An olden but golden EISCAT observation of a quiet-timeionospheric trough, *J. Geophys. Res.*, 115, A10315, doi:10.1029/2010JA015557.

Wannberg U. G., *et al.* (2010), EISCAT_3D: A next-generation European radar system for upper atmosphere and geospace research, Radio Science Bulletin No. 332.

Whalen, J. A. (1989), The daytime F layer trough and its relation to ionospheric-magnetospheric convection, *J. Geophys. Res.*, 94(A12), 17169–17184.

Williams, P. J. S., and A. R. Jain (1986), Observations of the high-latitude trough using EISCAT, *J. Atmos. Terr. Phys*., 48, 423–434.

Winser, K. J., G. O. L. Jones, and P. J. S. Williams (1986), A quantitative study of the high latitude ionospheric trough using EISCAT's common programmes, *J. Atmos. Terr. Phys*., 48(9–10), 893–904.

Zesta, E., *et al.* (2011), Ionospheric convection signatures of tail fast flows during substorms and Poleward Boundary Intensifications (PBI), *Geophys. Res. Lett*., 38, L08105, doi:10.1029/2011GL046758.

Zhang, Q., B. Zhang, M. Lockwood, H. Hu, J. Moen, J. M. Ruohoniemi, E. G. Thomas, S. Zhang, H. Yang, R. Liu, K. A. McWilliams, and J. B. H. Baker (2013), Direct observations of the evolution of polar cap ionization patches, *Science*, 339, 1597–1600, doi:10.1126/science.1231487.

Zou, S., M. B. Moldwin, J. M. Nicolls, A. J. Ridley, A. J. Coster, E. Yizengaw, L. R. Lyons, and E. F. Donovan (2013), Electrodynamics of the high-latitude trough: Its

relationship with convection flows and field-aligned currents, *J. Geophys. Res.*, 118(1–8), 2565–2572, doi:10.1002/jgra.50120.

This thesis is based on the following papers:

Ishida, T., Y. Ogawa, A. Kadokura, Y. Hiraki, and I. Häggström (2014a), Seasonal variation and solar activity dependence of the quiet-time ionospheric trough, *J. Geophys. Res*., 119, 6774–6783, doi:10.1002/2014JA019996.

Ishida, T., Y. Ogawa, A. Kadokura, K. Hosokawa, and Y. Otsuka (2014b), Direct observations of blob deformation during a substorm, *submitted to Ann. Geophys.*

8 Tables

Table 3.1

Details of the dataset used in this study obtained by the European Incoherent Scatter (EISCAT) UHF radar, Common Program 3 (CP-3). The number and pulse code for each CP-3 operation is different for every observational term.

Number	**Start date**	**End date**	**Number of available events**	**Pulse code**	**Number of beams**
1	19820512	19821215	13	cp3c	16
2	19830629	19861027	76	cp3c	15
3	19860401	19880309	51	cp3e	16
4	19880425	19980430	105	cp3f	16
5	20011121	20031126	30	tau3	16
6	20030624	20091215	65	tau1	16
7	20111128	20111207	5	bella	15

9 Figures

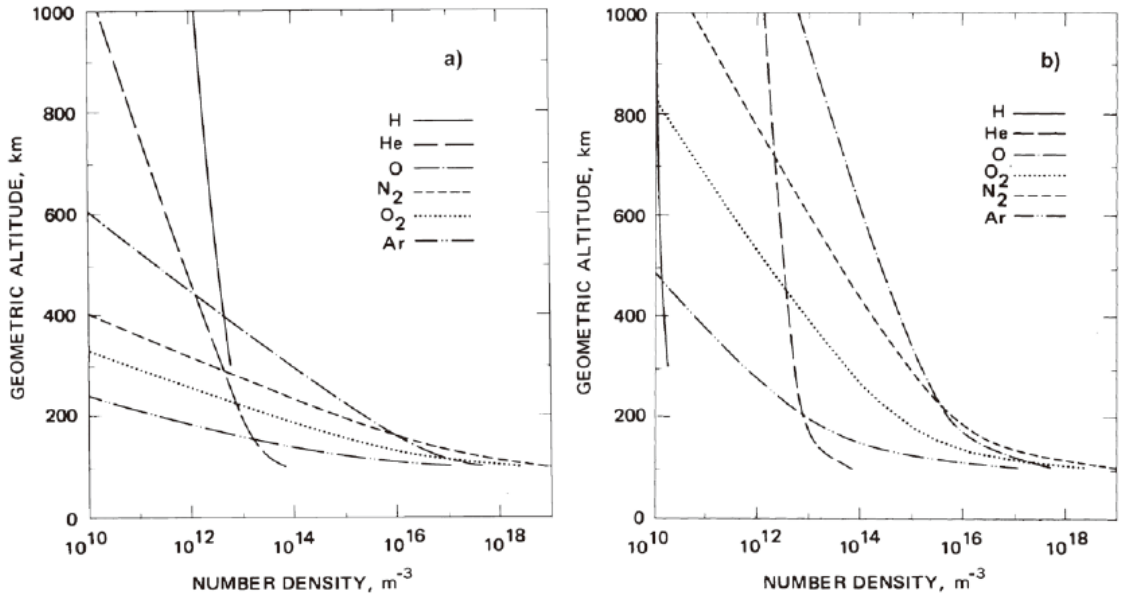

Figure 1.1. Composition changes in the atmosphere with respect to conditions of: (a) the solar minimum and (b) the solar maximum; data show the dominance of heavier constituents at greater altitudes during the solar maximum [from *U.S. Standard Atmosphere*, 1976]

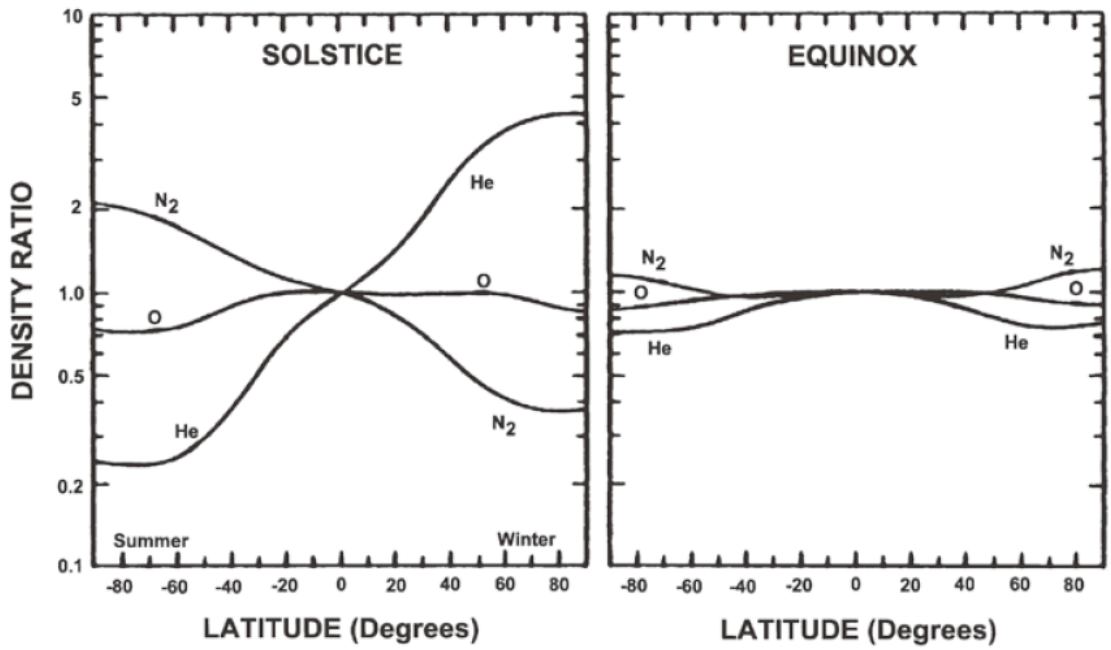

Figure 1.2. The latitudinal distribution of molecular nitrogen (N_2), atomic oxygen (O), and helium (He) under solstice and equinox conditions [from *Roble*, 1987]

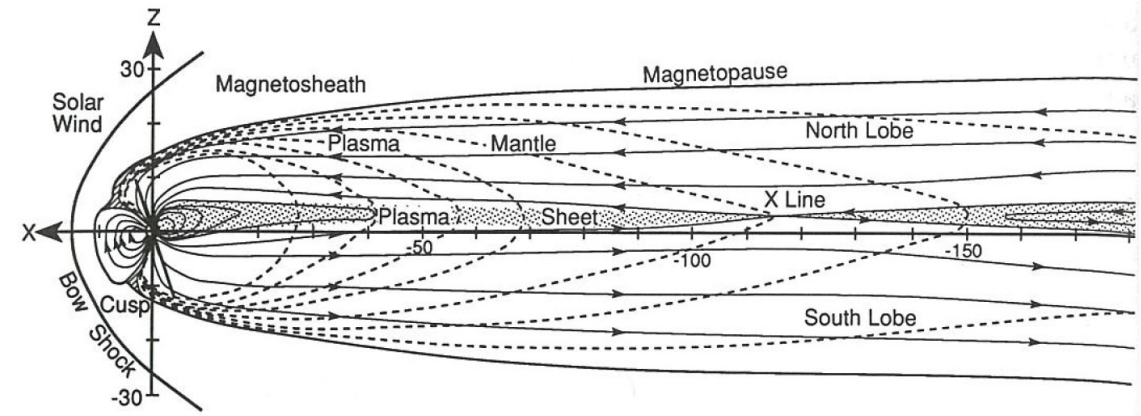

Figure 1.3. Noon–midnight cross section of the magnetosphere and geomagnetic tail drawn to scale. The plasma sheet carrying the cross-tail current sheet separates into two tail lobes. A magnetic x-line or neutral point is shown 115 Re behind the Earth. The dashed lines show the trajectories followed by particles in the plasma mantle [after *Pilipp and Morfill*, 1987; from *Kivelson and Russell*, 1995]

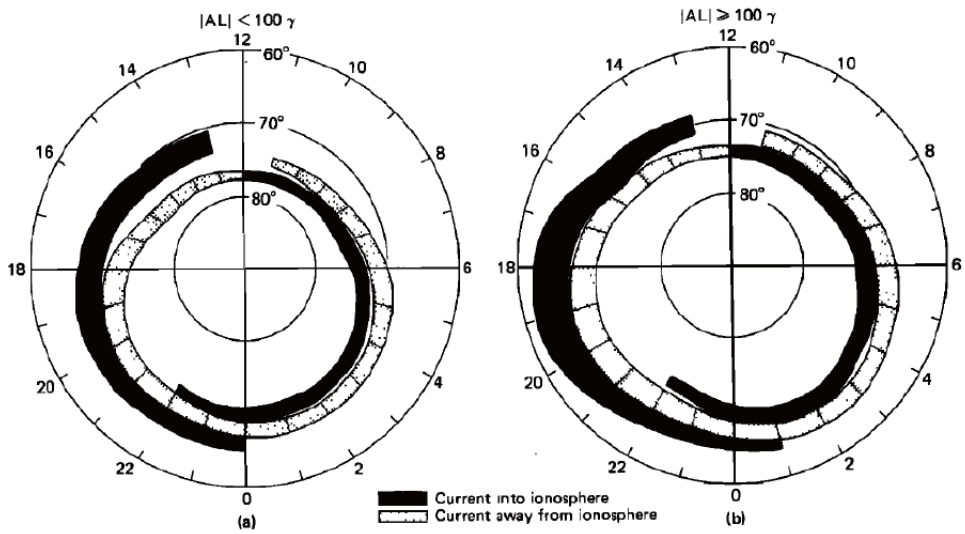

Figure 1.4. Average patterns of field-aligned currents in the high-latitude region during (a) moderate conditions and (b) disturbed conditions. The currents into and out of the ionosphere are indicated by different symbols that show currents out of the ionosphere in the dusk sector and into the ionosphere in the dawn sector, which are associated with Region-1 currents. The equatorial currents that enter the ionosphere in the dusk sector and leave the ionosphere in the dawn sector are associated with Region-2 currents [from *Iijima and Potemra*, 1976]

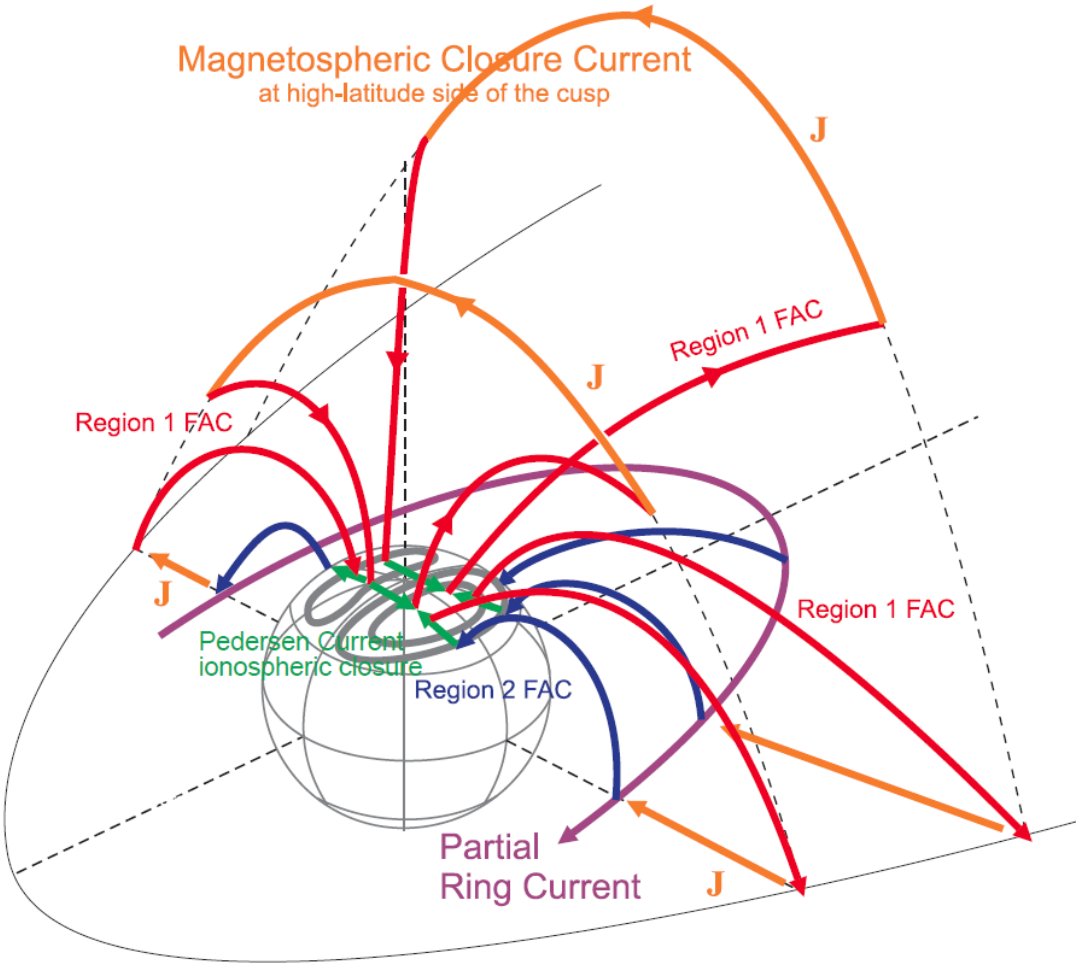

Figure 1.5. Magnetosphere–ionosphere current closure. Green, red, and blue lines are the Pedersen current, Region-1 current, and Region-2 current in the ionosphere, respectively. Orange and purple lines are the magnetospheric current and partial ring current in the magnetosphere, respectively [after *Hosokawa*, 2008]

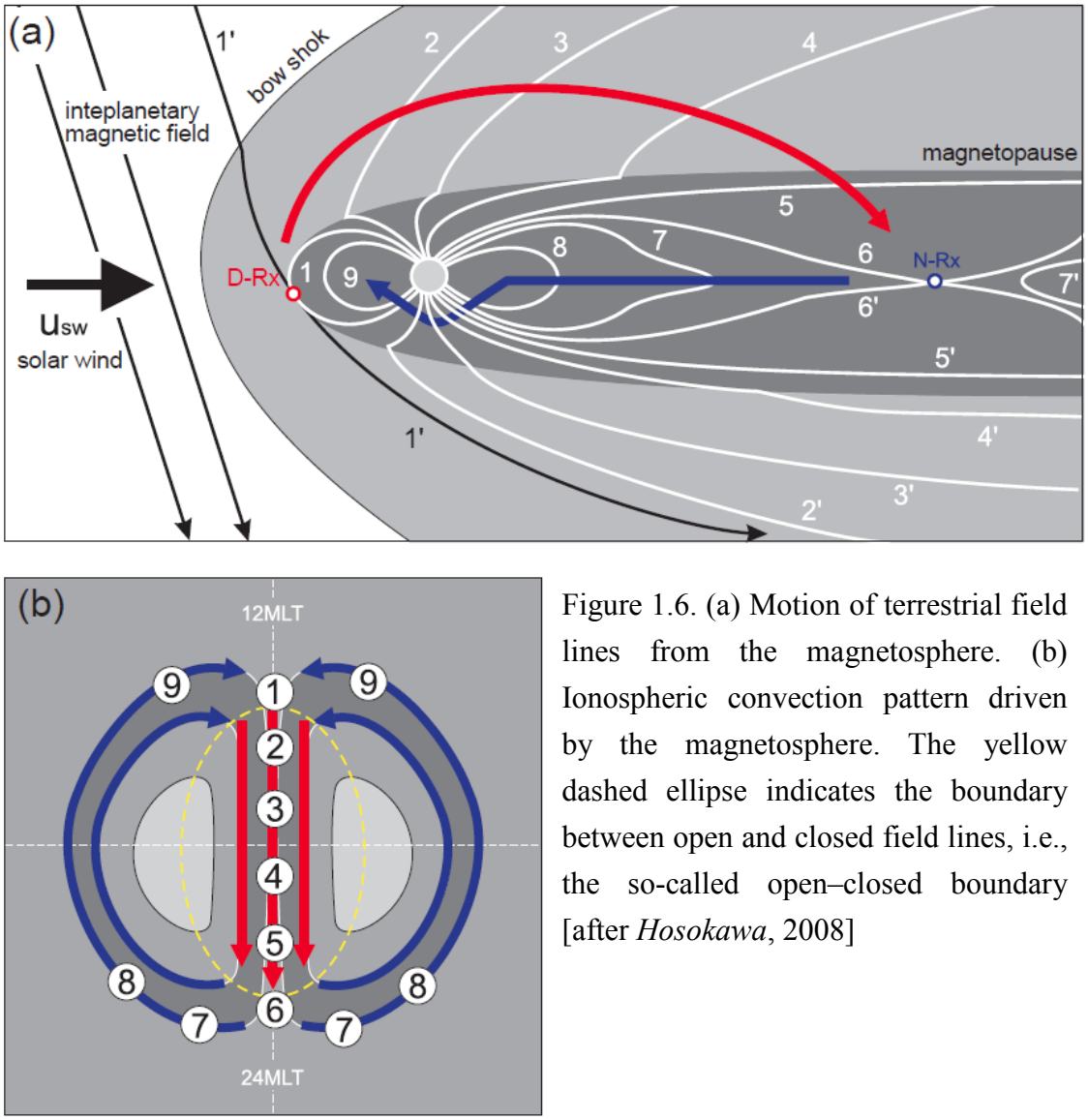

Figure 1.6. (a) Motion of terrestrial field lines from the magnetosphere. (b) Ionospheric convection pattern driven by the magnetosphere. The yellow dashed ellipse indicates the boundary between open and closed field lines, i.e., the so-called open–closed boundary [after *Hosokawa*, 2008]

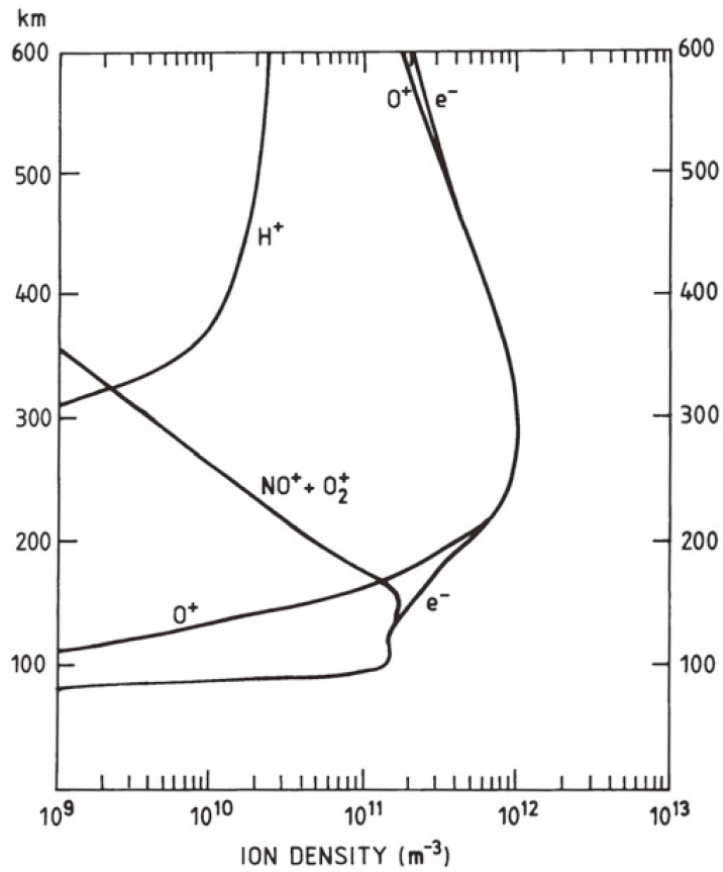

Figure 1.7. Altitude profiles of the most typical ion species in the ionosphere between 100 and 600 km, together with the corresponding electron density profile [after *Richmond*, 1987; from *Brekke*, 2013]

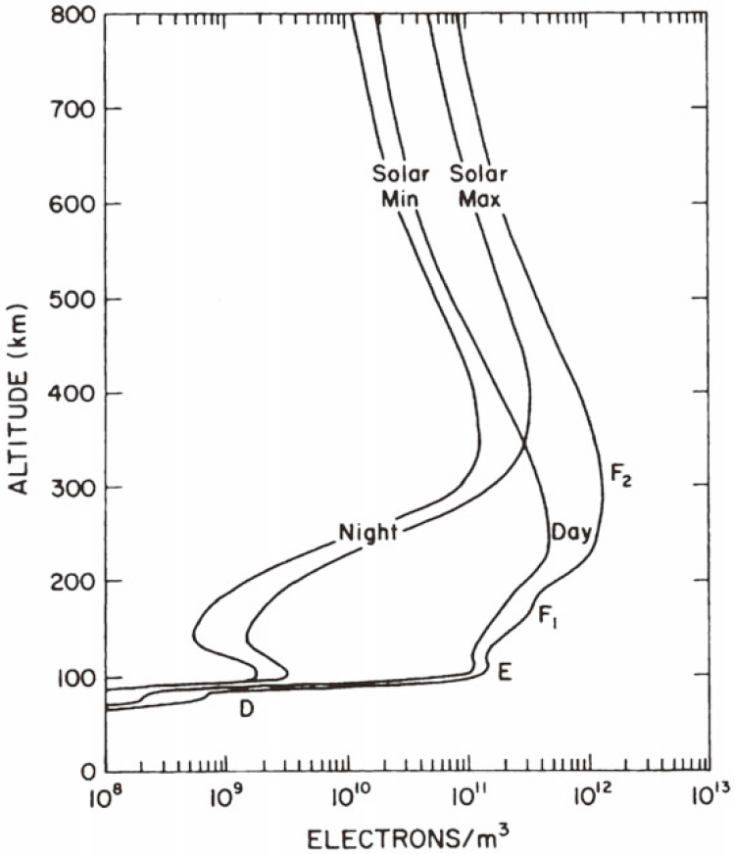

Figure 1.8. Typical mid-latitude ionospheric electron density profiles for sunspot maximum and minimum conditions at daytime and nighttime. The different altitude regions in the ionosphere are labeled with the appropriate nomenclature [from *Richmond*, 1987]

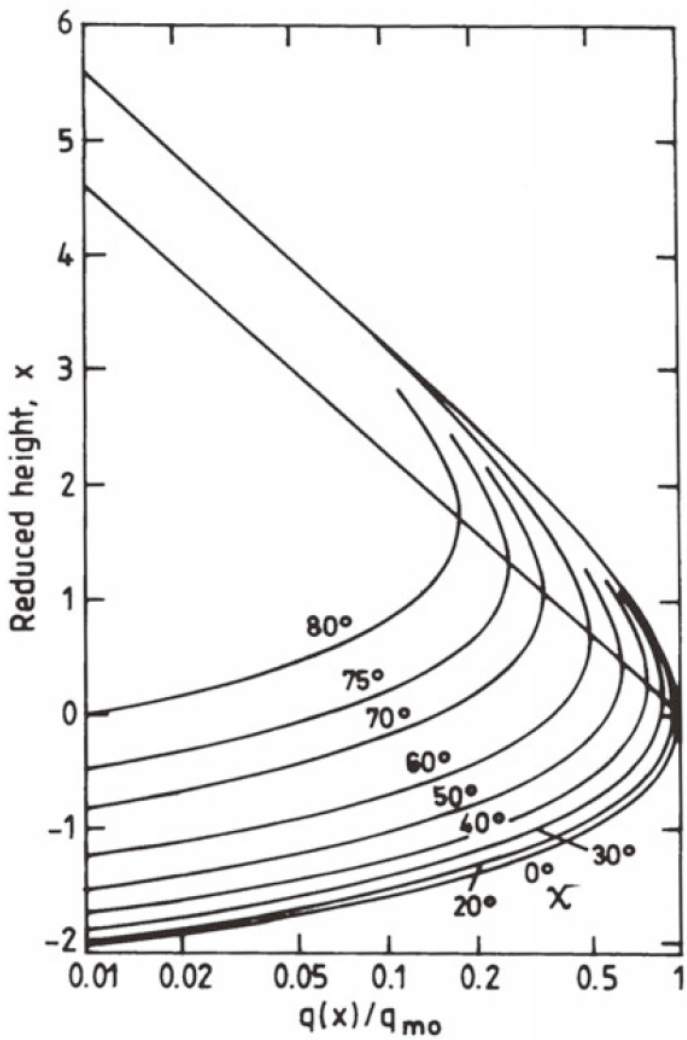

Figure 1.9. Chapman production profiles for different solar zenith angles [after *Van Zandt and Knecht*, 1964; from *Brekke*, 2013]

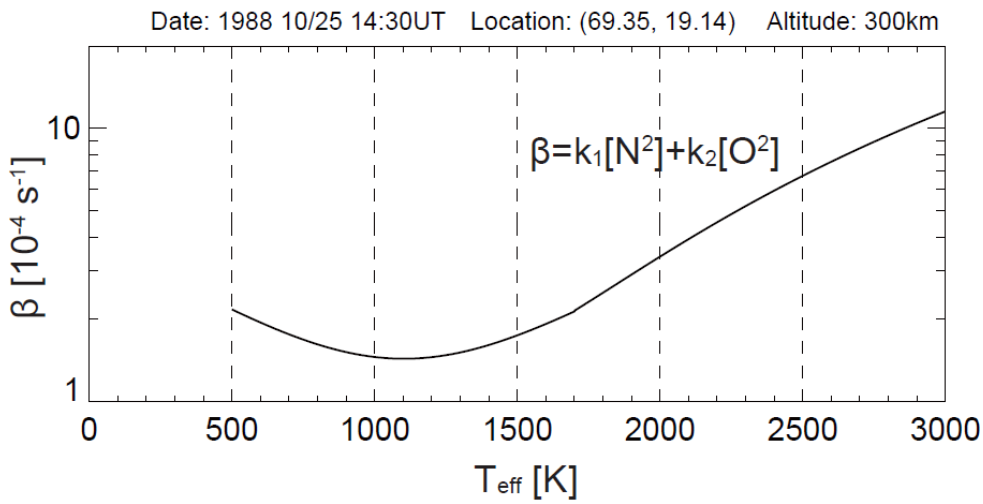

Figure 1.10. Profile of the dissociative recombination rate at an altitude of 300 km against temperature during an equinox day

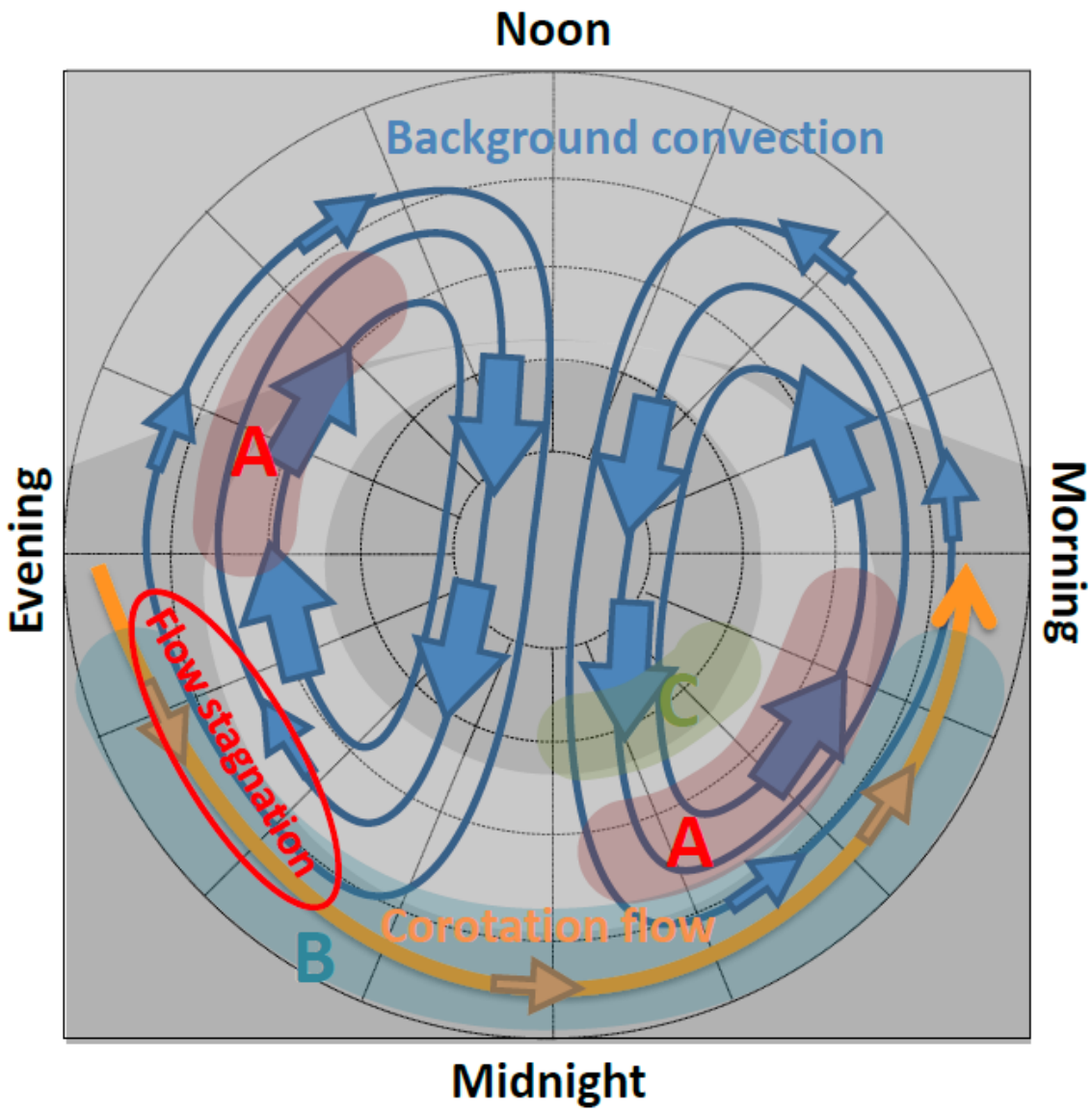

Figure 1.11. Location of the ionospheric troughs during the quiet time. Region A (red), B (light blue), and C (green) indicate the high-latitude troughs, mid-latitude trough, and so-called polar hole, respectively. Note that the polar hole is out of our research target. Additionally, the background plasma convection and the Earth's corotation plasma flow are described as blue and orange vectors, respectively [after *Rodger et al.*, 1992]

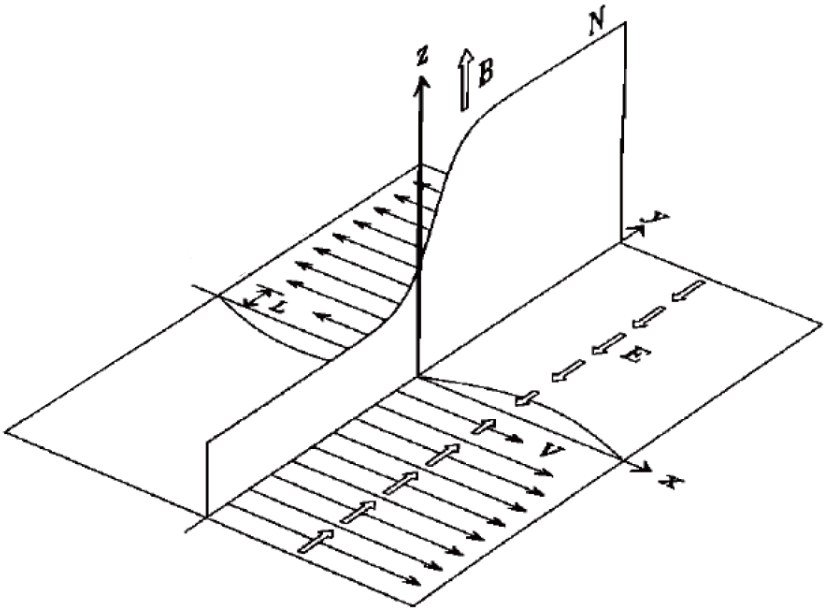

Figure 1.12. Simplified configuration of the Kelvin–Helmholtz instability, where V is the plasma flow, E is the electric field, L is the width of the shear region, and B is the geomagnetic field line [after *Keskinen et al.*, 1988]

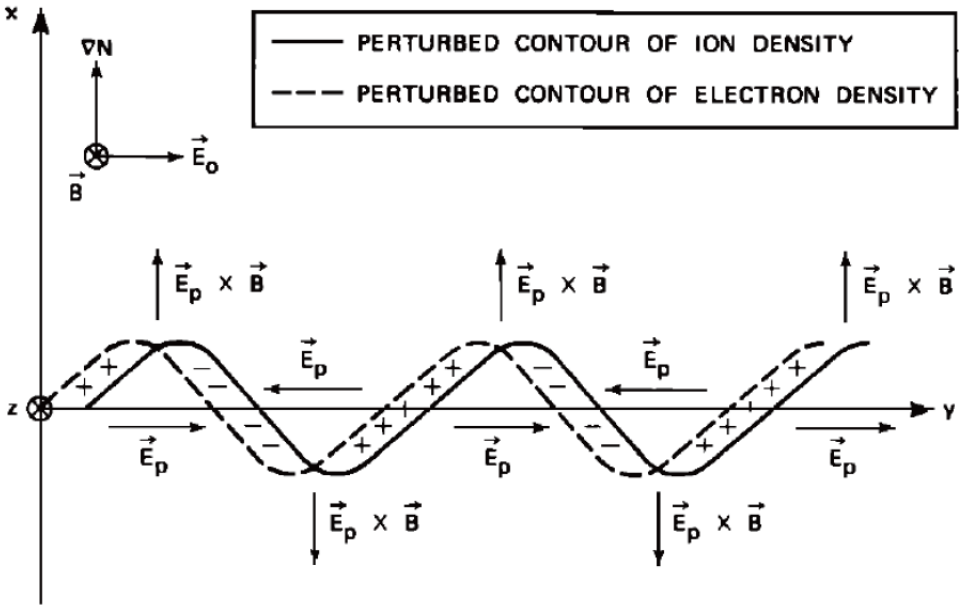

Figure 1.13. Simplified schematic diagram showing the basic mechanics of the gradient drift instability. A Pedersen ion drift (to the right) leads to charge separation and the development of polarization electric fields $\overrightarrow{E_p}$. The sense of $\overrightarrow{E_p}$ is to drive $\overrightarrow{E_p} \times B$ motion that further enhances the original plasma perturbation [from *Tsunoda*, 1988]

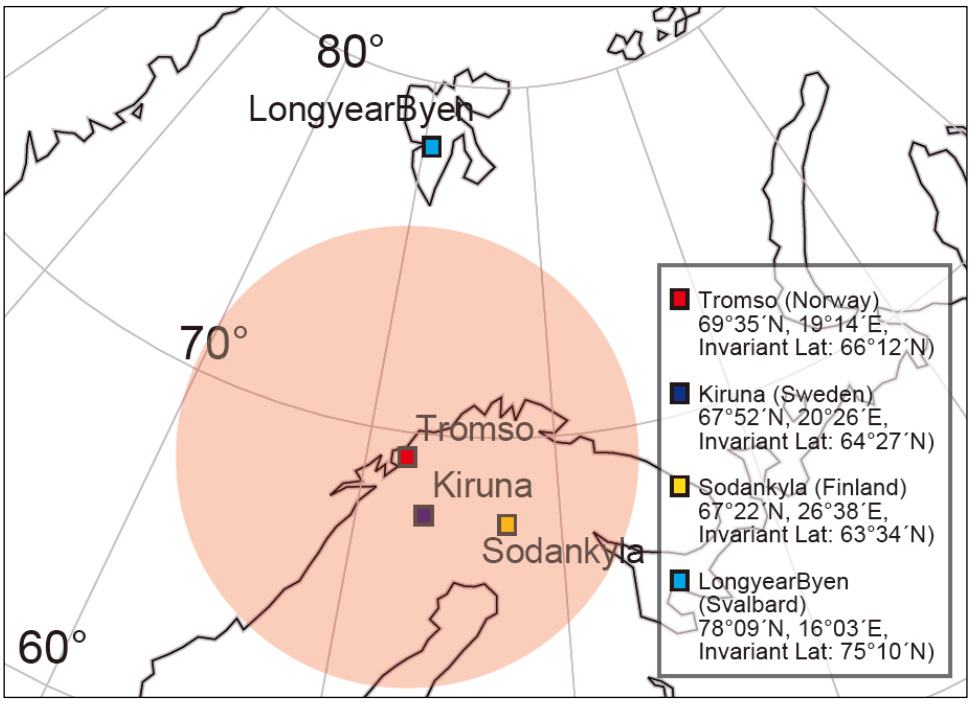

Figure 2.1. Locations of the EISCAT radars. Red, blue, yellow, and light blue squares indicate the Tromsø, Kiruna, Sodankyla, and LongyearByen sites, respectively. The red circle is the EISCAT Tromsø radar's observable region

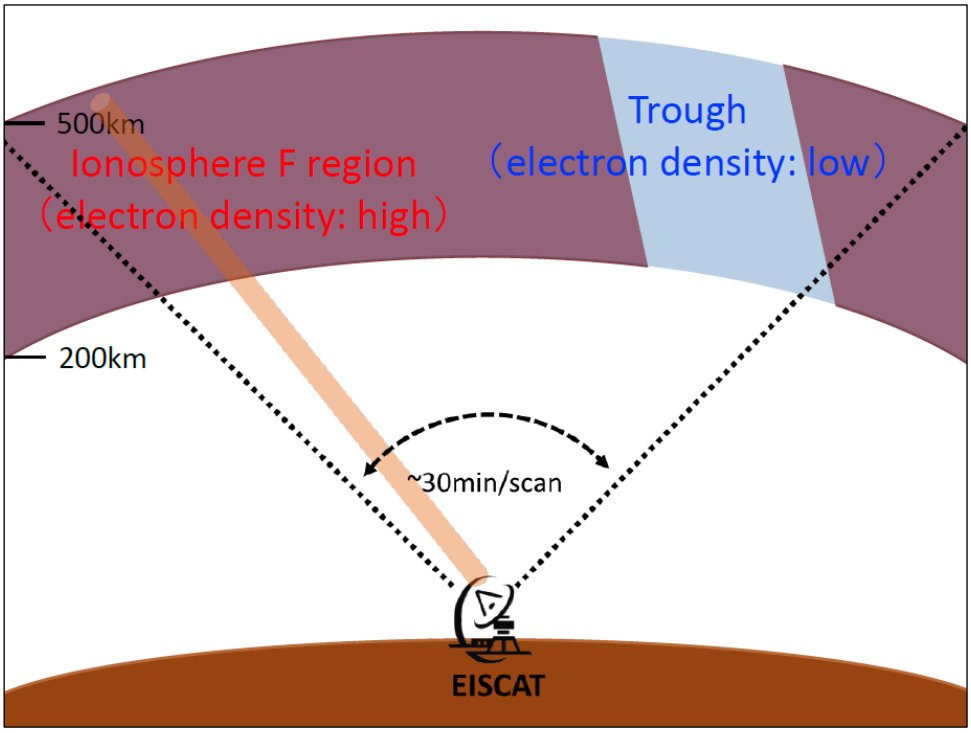

Figure 2.2. Schematic description of the EISCAT CP-3 scan observation. The CP-3 scan takes ~30 min for one single scan, and it obtains a latitudinal distribution covering of ~12.5° at an altitude of 325 km

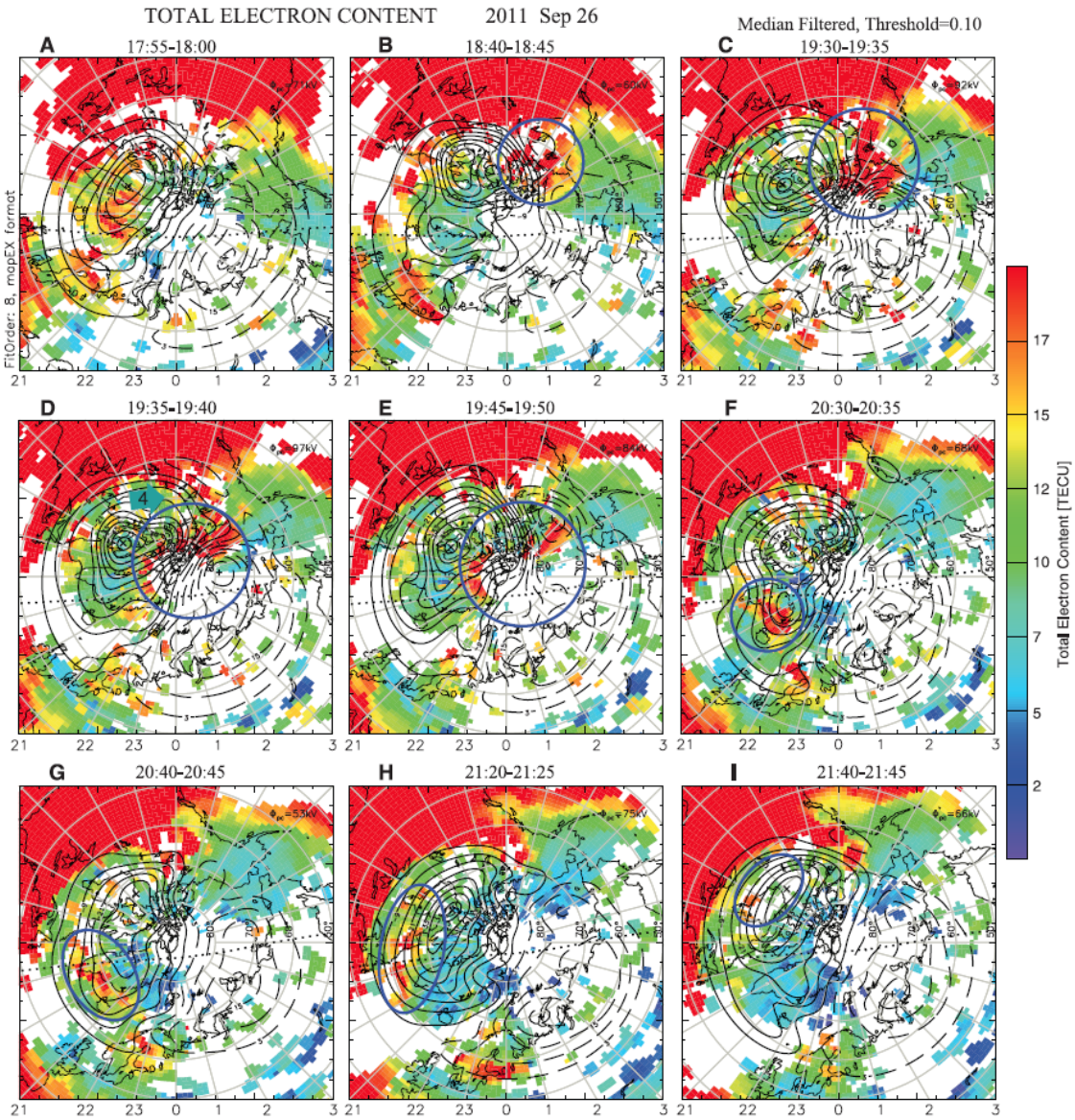

Figure 2.3. (A to I) Direct observations of the polar cap patch by the TEC maps with ionospheric convection on a geomagnetic latitude-magnetic local time grid with noon at the top. The dotted line across each panel is the day–night terminator at 100-km altitude. The blue circles and ellipses highlight the polar cap patch, the evolution of which is followed in this figure [from *Zhang et al.*, 2013]

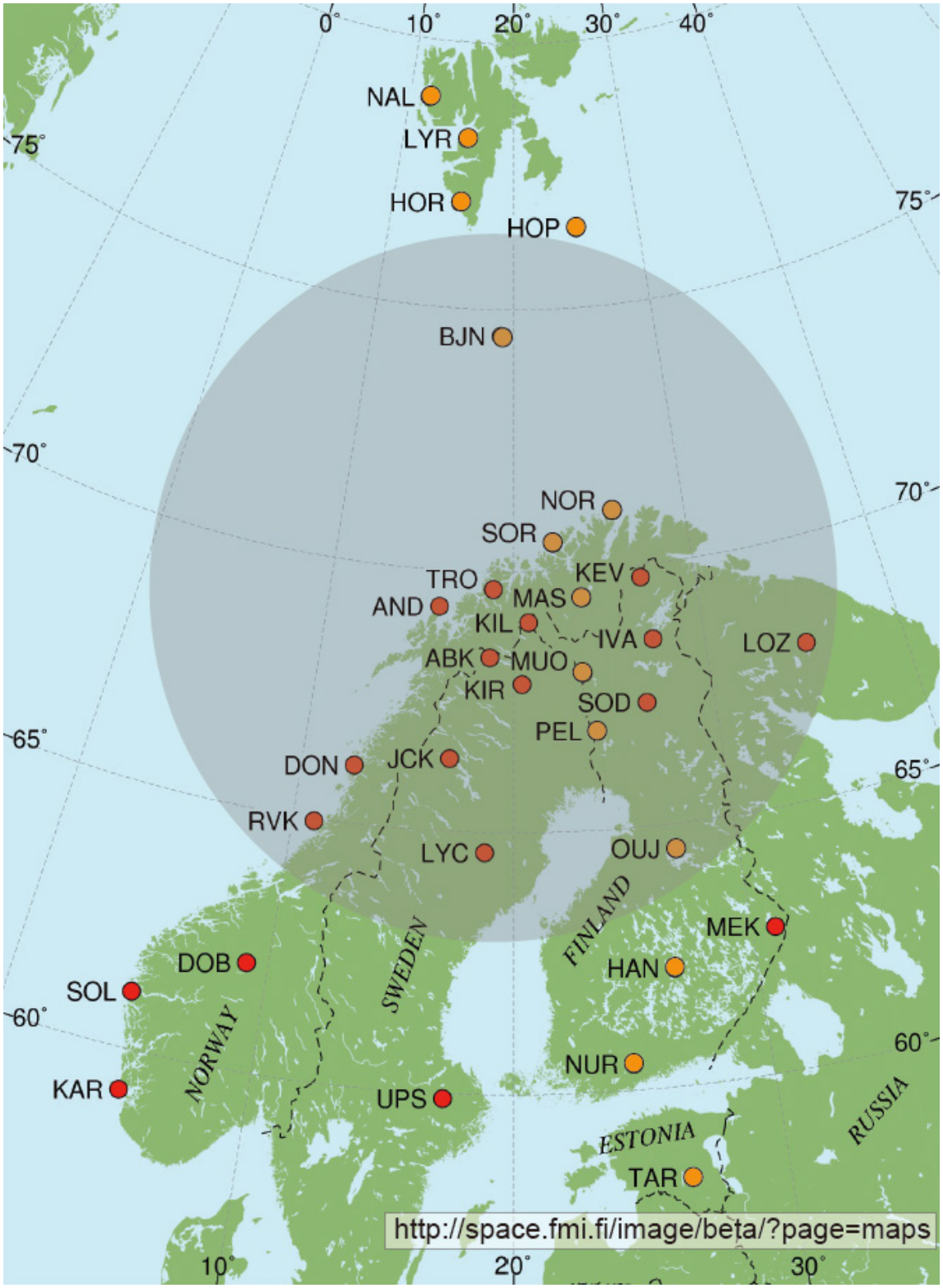

Figure 2.4. Locations of the IMAGE magnetometer stations (orange: 14, red: 18). Orange circles indicate stations used for this research. Shaded area indicates the EISCAT Tromsø radar's observable region

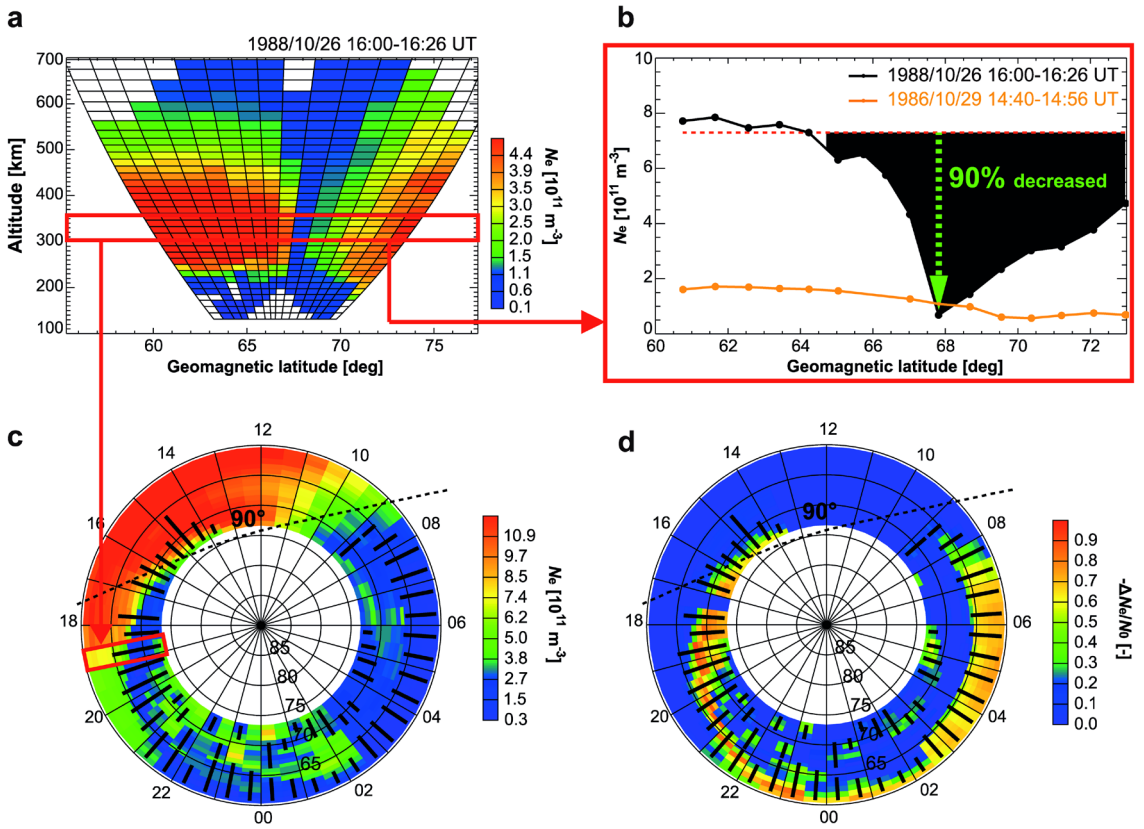

Figure 3.1. Electron density observed with the EISCAT CP-3 scan. (a) A single CP-3 scan, shown in the geomagnetic meridional plane, with geomagnetic latitude on the horizontal axis and altitude on the vertical axis. The color scale runs from high electron density (red) to low electron density (blue). (b) Latitudinal distribution of electron density with black and orange solid lines representing electron density variations during the trough (October 26, 1988, 16:00–16:26 UT) and non-trough (October 29, 1986, 14:40–14:56 UT) events, respectively. Black shaded region denotes the trough as detected by the algorithm described in the main text, and the red dashed line represents the background electron density. (c) Polar plot of the electron-density distribution in MLT–MLat coordinates for the same day. Color coding is same as in Figure 3.1a. Dashed black lines represent the solar terminator, where the SZA = 90°, and solid black lines indicate the latitudinal widths of the detected troughs. (d) Polar plot of the ratio of electron density in the trough region with color coding representing the rate of decrease. Dashed black lines and solid black lines are the same as in Figure 3.1c [from *Ishida et al.*, 2014a]

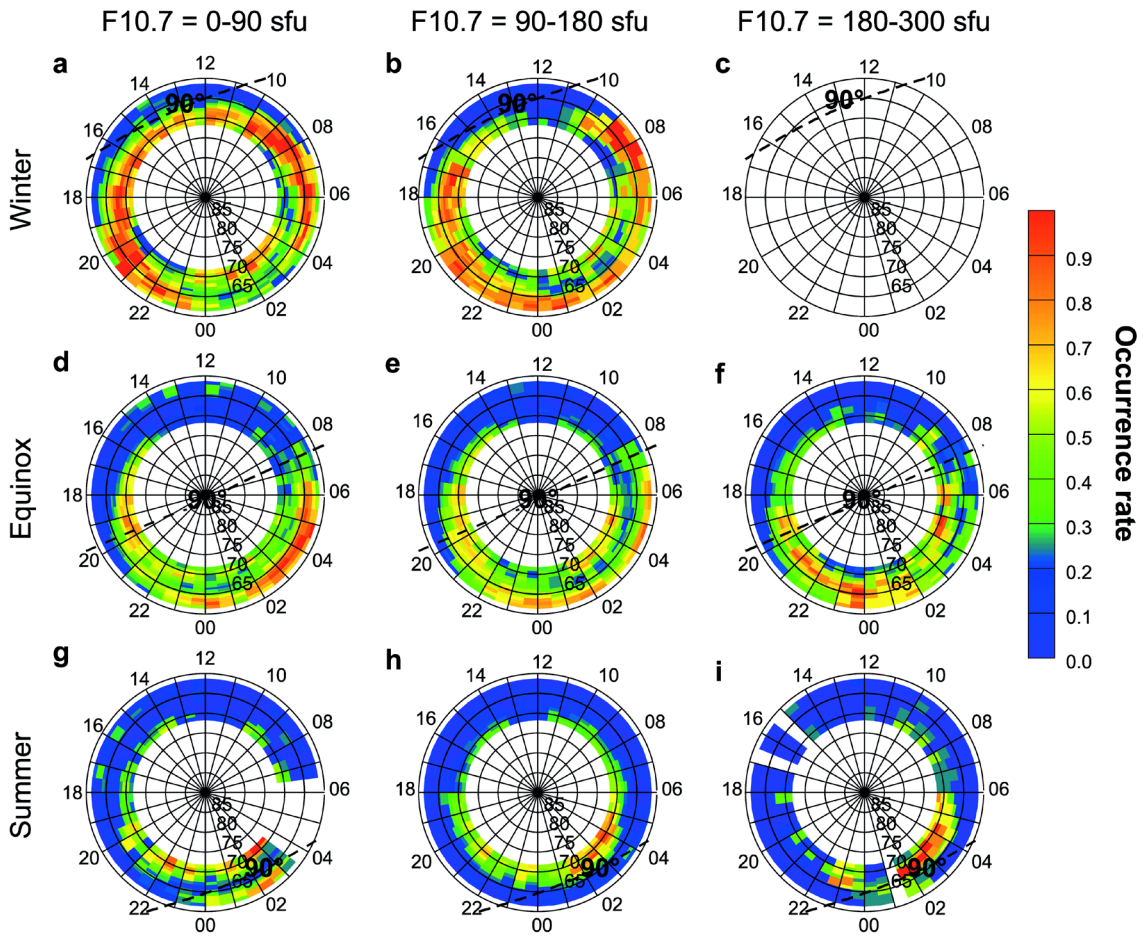

Figure 3.2. Occurrence rate of the trough divided into three seasons and three solar activities. Black dashed line in each polar plot indicates the average solar terminator, where the solar zenith angle equals 90° [from *Ishida et al.*, 2014a]

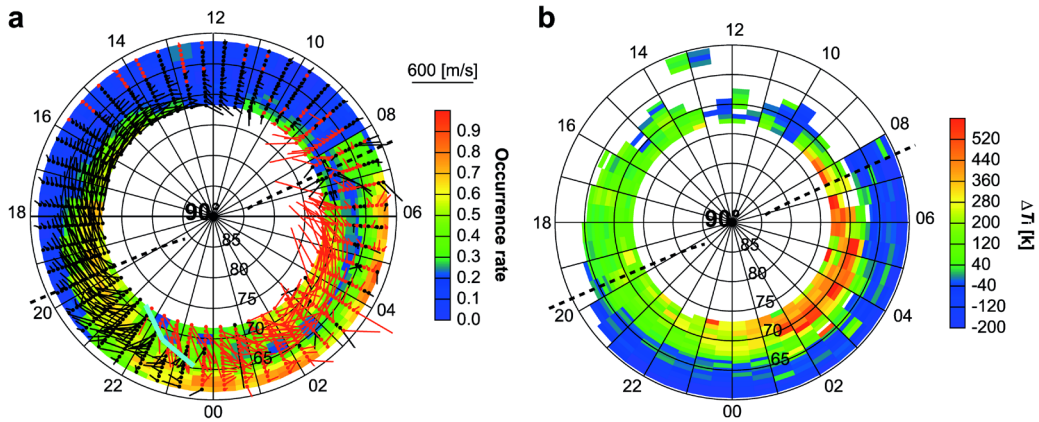

Figure 3.3. Example of the average description of the trough: (a) occurrence rate of the trough with average values of $\boldsymbol{V}_{\mathbf{i}}$ and (b) average value of $\Delta\boldsymbol{T}_{\mathbf{i}}$ within the trough under the same conditions as in Figure 3.2e. Black dashed line in each polar plot indicates the average solar terminator, where the solar zenith angle equals 90°. Red arrows shown in Figure 3a indicate an eastward component, whereas black arrows indicate a westward component [from *Ishida et al.*, 2014a]

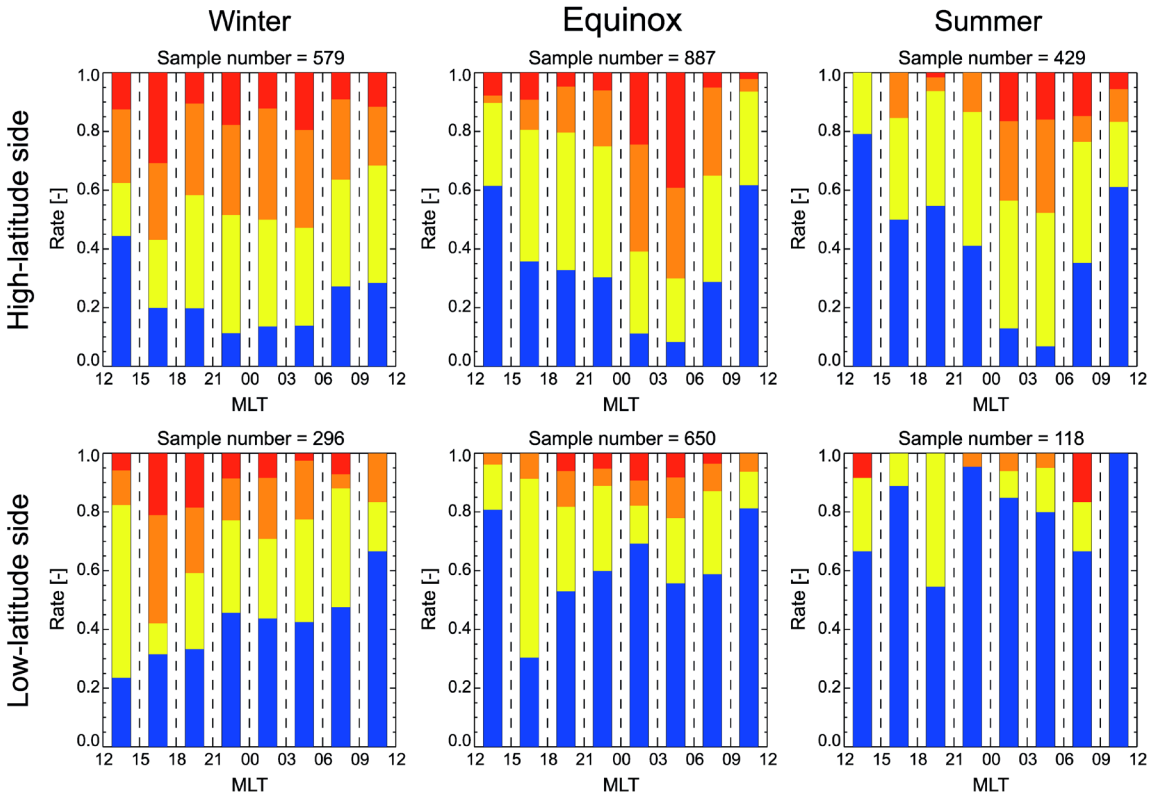

Figure 3.4. Seasonal variation in the $\Delta \boldsymbol{T}_{\mathbf{i}}$ ratio on the high-latitude (upper panels) and low-latitude (upper panels) sides of the field of view. Each color represents a range of $\boldsymbol{T}_{\mathbf{i}}$ increase comprising blue ($\Delta \boldsymbol{T}_{\mathbf{i}} < \mathbf{200\ K}$), yellow ($\Delta \boldsymbol{T}_{\mathbf{i}} = \mathbf{200 - 500\ K}$), orange ($\Delta \boldsymbol{T}_{\mathbf{i}} = \mathbf{500 - 1000\ K}$), and red ($\Delta \boldsymbol{T}_{\mathbf{i}} > \mathbf{1000}\ \boldsymbol{K}$). Left, middle, and right columns show the results for the winter, equinox, and summer seasons, respectively [from *Ishida et al.*, 2014a]

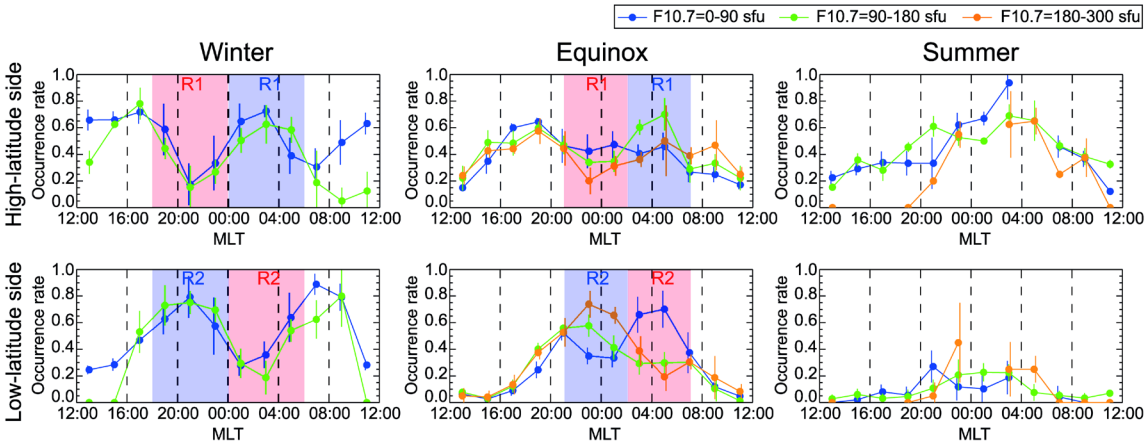

Figure 3.5. F10.7-dependent variation in trough occurrence rate on the high-latitude (upper panels) and low-latitude (lower panels) sides of the field of view. Left, middle, and right columns show the results for the winter, equinox, and summer seasons, respectively. Blue, green, and orange dotted lines shown in each panel are the variation in the occurrence rate at F10.7 = 0–90 sfu, F10.7 = 90–180 sfu, and F10.7 = 180–300 sfu, respectively. Error bars indicate the standard deviation centered on the mean value [from *Ishida et al.*, 2014a]

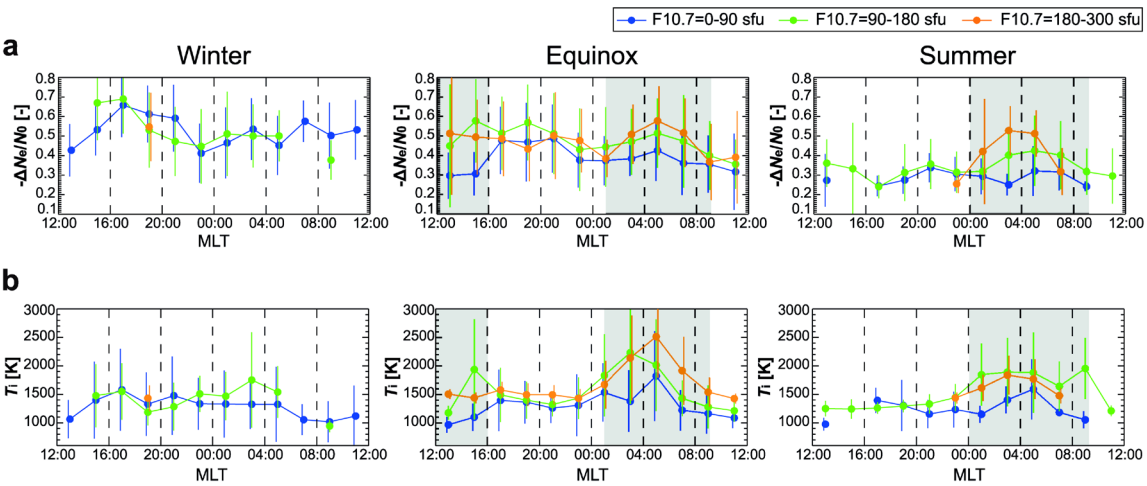

Figure 3.6. F10.7-dependent variation in the parameters associated with trough formation on the high-latitude side of the field of view. Panels show results obtained for the winter, equinox, and summer seasons (from left to right) for (a) trough depth and (d) T_i within the trough [from *Ishida* et al., 2014a]

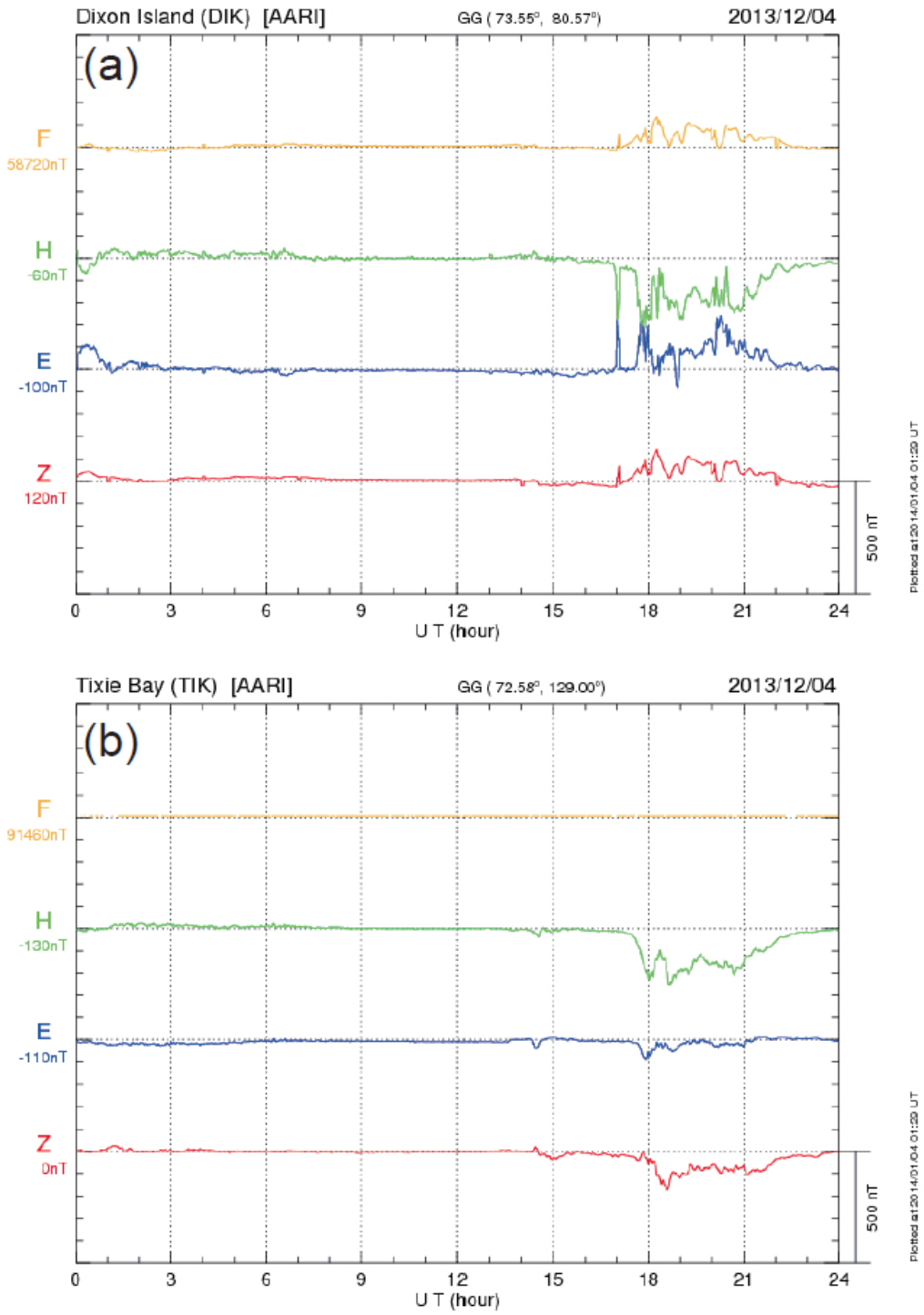

Figure 4.1. Magnetometer data at the (a) Dixon Island station (73.54°N, 80.56°E) and (b) Tixie Bay station (71.58°N, 129.00°E). Yellow, green, blue, and red lines are the magnetic variation of the total intensity, horizontal component, eastward component, and vertical component, respectively

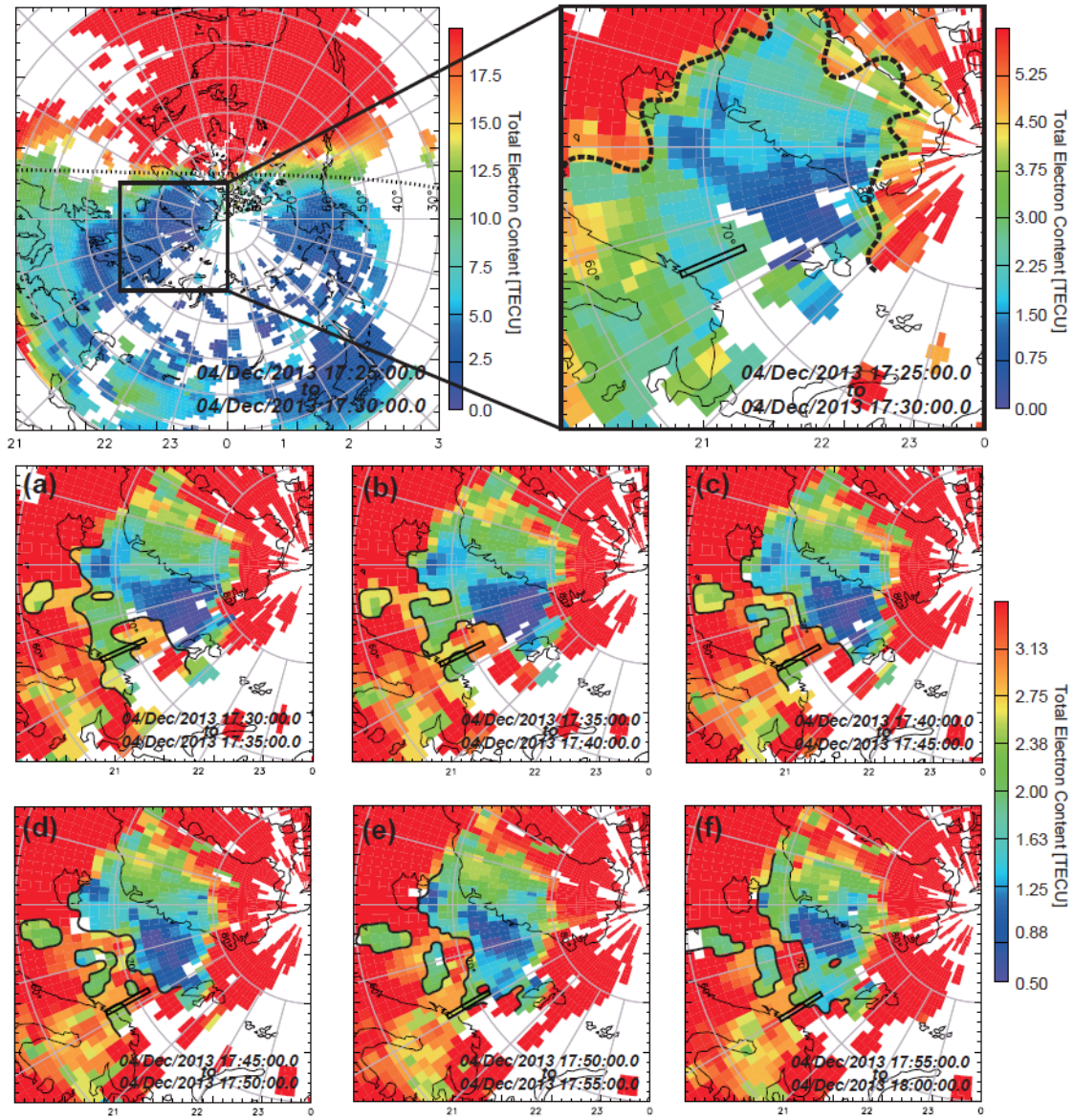

Figure 4.2. The TEC map after onset of the substorm. The top left panel is an overview of the polar ionosphere around onset time, and the top right panel enlarges the black box shown in the top left panel; these data represent the TEC variation around the EISCAT FOV. The color scale runs from high-electron density (red) to low-electron density (blue). The dashed black line in the top left panel represents the solar terminator, where SZA = 90°. The black rectangle in the top right panel indicates the EISCAT FOV, and the dashed curving line indicates the boundary of the high-latitude trough. (a–f) a time sequence of the horizontal shape of the density structures around the EISCAT FOV. The median filter was applied to each TEC map

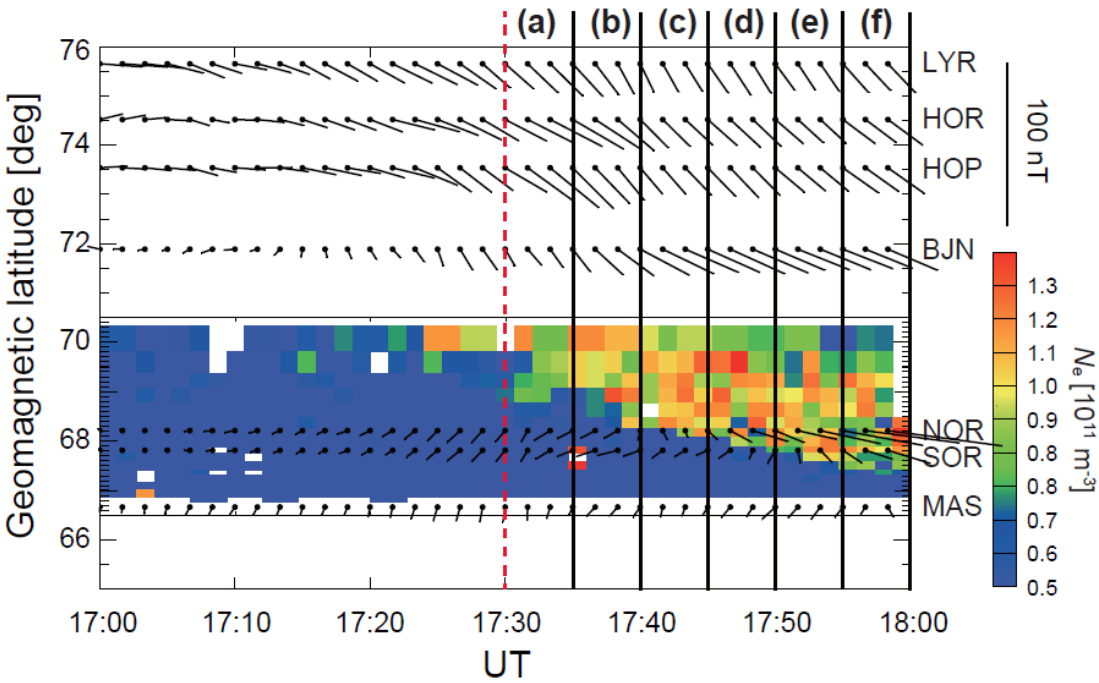

Figure 4.3. Observations from EISCAT and the IMAGE magnetometer during the substorm on 4 December 2013. The keogram was reproduced from the N_e observed by the meridional scans at an altitude of 210 km, with overplotted convection vectors at an altitude of 120 km from the IMAGE meridian chain. The red dashed vertical line indicates the onset time (~17:30 UT), and the remaining 30 minutes is divided into six sections according to Figure 4.2a–f

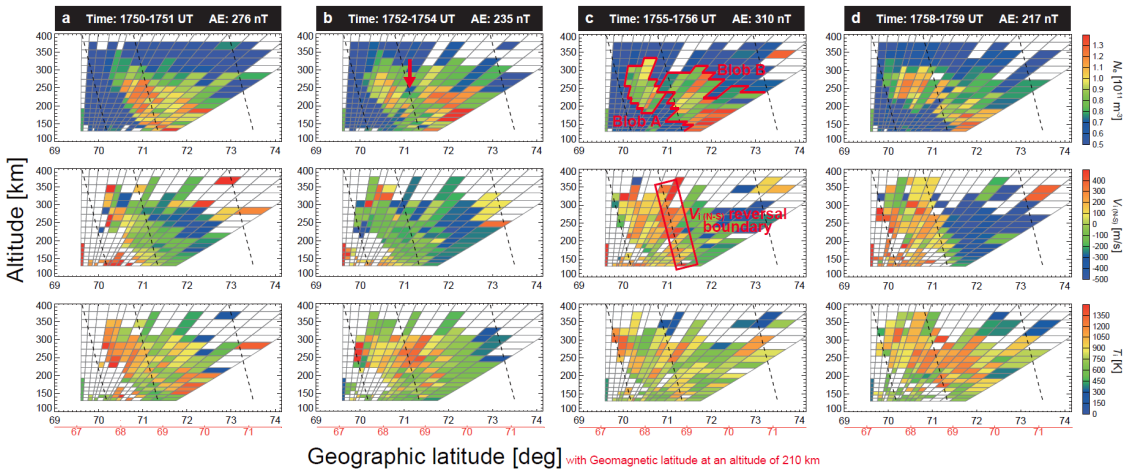

Figure 4.4. The temporal evolution of a blob on the meridional plane during Figure 4.2e-f, with geographic latitudes on the horizontal axes and altitudes on the vertical axes: (top) N_e, (middle) $V_{i\,(N-S)}$, and (bottom) T_i. Dashed slanted lines indicate the geomagnetic field lines. Red horizontal axes indicate the geomagnetic latitudes at an altitude of 210 km

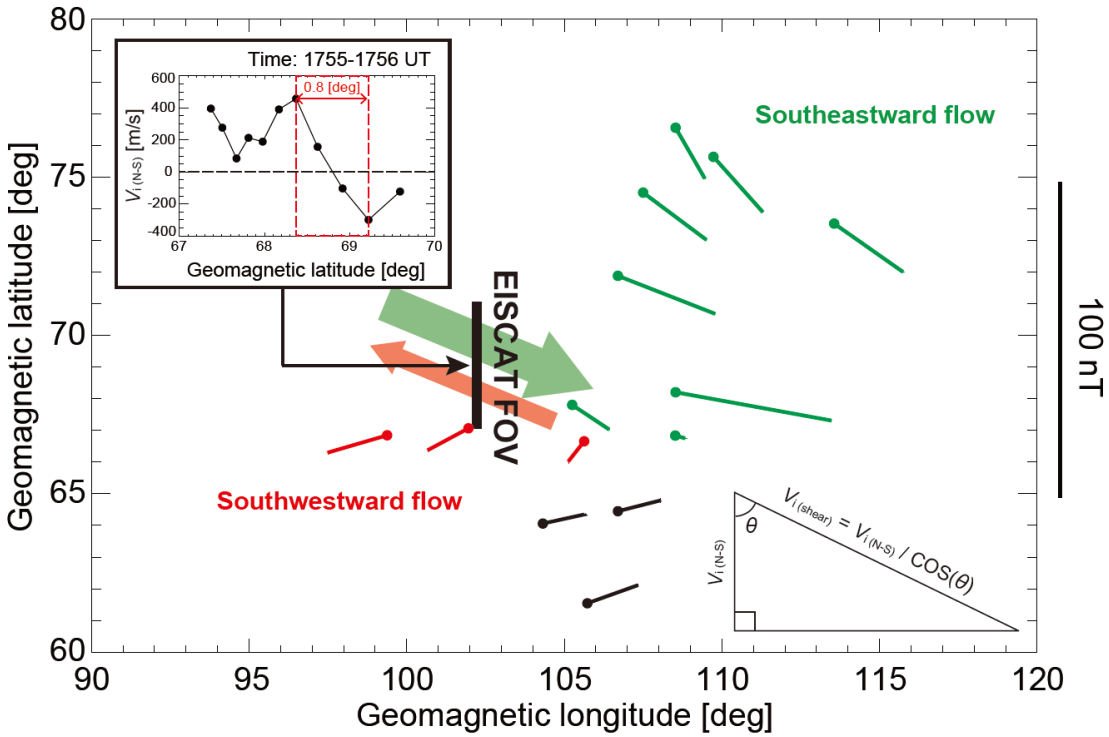

Figure 4.5. The horizontal distribution of the convection vectors at ~17:55 UT. The green, red, and black vectors are the convection vectors from the IMAGE magnetometer. The large red arrow indicates the localized northwestward flow, which was assumed from the horizontal distribution of the convection vector and EISCAT data. The line plot shows the latitudinal variation of the $V_{\mathrm{i\,(N-S)}}$ at ~17:55 UT

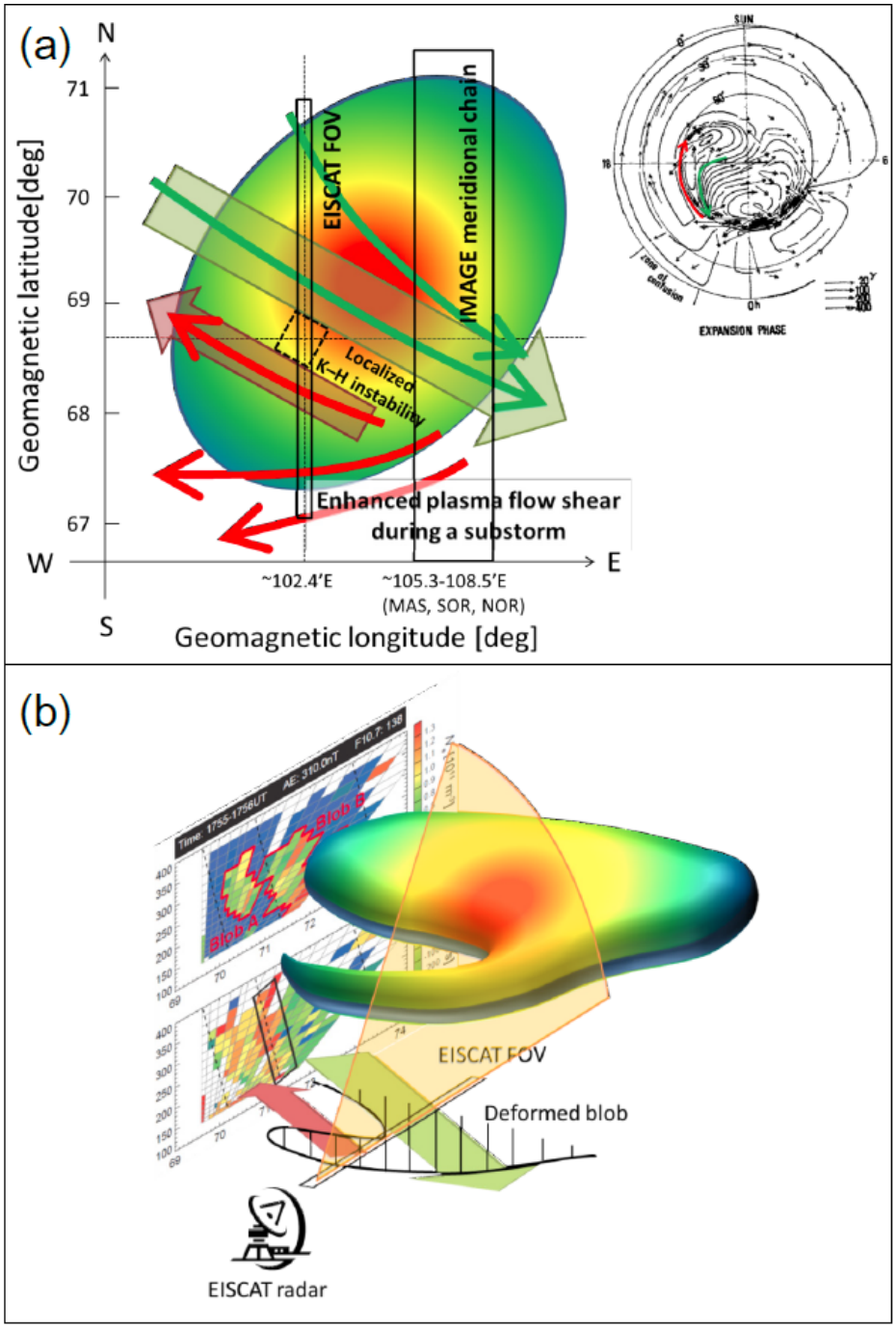

Figure 4.6. Explanation of the K–H instability by schematic illustration. (a) Plausible geometry of the K–H instability on the geomagnetic latitude–longitude coordinates at ~17:55 UT. (b) The relationship between the plasma flow shear and deformed blob shown in Figure 4.4c. Black rectangles are the EISCAT FOV and the observational region by the IMAGE meridional chain. Green and red arrows indicate the expected convection flow during a substorm expansion phase, which was assumed from the convection pattern from *Iijima and Nagata* [1972] (right side of Figure 4.6a)

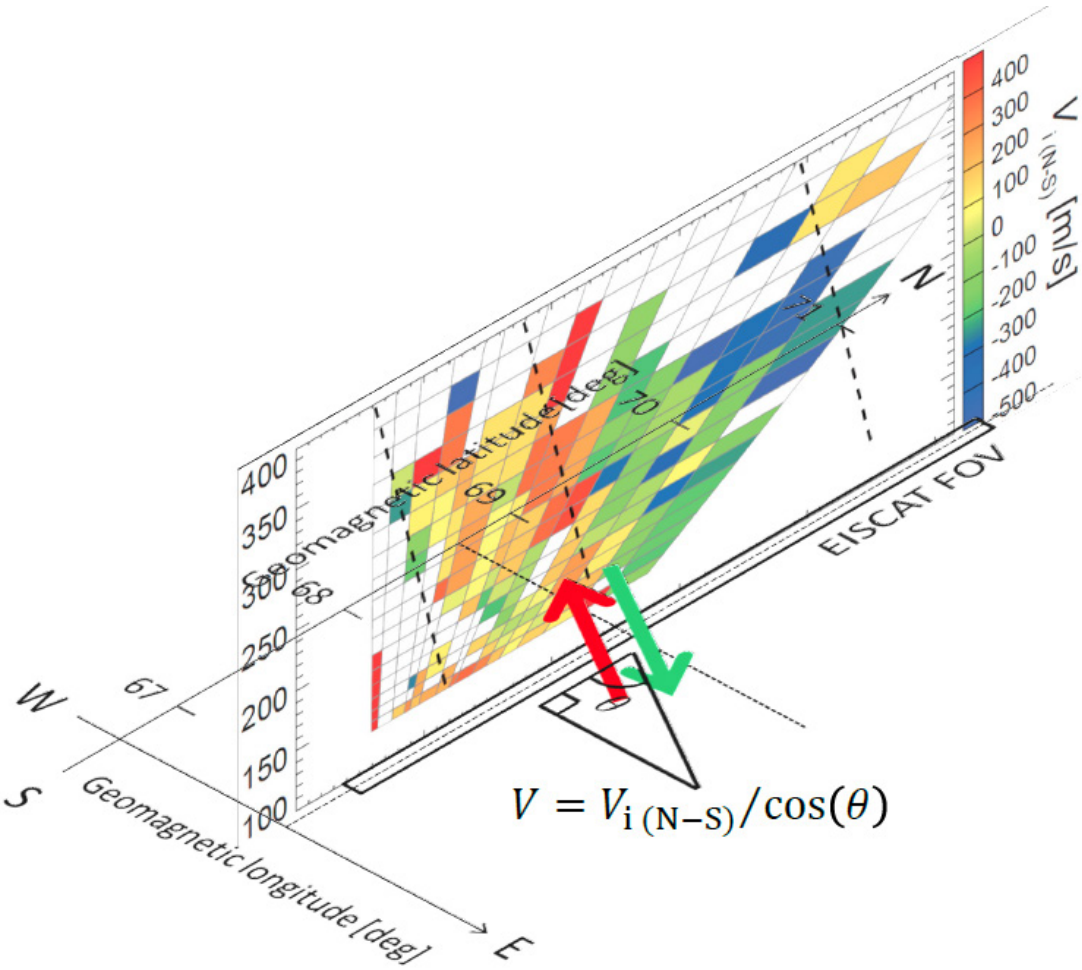

Figure 4.7. The geometry of the EISCAT observations at ~17:55 UT. The observed ion flow data by high-speed meridional scans are plotted on the geomagnetic latitude–geomagnetic longitude plane

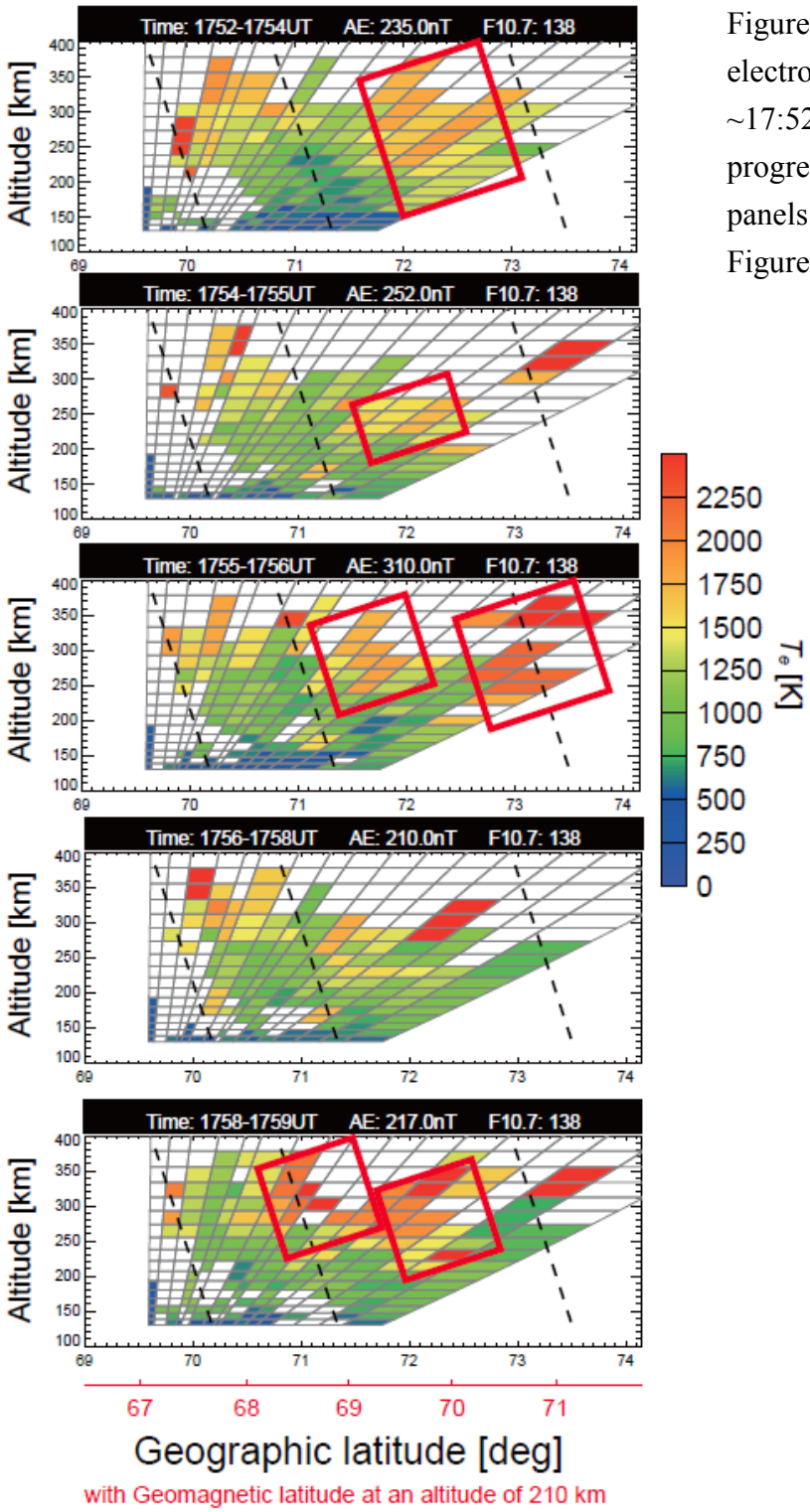

Figure 4.8. Temporal variation of electron temperature during ~17:52–17:59 UT. Time progresses from the top to bottom panels. Format is the same as in Figure 4.4

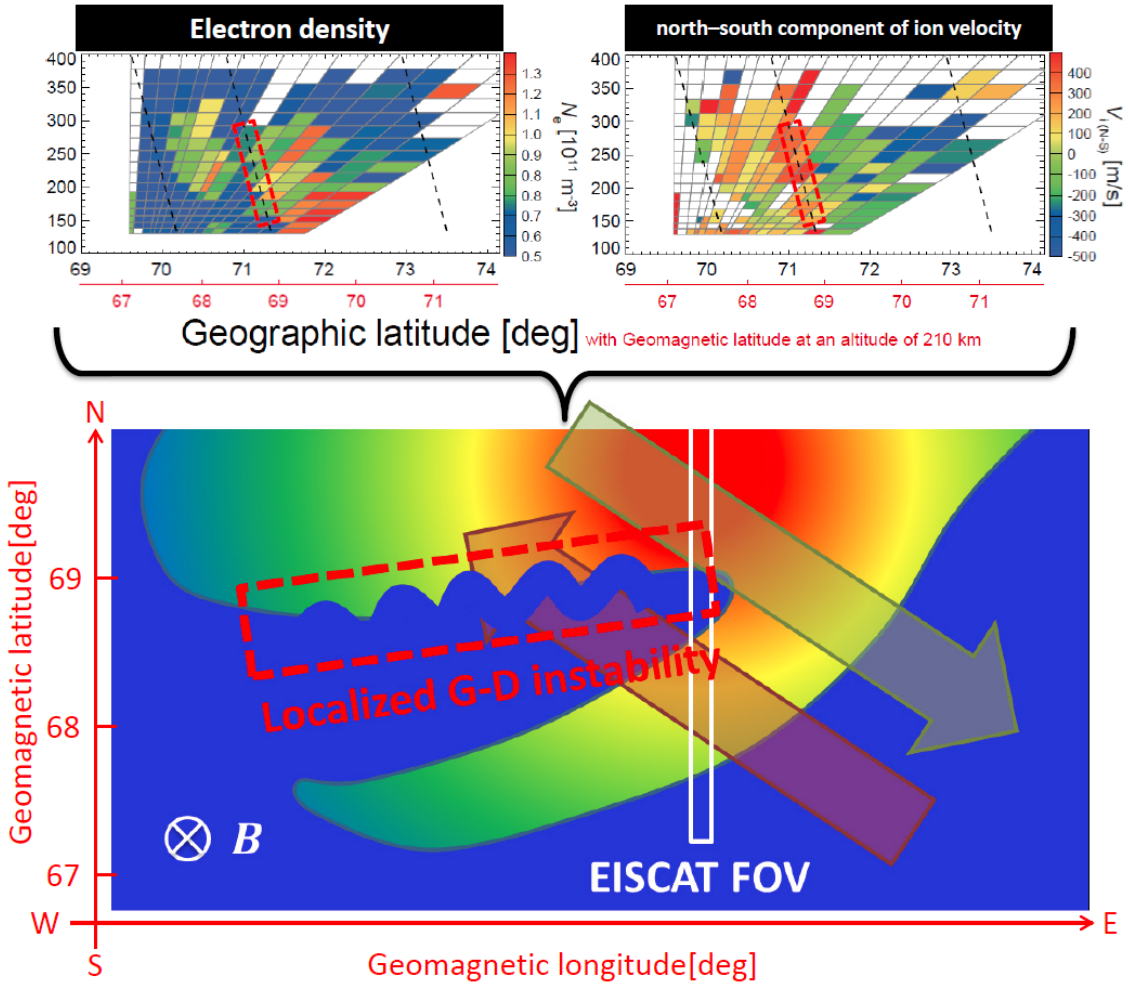

Figure 4.9. (top) The N_e and $V_{i\,(N-S)}$ from Figure 4.4c, with overplotted dashed red boxes that represent the region where the G-D instability supposedly occurred. (bottom) Schematic illustration of the localized G-D instability on the equatorward boundary of Blob B during 17:55–17:59 UT. Red arrow indicates northwest plasma flow of the enhanced plasma flow shear

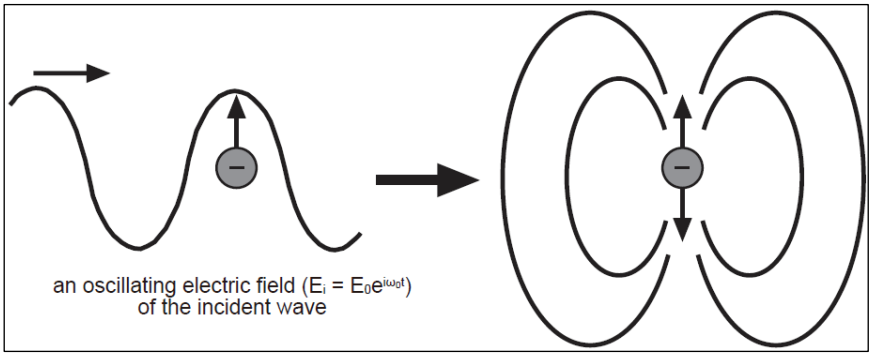

Figure 6.1. Mechanism of Thomson scattering in terms of dipole radiation of an oscillating electron [from *Nygren*, 1996]

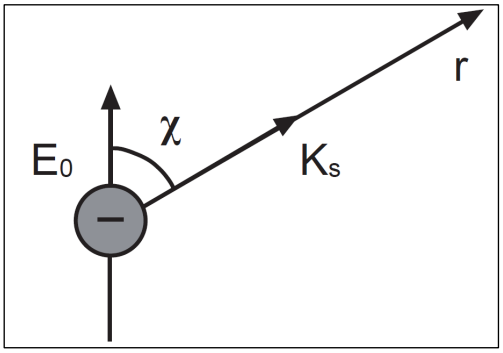

Figure 6.2. Angle between the electric field of the incident wave and the scattering direction [from *Nygren*, 1996]

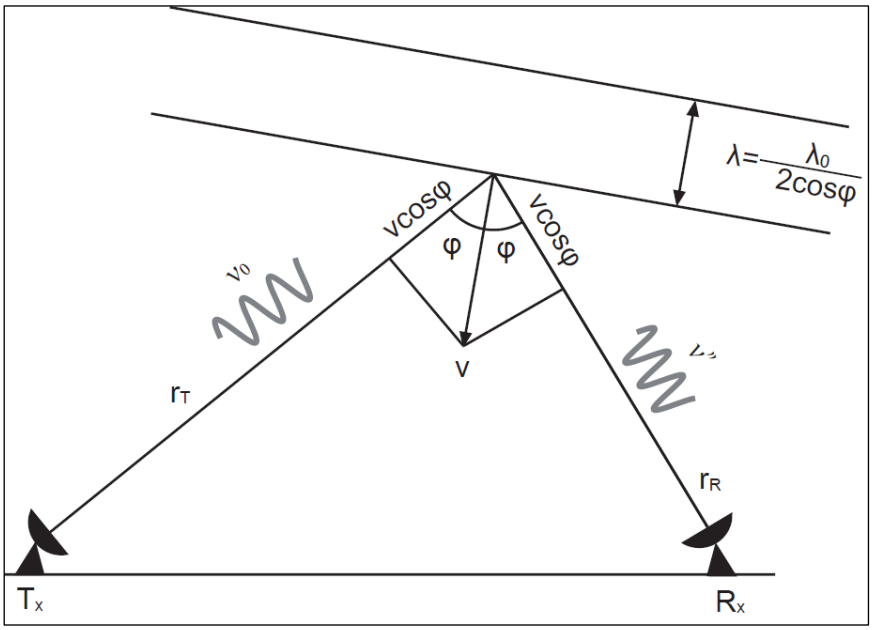

Figure 6.3. Generation of Doppler shift in scattering from plasma waves [from *Nygren*, 1996]

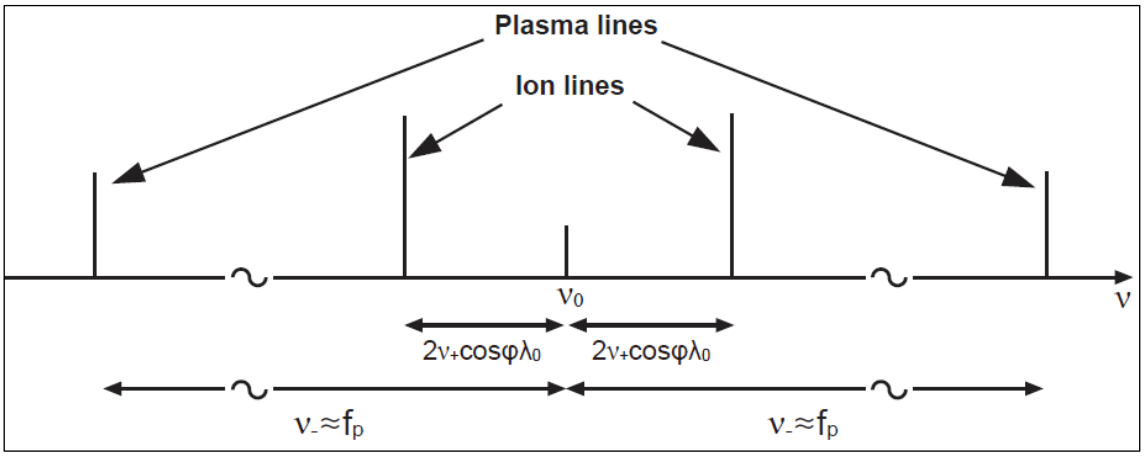

Figure 6.4. Location of ion and plasma lines around the transmitter frequency [from *Nygren*, 1996]

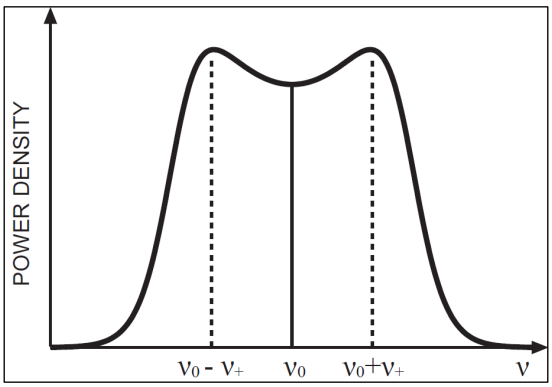

Figure 6.5. Generation of the ion line. The two ion lines shifted from the radar frequency by $\pm\nu_+$ are broadened due to Landau damping so that they merge into a single line [from *Nygren*, 1996]

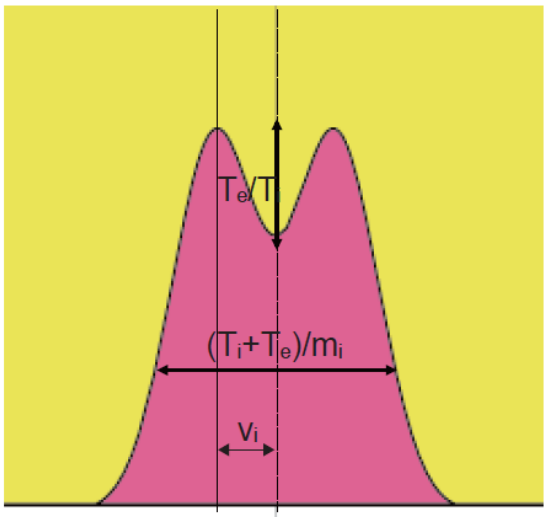

- Ion (and electron) temperature (T_i and T_e) to ion mass (m_i) ratio from the window of the spectra
- Electron to ion temperature ratio (T_e/T_i) from "peak to valley" rartio
- Electron (= ion) density from total area (corrected for temperatures)
- Ion velocity (v_i) from the Doppler shift

Figure 6.6. Dependence of the ion line shape on plasma parameters